



# GOME validation at KNMI and collaborating institutes

*Edited by P. Stammes and A.J.M. Piters*

Koninklijk Nederlands Meteorologisch Instituut



**Scientific report = wetenschappelijk rapport; WR 96-08**

De Bilt, 1996

P.O. Box 201  
3730 AE De Bilt  
Wilhelminalaan 10  
Telefoon 030-220 69 11  
telefax 030-221 04 07

Edited by: P. Stammes and A.J.M. Piters

UDC: 551.501.71  
551.507.362.2  
551.510.534  
551.508.952  
ISSN: 0169-1651  
ISBN: 90-369-2113-9



# GOME validation at KNMI and collaborating institutes

*edited by*

P. Stammes and A.J.M. Piters

*with contributions from*

I. Aben and M.R. Dobber

*Space Research Organization of the Netherlands (SRON),  
Utrecht, The Netherlands*

J.P. Burrows, M. Eisinger, and A. Richter

*Institute of Environmental Physics (IUP), University of Bremen, Germany*

M.A.F. Allaart, A.J. Feijt, H.M. Kelder, R.B.A. Koelemeijer,  
F. Kuik, A.C.A.P. van Lammeren, P.F. Levelt,  
A.J.M. Piters, D.M. Stam, and P. Stammes

*Royal Netherlands Meteorological Institute (KNMI), De Bilt, The Netherlands*

October 1996



# List of contents

	page
Preface .....	5
1 GOME overview .....	7
<i>(P. Stammes and A.J.M. Piters)</i>	
2 Validation of GOME polarisation and radiance measurements .....	17
<i>(P. Stammes, D.M. Stam, R.B.A. Koelemeijer, and I. Aben)</i>	
3 Error analysis of polarisation measurements by GOME .....	27
<i>(I. Aben, M.R. Dobber, P. Stammes, and D.M. Stam)</i>	
4 First validation of GOME cloud observations .....	37
<i>(R.B.A. Koelemeijer, P. Stammes, A.J. Feijt, and A.C.A.P. van Lammeren)</i>	
5 Studies on DOAS ozone column retrieval from the UV and visible measurements of GOME .....	47
<i>(M. Eisinger, A. Richter, J.P. Burrows, and A.J.M. Piters)</i>	
6 Ground-based measurements at KNMI used for GOME validation .....	61
<i>(A.J.M. Piters, P.F. Levelt, F. Kuik, M.A.F. Allaart, and H.M. Kelder)</i>	
7 Validation of GOME total ozone column with the Assimilation Model KNMI .....	65
<i>(A.J.M. Piters, P.F. Levelt, M.A.F. Allaart, and H.M. Kelder)</i>	
List of acronyms .....	73



# Preface

The aim of this report is to give an overview of the GOME validation activities that have taken place in 1995–96 at KNMI, partly in collaboration with the Space Research Organisation of the Netherlands (SRON) in Utrecht, and the Institute for Environmental Physics (IUP) in Bremen. It is a compilation of a general introduction on GOME (Chapter 1) and six scientific papers (Chapters 2–7) describing the GOME validation research performed at KNMI together with SRON and IUP. These papers have been published previously in the Proceedings of the GOME Geophysical Validation Campaign Workshop, held 24–26 January 1996 in Frascati, Italy (published as ESA-WPP 108, ESA/ESTEC, Noordwijk, May 1996).<sup>1</sup>

Chapter 1 of this report, entitled “GOME overview”, is intended to help the reader to become familiar with the GOME project and instrument, and to give an overview of the GOME validation activities at KNMI. Chapter 2 discusses the GOME level 1 products, namely radiance and polarisation. Chapter 3 gives an error estimate of the polarisation measurements by GOME. Chapter 4 describes the first validation of the GOME cloud detection scheme, which is used in determining the ozone column. Chapter 5 discusses various aspects of the retrieval of ozone from GOME level 1 data. Chapter 6 shows a comparison between the GOME ozone measurements and ground-based measurements at KNMI. Finally, Chapter 7 demonstrates the use of an atmospheric transport model in the validation of GOME ozone measurements.

The validation activities performed at KNMI have been supported by funding from BCRS and SRON.

---

<sup>1</sup>An asterisk in the list of references of each chapter indicates that the reference is to a paper in the above mentioned proceedings.





## GOME overview

Piet Stammes and Ankie Piters

Royal Netherlands Meteorological Institute (KNMI)  
P.O. Box 201, 3730 AE De Bilt, The Netherlands

### 1 Importance of GOME

The Global Ozone Monitoring Experiment (GOME) has been launched on April 21, 1995, on board the ERS-2 satellite of the European Space Agency (ESA). GOME is the first European satellite instrument intended to observe the Earth's ozone layer from space. Various satellite instruments from the United States and Russia have preceded it — the most notable of these is the Total Ozone Mapping Spectrometer (TOMS), of which several versions have been launched since 1978. Monitoring the ozone layer from space has become especially important since the discovery of the ozone hole above the South Pole in 1985. Since then the development of the ozone layer is being followed with close attention. Satellite measurements are indispensable in this respect, because only these can give a global view of the ozone distribution.

There are at least four reasons why GOME is important. Firstly, no TOMS instrument was available between December 1994, when the Meteor/TOMS was deactivated, and July/August 1996, when new TOMS instruments were launched on board the U.S. Earth Probe and the Japanese ADEOS satellite. Secondly, the GOME instrument uses a new ozone detection technique, which potentially produces more accurate ozone data than TOMS. Thirdly, GOME measures not only ozone but also other trace gases which affect the ozone cycle and other atmospheric-chemical processes. In addition, GOME also measures aerosols, clouds, and the spectral reflectance of the Earth, which are important elements of the Earth's climate system.

The fourth aspect of GOME is that it is the first of a number of satellite instruments which will perform spectroscopic remote sensing measurements of the Earth's atmosphere from the ultraviolet to the near-infrared. The other instruments are SCIAMACHY, to be launched in 1999 on board ENVISAT, and OMI, to be launched from 2001 onwards on board the METOP series (see the end of this report for an explanation of acronyms). With GOME we will gain experience in interpreting spectroscopic remote sensing data, which can then be used to prepare for SCIAMACHY and OMI data analysis.

In many respects GOME is the smaller version of SCIAMACHY, which has a larger wavelength range than GOME (extension to 2400 nm) and a limb-view mode in addition to the nadir view mode of GOME. SCIAMACHY is important for the atmospheric research community in the Netherlands, because it is being built in a co-operation between Germany, the Netherlands, and Belgium. The lead scientist of GOME and the PI of SCIAMACHY is Prof. Dr. J. Burrows of the University of Bremen, Germany. The co-PI of SCIAMACHY is Dr. A. Goede from SRON.

The OMI instrument from ESA and EUMETSAT still has to be defined, but it will probably be an improved version of GOME. For OMI two principal users have been selected: Dr. H. Kelder from the Netherlands (KNMI) and Dr. R. Guzzi from Italy (IMGA).

### 2 GOME instrument

The ERS-2 is a polar satellite orbiting the Earth in about 100 minutes at an altitude of 780 km. The North-South passage of the equator takes place at 10:30 local solar time. The speed of the spacecraft relative to the ground is about 6.7 km/s. GOME is scanning the Earth with a mirror from East to West in 4.5 s (forward scan), and then sweeps back in 1.5 s (backscan). The swath size in the flight direction is 40 km. The swath width can be varied between 120 and 960 km (default value). The maximum scan angle for the 960 km swath is 31°. The swath width of 960 km gives approximately global coverage of the Earth at the equator in three days. Since the standard integration time of most GOME channels is 1.5 s, each forward scan is divided into three ground pixels called East, Nadir, and West pixels. Their size is on average  $320 \times 40 \text{ km}^2$  for the default swath width. The radiation observed during the backscan is also integrated, which yields the Backscan pixel.

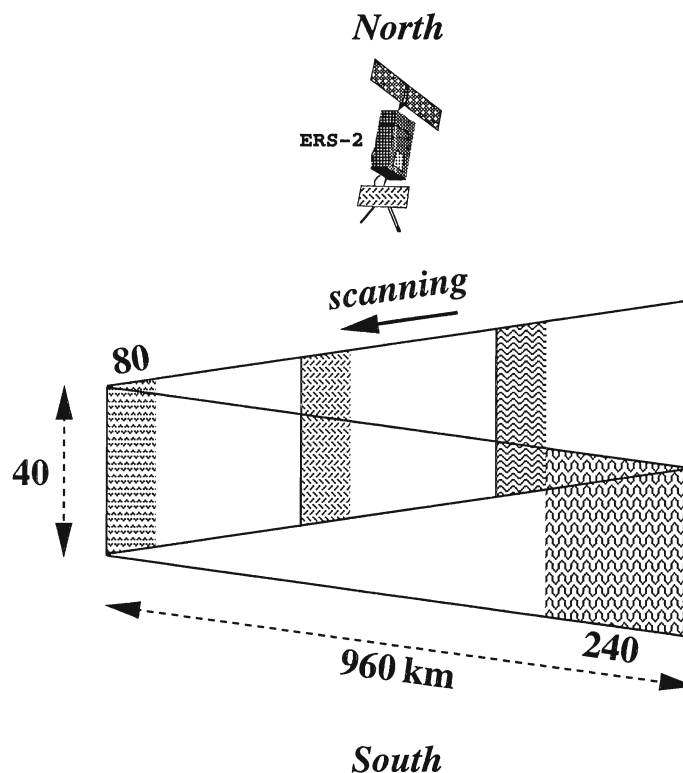


Figure 1: Schematic of the GOME pixels used in the validation phase, as seen from above. The East, Nadir, and West pixels are on average  $80 \times 40 \text{ km}^2$ , whereas the Backscan pixel is about  $240 \times 40 \text{ km}^2$ . In the first operational phase the pixels will have their full size, i.e. on average  $320 \times 40 \text{ km}^2$  for the East, Nadir, and West pixels and  $960 \times 40 \text{ km}^2$  for the Backscan pixel. Note the different scales in  $x$ - and  $y$ -directions. (Figure from D.M. Stam)

During the GOME validation phase the integration time was limited to 0.375 s, because of overexposure over cloudy scenes. Therefore, each pixel was limited to the western quarter of the original pixel, i.e. on average a  $80 \times 40 \text{ km}^2$  area for the East, Nadir and West pixels, and a  $240 \times 40 \text{ km}^2$  area for the Backscan pixel (see Fig. 1). In the operational phase the pixel size has been restored to normal, i.e. on average  $320 \times 40 \text{ km}^2$  for a 960 km swath, due to implementation of the so-called co-adding mode in the instrument.

GOME is a four-channel grating spectrometer measuring the Earth's radiance almost contiguously from about 240 to 790 nm. The spectrometer's channels and their resolution are listed in Table 1. The standard integration time is 12 s for channel 1A and 1.5 s for channels 1B–4 (0.375 s before the co-adding mode was used). These integration times are longer for low sun. Because GOME is sensitive to polarisation, it measures the polarisation of the incoming light using so-called PMDs in three broad spectral bands, which are given in Table 2. In this way the measured signal can be corrected for polarisation in order to obtain a radiance. The GOME polarisation measurement yields two Stokes parameters:  $I$  and  $Q$  (see Chapter 2). The PMDs have a pixel size of 1/16-th of the spectrometer's pixel size, i.e. on average  $20 \times 40 \text{ km}^2$  for a 960 km swath. This means that the PMDs have 48 pixels across the swath, and can therefore be used for coarse imaging of the Earth in three colours (see Chapter 4). This is especially helpful for scene identification and cloud detection. From the overlap between spectral channels 1B and 2 and between channels 3 and 4 in principle also polarisation can be derived. However, it appears that these data are not (yet) of good quality.

Once per day GOME is observing the Sun via a diffuser plate. Spectral calibration of the instrument is performed using an on board line lamp. More technical details about GOME can be found in the GOME Users Manual (ESA, 1995).

Table 1: Spectral ranges and resolutions of the GOME spectral channels. The spectral ranges are from the GDP level 1 data product, version 0.70. The resolution data are from Hoekstra et al. (1996).

spectrometer channel	spectral range	resolution
channel 1A	237–307 nm	0.18 nm
channel 1B	307–315 nm	0.18 nm
channel 2	313–405 nm	0.17 nm
channel 3	407–608 nm	0.28 nm
channel 4	599–794 nm	0.30 nm

Table 2: Spectral ranges and effective wavelengths,  $\lambda_e$ , of the GOME polarisation measurements.

polarisation channel	spectral region	$\lambda_e$	remark
PMD 1 (blue)	300–400 nm	350 nm	
PMD 2 (green)	400–600 nm	490 nm	
PMD 3 (red)	600–800 nm	605 nm	
overlap 1 (ch. 1B/2)	313 nm	313 nm	bad data
overlap 3 (ch. 3/4)	605 nm	605 nm	bad data

### 3 GOME data processing

#### 3.1 Level 0–1 processing

The raw data of 10 out of every 14 orbits are received in Kiruna (S), and then sent to DLR, Oberpfaffenhofen (D), where they are processed together with the other orbits received at other stations. The GOME Data Processor (GDP) running at DLR produces from the raw data calibrated and geolocated Earth radiances and calibrated solar irradiances, which are called level 1 data. The main calibration steps of the level 0–1 processing scheme are (DLR, 1996): (a) leakage current correction, (b) straylight correction, (c) wavelength calibration, (d) radiometric calibration, and (e) polarisation correction.

In the validation phase not the level 1 data, but the level 0 data together with the calibration software (called extraction software) were distributed to the users; this will probably also occur for the operational phase. The advantage of this procedure is that, when new calibration constants become available, only the extraction software databases have to be replaced and not the entire level 1 product.

The GOME data were more or less routinely processed from 22 July 1995 onwards. The co-adding mode was switched on by the end of March 1996.

The main level 1 data products from GOME are:

1. Spectrum of solar irradiance  $\pi F$  measured perpendicular to the solar direction (in  $\text{mW}/\text{m}^2/\text{nm}$ )
2. Spectrum of Earth radiance  $I$  per pixel (in  $\text{mW}/\text{m}^2/\text{nm}/\text{sr}$ )
3. Fractional polarisation  $p$  per pixel in the three PMD bands
4. Sub-pixel radiances in the three PMD bands.

The reflectivity of a pixel, denoted by  $R$ , is defined as:

$$R = I/(\mu_0 F), \quad (1)$$

where  $\mu_0$  is the cosine of the solar zenith angle. The reflectivity is the quantity needed for atmospheric studies.

In Fig. 2 the reflectivity spectrum of a cloud-free nadir pixel ( $70 \times 40 \text{ km}^2$ ) in the center of the Netherlands is shown, as measured by GOME on 25 July 1995 at 10:49 UTC. The solar zenith angle was  $34^\circ$ . A large number of gaseous absorption bands can be discerned in the spectrum, the strongest of which are due to  $\text{O}_3$ ,  $\text{O}_2$ ,  $\text{H}_2\text{O}$ , and  $\text{NO}_2$ . The shape of the continuum is determined by Rayleigh scattering (at the shorter wavelengths), aerosol scattering (all over the spectrum), and surface reflection (most clearly at the longer wavelengths). The broad peak around 550 nm and the increase in reflectivity from 700 nm onwards are spectral signatures of vegetation. This agrees with the pixel location, which is “the green heart of Holland”. The many small peaks from about 340 to 400 nm are mainly due to Raman scattering. In summary, a lot of information about atmosphere and surface is contained in this single GOME measurement.

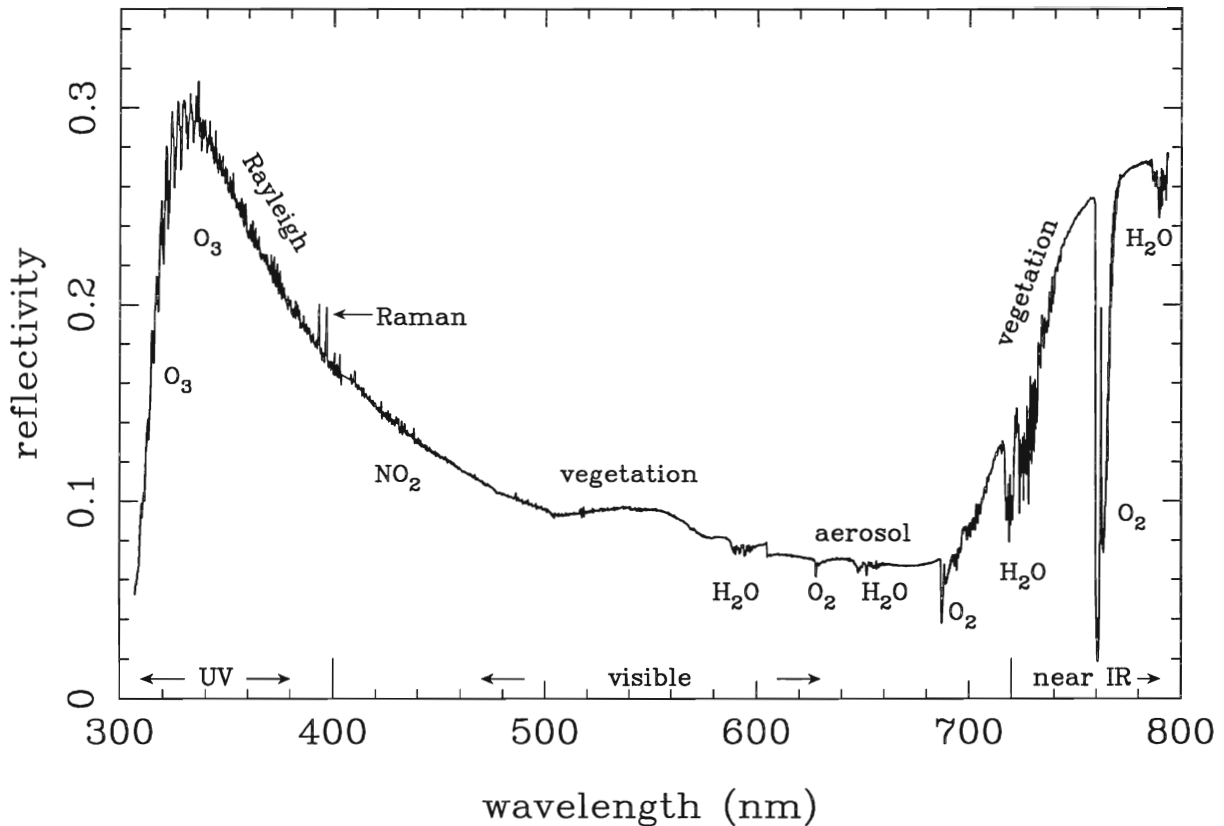


Figure 2: Reflectivity spectrum of the center of the Netherlands, as measured by GOME on 25 July 1995, 10:49 UTC (orbit 1364, pixel 1853; center: 52°N, 5°E).

### 3.2 Level 1–2 processing

From the GOME level 1 data various geophysical products can be derived, which are called level 2 products. Trace gas columns can be retrieved from the GOME spectra using the Differential Optical Absorption Spectroscopy (DOAS) method. Initially, the GDP only derives the  $O_3$  and  $NO_2$  columns. The DOAS method (see Chapter 5) is an experimental absorption band fitting-method based on the extinction law of Lambert-Beer. In practice, it can be used for relatively weak absorption bands, like the ozone Huggins and Chappuis bands. The advantage of the DOAS method is that it does not need a radiometric calibration, but only a wavelength calibration.

The DOAS algorithm consists of the following main steps:

1. Selection of a narrow spectral interval (the DOAS window), showing sufficient absorption band structure due to the absorber(s) under consideration.
2. Subtraction of a low-order polynomial from the negative logarithm of the reflectivity in this interval. This step separates the absorption structure from the scattering structure in the spectrum, because scattering processes are a smooth function of wavelength.
3. The resulting differential absorption spectrum of the atmosphere is fitted to the differential absorption spectrum of the absorber(s), which is known from laboratory measurements. This yields the effective slant column density of absorber(s), *SCD*.

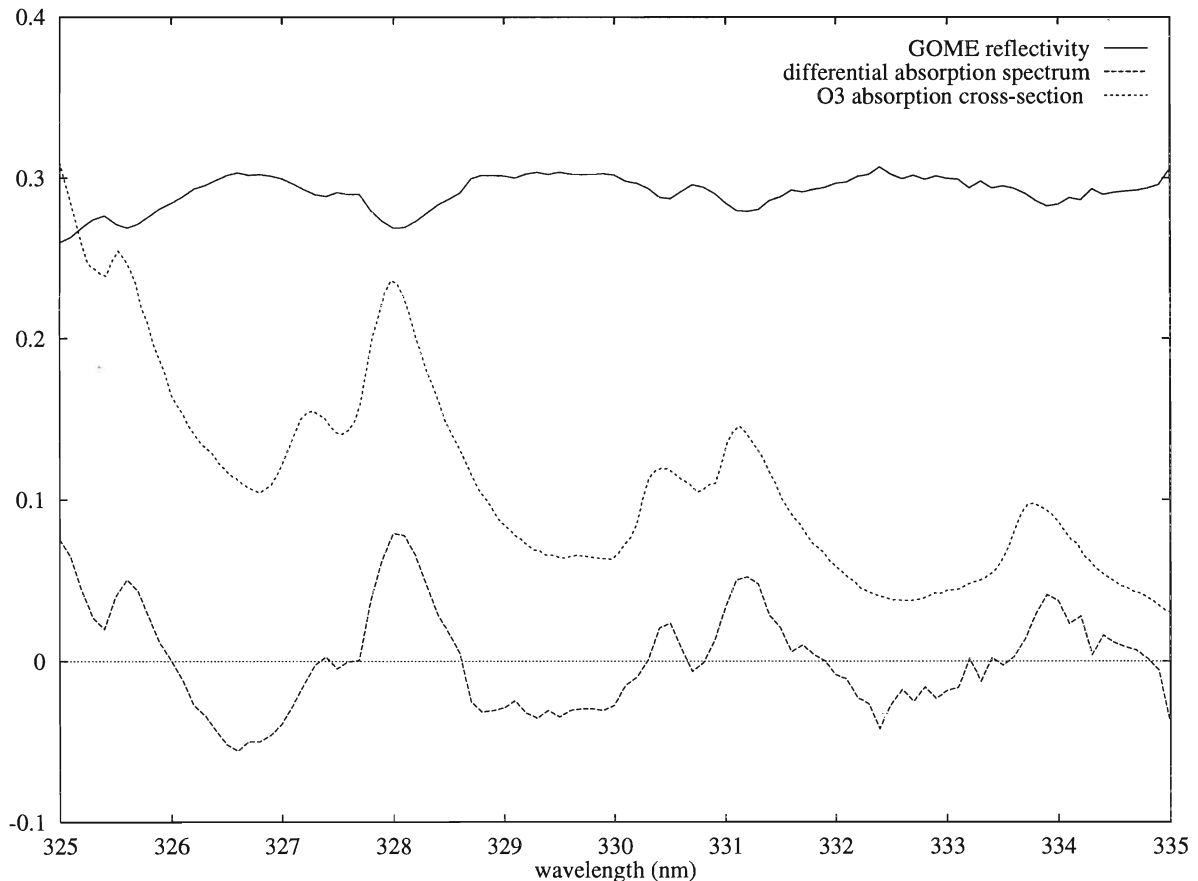


Figure 3: Steps of the DOAS procedure. **Solid curve:** GOME measurement of reflectivity  $R$  in the spectral region between 325 and 335 nm on 25 July 1995 over the Netherlands (detail from Fig. 2). **Dashed curve:** the differential absorption spectrum of the atmosphere, i.e.  $-\ln R$  - polynomial (unit: differential optical thickness). **Dotted curve:** the ozone absorption cross-section at  $-30^\circ\text{C}$  (unit:  $5 \times 10^{-20} \text{ cm}^2/\text{molecule}$ ).

Summarizing, the DOAS formula is (cf. Chapter 5, and Spurr, 1994):

$$\ln R(\lambda) = -\sigma_1(\lambda) SCD_1 - \sigma_2(\lambda) SCD_2 - \dots - a_0 - a_1(\lambda - \lambda_0) - a_2(\lambda - \lambda_0)^2 \quad (2)$$

where  $\sigma_i$  is the absorption cross-section of absorber  $i$  (in  $\text{cm}^2/\text{molecule}$ ),  $SCD_i$  is the slant column density of absorber  $i$  (in  $\text{molecules}/\text{cm}^2$ ),  $a_j$  ( $j = 0, 1, 2$ ) is a polynomial coefficient, and  $\lambda_0$  is some reference wavelength.

The vertical column density of the absorber,  $VCD$ , is related to the  $SCD$  by the so-called airmass factor,  $AMF$ , which represents the effective optical path in the atmosphere due to scattering. We have:

$$VCD = SCD/AMF. \quad (3)$$

The  $AMF$  is computed from a radiative transfer model using the formula:

$$AMF = \frac{\ln I_{no\ i} - \ln I_i}{\tau_i}, \quad (4)$$

where  $I_{no\ i}$  and  $I_i$  are the radiances calculated without and with absorber  $i$ , respectively, and  $\tau_i$  is the vertical optical thickness of absorber  $i$ .

In the GOME data processing the ozone fitting window is chosen from 325 to 335 nm. In Fig. 3 the reflectivity spectrum in this window is shown, taken from the full spectrum of Fig. 2. Also the differential absorption optical thickness spectrum of the atmosphere is shown, which is the negative natural logarithm of the reflectivity minus a polynomial. The ozone Huggins bands can be clearly seen in this spectrum. For



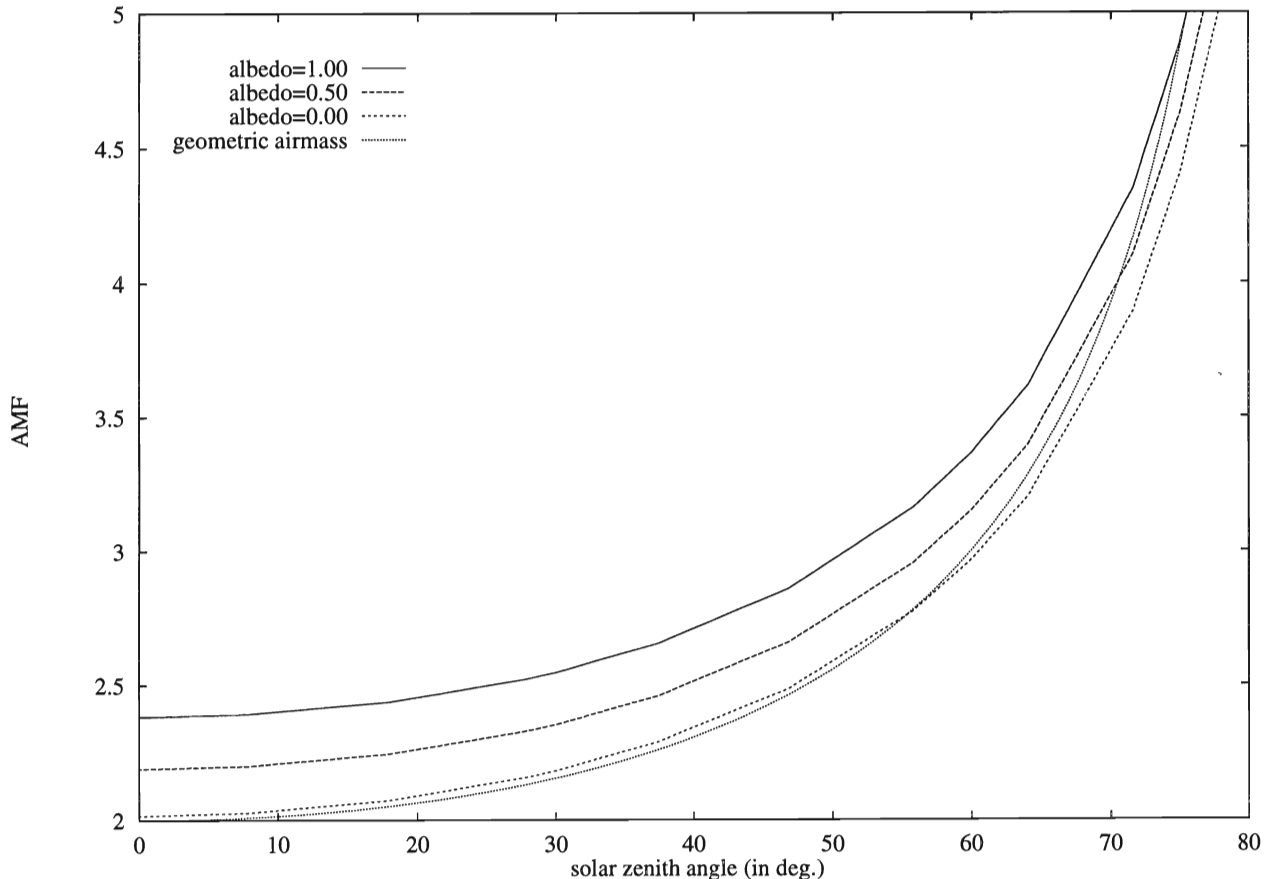


Figure 4: Airmass Factor ( $AMF$ ) at 330 nm calculated by DAK as a function of solar zenith angle (in degrees) for nadir view and three values of the surface albedo. Atmospheric model: Mid-Latitude Summer with background aerosol profile. The geometric airmass is also shown.

comparison the ozone absorption reference spectrum at  $-30^\circ$  C is also given. The GDP DOAS method yielded a vertical ozone column of 288 DU in this case, which compared well with the simultaneous KNMI Brewer measurement of 292 DU (direct sun).

The accuracy of the ozone vertical column not only depends on the DOAS derived slant column, but also on the  $AMF$  calculation. The  $AMF$  depends mainly on viewing and solar geometries, ground albedo, (effective) cloud cover fraction, cloud top height, and ozone profile. In Fig. 4 some calculations of the  $AMF$  for nadir view at 330 nm are shown versus solar zenith angle for the Mid-Latitude Summer atmospheric model (Anderson et al., 1986) and three values of the surface albedo: 0, 0.5, and 1. Calculations were performed with the Doubling-Adding KNMI (DAK) radiative transfer model (Stammes, 1994). For comparison, the geometric airmass, which is in this case  $1 + 1/\mu_0$ , is also shown. The calculations with DAK hold for a plane-parallel geometry, and become inaccurate for solar zenith angles larger than about  $80^\circ$ .

The effect of clouds on the  $AMF$  is taken into account in the level 1–2 processing by the ICFA algorithm. This algorithm uses the depth of  $O_2$  A-band as an estimate of the airmass above the reflecting surface (clouds or ground). The depth of the  $O_2$  A-band depends in first instance on cloud cover fraction and cloud top pressure. Using a climatology for cloud top pressure, the cloud cover fraction is derived (see also Chapter 4). The  $VCD$  is calculated separately for the clear and cloudy parts of the pixel. For the cloudy parts a so-called ghost column is added, which represents the tropospheric ozone column shielded by clouds. The  $VCD$ s of the clear and cloudy parts are then added by weighting with the cloud cover fraction to yield the  $VCD$  of the pixel.

## 4 GOME validation campaign

From July 1995 to Spring 1996 the GOME validation campaign took place. The aim was to determine the quality of the GOME data, especially the ozone column, by comparison with independent ground data. In this international campaign about 20 groups were involved. A relatively large contribution came from the Netherlands: KNMI, RIVM, SRON, and TNO/TPD were all involved. A report of the validation campaign has been published recently (ESA, 1996).

The GOME validation activities at KNMI were the following (with ESA validation project number between brackets):

1. *Radiance and polarisation validation* (NL-109, in cooperation with SRON).  
Radiances and polarisation were checked for consistency and compared with radiative transfer theory and calculations for simple scenes and geometries. See Chapters 2 and 3.
2. *Cloud validation* (part of NL-114).  
The ICFA cloud cover fraction was compared with Meteosat cloud measurements. Furthermore, a new way to use the PMD measurements for cloud imaging was investigated. See Chapter 4.
3. *Ozone validation* (NL-112 and part of NL-114).  
Here three activities were performed:
  - (a) A study on DOAS retrieval of ozone in the visible. See Chapter 5.
  - (b) Comparison of the GOME ozone column with the Brewer total ozone measurements, and measurement strategy of ozone soundings performed at KNMI. See Chapter 6.
  - (c) A data assimilation approach of GOME validation. The AMK model was used to assimilate GOME ozone measurements and to study GOME measurement uncertainties and systematic errors. See Chapter 7.

Furthermore, KNMI was also member of a small number of validation groups selected by ESA to study the reprocessed data from April to June 1996.

The results of the GOME validation can be briefly summarized as follows (for more details, see the relevant Chapters):

- The level 1 data were in general quite good, but there are still some problems in the data processing, which cause a delay in release of the level 1 data. For instance, in the UV the solar irradiance is deviating several percent from SOLSTICE data. Also instrumental effects, like etaloning, are visible in the irradiance. By using the on board calibration, a dynamic calibration database will be created to improve irradiances and radiances. The spatial aliasing effect due to serial read-out of the detectors may be partly corrected in the near future.
- The level 2 data to be released from August 1996 onwards are the ozone column and the NO<sub>2</sub> column. The accuracy of the ozone column is better than 3 % (including systematic and random ( $1\sigma$ ) errors) for solar zenith angles up to 60°, and better than 10 % for solar zenith angles up to 90°. The accuracy of the NO<sub>2</sub> column is about 10 % for nonpolluted areas.

## 5 GOME data assimilation at KNMI

The amount of ozone in the atmosphere is highly variable in time and space. Since GOME (or any other ozone-measuring satellite instrument) cannot observe the whole Earth fast enough to cover this variability, the observations are assimilated in global transport models to predict the ozone distribution at any specific time and place. Data-assimilation techniques, which are commonly used in meteorological models, use the (known) statistical error characteristics of both the measurements and the model to predict the most probable global ozone distribution. An example, calculated with the two-dimensional Assimilation Model KNMI (Levelt et al., 1996) using GOME total ozone observations, is shown in Fig. 5.

When the statistical error characteristics of the ozone observations are not known, as is the case for GOME, it is possible to use data assimilation techniques to study these error characteristics. This concept is used in Chapter 7. An upper limit for the intrinsic (random) uncertainty in the retrieved total ozone column is derived, and a systematic error depending on viewing geometry is identified.

## 6 Outlook

The GOME level 2 data, with the ozone column as the main product, has been released to the scientific community in August 1996. It can be anticipated that a lot of atmospheric research will be performed with these data. In the meantime the validation of the GOME data products has to be continued, because the performance of the instrument and the retrieval algorithm have to be monitored. Furthermore, the ozone data in the co-adding observation mode of GOME ( $320 \times 40$  km<sup>2</sup> pixels) are not yet fully validated. This is clearly needed in the near future. When the reprocessed GOME data of the period July 1995 – March 1996 ( $80 \times 40$  km<sup>2</sup> pixels) become available, a comparison between large and small pixels can be made. Then it is possible to decide on the best swath width for GOME, which has until now been an undecided issue.

The level 0–1 processing will have to be improved at DLR, in cooperation with scientists from the GOME Science Advisory Group. A good quality of the level 1 data is essential for various important retrievals, such as ozone profile retrieval and aerosol retrieval. An important aspect of GOME level 1–2 data processing which can be improved is cloud detection using the PMD information.

The Climate Research Department of KNMI (sections AO and AS) will remain involved in GOME data analysis, in national and international cooperations. The research will cover validation, retrieval, and data assimilation studies, such as: validation of GOME level 1 and level 2 data, transport and chemistry of ozone and related trace gases, assimilation of GOME data in the AMK and TMK models, retrieval of ozone profiles and aerosol, cloud detection and characterisation, and radiative transfer studies.

## References

Anderson, G.P., S.A. Clough, F.X. Kneizys, J.H. Chetwynd, E.P. Shettle, 1986: "AFGL Atmospheric Constituent Profiles", Report AFGL-TR-86-0110, Air Force Geophysics Laboratory, Hanscom AFB (MA)

DLR, 1996: *Product Specification Document of the GOME Data Processor*, ER-PS-DLR-GO-0016, Iss./Rev. 3/A, 4 April 1996, DLR, Oberpfaffenhofen

ESA, 1995, *GOME Users Manual*, ESA SP-1182, ESA/ESTEC, Noordwijk

ESA, 1996: *Proceedings of the GOME Geophysical Validation Campaign*, ESA WPP-108, ESA/ESTEC, Noordwijk

Hoekstra, R., C. Olij, E. Zoutman, and M. le Kluse, 1996: Validation of in-orbit calibration of GOME, in: *Proceedings of the GOME Geophysical Validation Campaign*, ESA WPP-108, ESA/ESTEC, Noordwijk

Levelt, P.F., M.A.F. Allaart and H.M. Kelder, "On the assimilation of total-ozone satellite data", to be published in *Ann. Geophys.*, November, 1996.

Spurr, R.J.D., 1994: DOAS slant column retrieval in GOME data processing, IUP, Univ. Bremen, Internal document (Jan. 1994)

Stammes, P., 1994, "Errors in UV reflectivity and albedo calculations due to neglecting polarisation", SPIE Proceedings Vol. 2311, *Atmospheric Sensing and Modeling*, 227–235



Assimilated GOME total ozone  
8-10-95 0h

KNMI/ESA

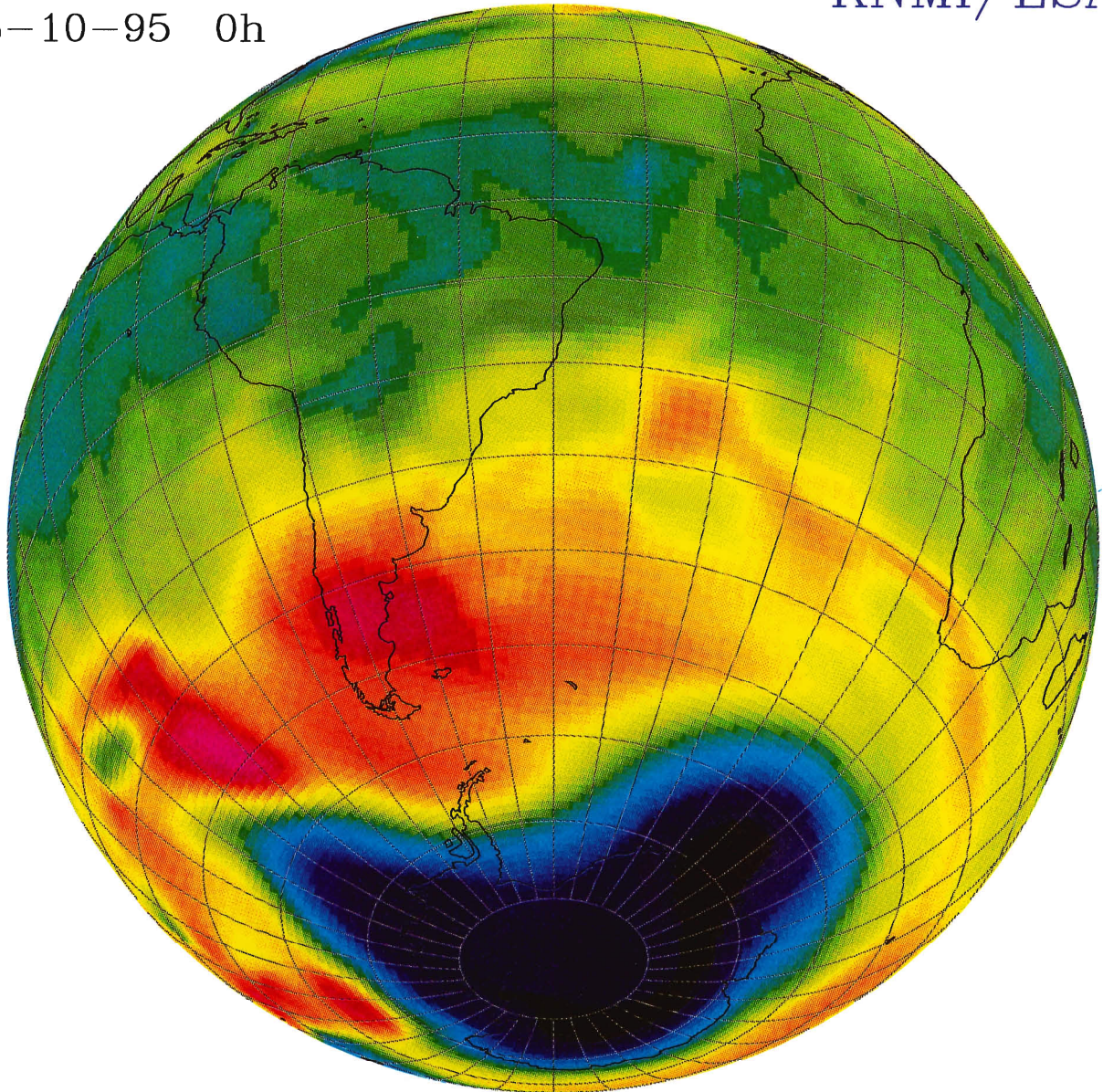


Figure 5: The calculated ozone distribution on 8 October 1995 at 0 UT, based on GOME total ozone observations between 5 and 7 October. The calculation is performed with the Assimilation Model KNMI. Black and blue colours are low ozone amounts, yellow and red are high ozone amounts. The ozone hole over the Antarctic is clearly visible.





# Validation of GOME polarisation and radiance measurements

P. Stammes<sup>1</sup>, D.M. Stam<sup>1,3</sup>, R.B.A. Koelemeijer<sup>1</sup>, and I. Aben<sup>2</sup>

<sup>1</sup> Royal Netherlands Meteorological Institute (KNMI)  
P.O. Box 201, 3730 AE De Bilt, The Netherlands

<sup>2</sup> Space Research Organization Netherlands (SRON)  
Sorbonnelaan 2, 3584 CA Utrecht, The Netherlands

<sup>3</sup> Faculty of Physics and Astronomy, Vrije Universiteit  
De Boelelaan 1081, 1081 HV Amsterdam, The Netherlands

## Abstract

The accuracy of radiance measurements of the Earth by GOME on board ERS-2 depends on the correction for the polarisation sensitivity of the instrument. The polarisation measurements of the Earth by GOME needed to perform this correction have been validated by comparison with polarised radiative transfer calculations.

It has been found that the fractional polarisation measurements of the Polarisation Measuring Devices (PMDs) are consistent and overall correct (for systematic and random polarisation errors, see Aben et al., this issue). The overlap polarisations are strongly deviating, and should not be used in the polarisation-correction scheme.

The radiance measurements show jumps from channel to channel. This is most probably due to the serial read-out of the spectral detector arrays, which causes a varying scene over a spectral channel. Radiance jumps will especially occur over inhomogeneous (e.g. partially cloudy) scenes.

## 1 Introduction

The Global Ozone Monitoring Experiment (GOME) on board the ERS-2 satellite has been designed to measure column densities and, possibly, profiles of trace gases and aerosols in the Earth's atmosphere (ESA, 1993). The primary measurements performed by GOME are, however, spectral radiance measurements of the Earth from about 240 to 790 nm with a high spectral resolution. The spectral radiance, which is called a level 1 data product, is the basis of all derived information on atmospheric composition, e.g. trace gas column densities, which are called level 2 data products. Therefore, the accuracy of the mea-

sured radiance should be as high as possible. Since GOME is sensitive to polarisation (mainly due to its scan mirror and gratings), its radiance measurements must be corrected for the polarisation of the incoming light, because atmospheric radiation is in general polarised. To this purpose, GOME measures the polarisation with three broad-band Polarisation Measuring Devices (PMDs) and three narrow-band channel-overlaps. These polarisation measurements are intended to be used in the polarisation-correction part of the GOME data processing.

The aim of the work presented here is, firstly, to validate the polarisation measurements, and, secondly, to validate the radiance measurements by GOME. Since there was no other polarisation measuring satellite instrument available during the GOME validation phase, which took place in the second half of 1995, the validation approach was indirect by using radiative transfer calculations. The validation approach consisted of: (a) checks on the consistency of the GOME data; (b) comparison of GOME data with results from single scattering theory; (c) comparison of GOME data with multiple scattering results using the Doubling-Adding KNMI (DAK) model.

Part of the validation work was an error analysis of the PMD measurements, based on special geometries along the GOME orbit. This work is described separately in this issue by Aben et al. (1996). Another part, discussing various instrumental effects relevant for polarisation and radiance calibration, is described in this issue by Slijkhuis (1996).

The structure of this paper is as follows. In Section 2 the GOME data used for validation are briefly described. In Section 3 the DAK model is introduced. The polarisation validation is reported in Section 4 and the radiance validation in Section 5. Conclusions

are given in Section 6.

## 2 Description of GOME data

### 2.1 Overview

Technical information about the GOME instrument and data processing can be found in the GOME Users Manual (ESA, 1995). Here a few relevant details are given. ERS-2 is in a sun-synchronous polar orbit with an equator-crossing time of 10.30 AM (local solar time of the descending node). GOME measures the Earth's radiation by scanning perpendicular to the flight direction from East to West in 4.5 s, and doing an integration every 1.5 s. This leads to three ground pixel types: East (E), Nadir (N), and West (W). The backscan of 1.5 s also involves an integration, which leads to the Backscan (B) pixel. The swath width can in principle be varied between 120 and 960 km; in the validation phase it was 960 km. The integration time (IT) in the validation phase was only 0.375 s instead of the planned 1.5 s, leading to a size of  $80 \times 40 \text{ km}^2$  (across  $\times$  along track), for the E, N, and W pixels, and a size of  $240 \times 40 \text{ km}^2$  for the B pixel. The nadir angles of the viewing directions for the centres of these pixels are, at satellite altitude (about 780 km):  $-13.9^\circ$  (E),  $6.6^\circ$  (N),  $27.3^\circ$  (W), and  $-23.5^\circ$  (B), where the minus sign denotes the eastern side of the nadir direction.

GOME observes the Sun and the Earth in four spectral channels, encompassing the range from about 240 to 790 nm, with 0.2 to 0.4 nm resolution. Each channel is a 1024-element diode-array (Reticon). The dispersion is performed by means of a predisperser prism and gratings. The present radiance validation has been limited to data of spectral channel 1B (307–315 nm), channel 2 (311–405 nm), channel 3 (394–611 nm), and channel 4 (578–794 nm). Here the total ranges are given, which are larger than the useful ranges.

The GOME level 1 data product contains a sun irradiance spectrum in  $\text{W}/(\text{m}^2 \text{ nm})$ , measured once per day, and an Earth radiance spectrum in  $\text{W}/(\text{m}^2 \text{ nm sr})$  for each ground pixel, with the corresponding solar and viewing geometries and geolocation. The polarisation measurements can be found in the level 1 data using an option in the extraction software of the GOME Data Processor (GDP). We used data from 22 and 23 July 1995, which were processed with GDP versions 1.43 and 1.55, respectively.

### 2.2 Polarisation measurements

GOME measures the polarisation of the incoming light by measuring the radiance of two perpendicularly polarised components of the incident light. This is sufficient to correct for the polarisation sensitivity

Table 1: Spectral ranges and effective wavelengths  $\lambda_e$  of the GOME polarisation measurement points in spectral order. The theoretical value  $p_7$  is also listed. PMD=Polarisation Measuring Device, OVL=channel overlap (channel  $i$ /channel  $j$ ).

$p$ point	range (nm)	$\lambda_e$ (nm)	remark
$p_7$	240–300	$\leq 300$	theory
OVL 1 (1B/2)	311–315	313	
PMD 1	300–400	350	
OVL 2 (2/3)	(394–405)	–	low sens.
PMD 2	400–600	490	
OVL 3 (3/4)	578–611	605	
PMD 3	600–800	700	

of the instrument. The polarisation measurements from the three broad-band PMD detectors follow from a combination of the PMD signals with the signals from the spectrally integrated spectral channels. The polarisation measurements from the channel overlaps (OVL) follow from a combination of the signals at the end of one channel and the beginning of the next, using the fact that these have different polarisation sensitivities. The spectral ranges and effective wavelengths of the PMD and OVL polarisation measurements are listed in Table 1. (The polarisation in overlap 2 is in fact missing due to too low sensitivity.)

The incident radiation has a radiance  $I$  which can be regarded as the sum of the radiances of two perpendicularly polarised beams,  $I_p$  and  $I_s$ , where the subscript  $p$  means parallel to the slit direction (equal to the flight direction) and  $s$  means perpendicular to it. The polarisation quantity in the GOME level 1 data is the so-called fractional polarisation along the flight direction, denoted by  $p$  and defined as  $p = I_p/I$ . We may write down two alternative formulations for  $p$  in more usual polarisation quantities:

$$p = (1 - Q/I)/2 \quad (1)$$

$$p = (1 - P \cos 2\chi)/2, \quad (2)$$

where  $P = \sqrt{Q^2 + U^2}/I$  is the degree of linear polarisation and  $\chi = \frac{1}{2} \arctan(U/Q)$  is the direction of polarisation ( $0^\circ \leq \chi < 180^\circ$ ).  $I$ ,  $Q$  and  $U$  are the Stokes parameters as defined by e.g. Van de Hulst (1957); the plane of reference chosen here is the local meridian plane, containing the local nadir and the viewing direction. Note that unpolarised light has  $p = 0.5$ . The more  $p$  is deviating from 0.5, the larger the degree of polarisation (assuming that the direction of polarisation remains unchanged).

In addition to the six polarisation measurement points, there is a so-called seventh polarisation point, denoted by  $p_7$ , which is determined from theory

assuming single scattering by molecules (Stammes, 1994a). From extensive multiple scattering calculations with DAK it has been found that this assumption holds for  $\lambda < 300$  nm if there is not a high aerosol loading in the stratosphere. The seventh point  $p_7$  is calculated from Eq. (2) by assuming that the degree and the direction of linear polarisation are due to single scattering (s.s.) by molecules.  $P_{s.s.}$  and  $\chi_{s.s.}$  only depend on the viewing and solar geometry, so  $p_7$  can be calculated straightforwardly in the GOME data processing (cf. Stammes, 1994a).

### 2.3 Polarisation-correction

In order to derive the radiance  $I$  (level 1 data) from the measured signal  $S$  (level 0 data in counts/s), the GDP performs two main calibration steps: (1) polarisation correction by transforming the polarised signal  $S_{pol}$  into an unpolarised signal  $S_{unpol}$ , and (2) radiance calibration by transforming  $S_{unpol}$  into  $I$ . We here give the main polarisation correction formula, to indicate how the GOME polarisation measurements are used in the data processing:

$$S_{unpol} = S_{pol} \frac{1}{2} \frac{1 + \eta}{p(1 - \eta) + \eta}, \quad (3)$$

where  $\eta$  is the polarisation sensitivity ratio of the GOME instrument, which is strongly wavelength-dependent (see, e.g., ESA, 1995, Fig. 6.4-2).

The above formula must be applied to the signal at each array detector wavelength. This means that the  $p$  data points, including  $p_7$ , must be interpolated in  $\lambda$  (see Spurr, 1994).

## 3 Radiative transfer model

The radiative transfer model DAK used here for validation purposes, is an application of the doubling-adding method to polarised radiative transfer in the Earth's atmosphere. The doubling-adding method is an accurate method to solve multiple scattering in a plane-parallel atmosphere (Van de Hulst, 1980). The extension of the method to include polarisation has been described by De Haan et al. (1987). The DAK model consists of an atmospheric shell around a doubling-adding radiative transfer kernel (Stammes, 1994b).

Before we will consider the actual polarisation measurements of GOME, we first show in Fig. 1 the expected spectral behaviour of the fractional polarisation  $p$ , as calculated with DAK for a simple case. Figure 1 shows  $p(\lambda)$  for nadir view of a clear sky atmosphere, containing only molecules and ozone, with a Lambertian surface albedo  $A_g = 0.05$ . The solar zenith angle has three values:  $30^\circ$ ,  $60^\circ$ , and  $75^\circ$ , and the relative azimuth between viewing and solar direction is assumed to be  $0^\circ$ . Note that the line  $p = 0.5$

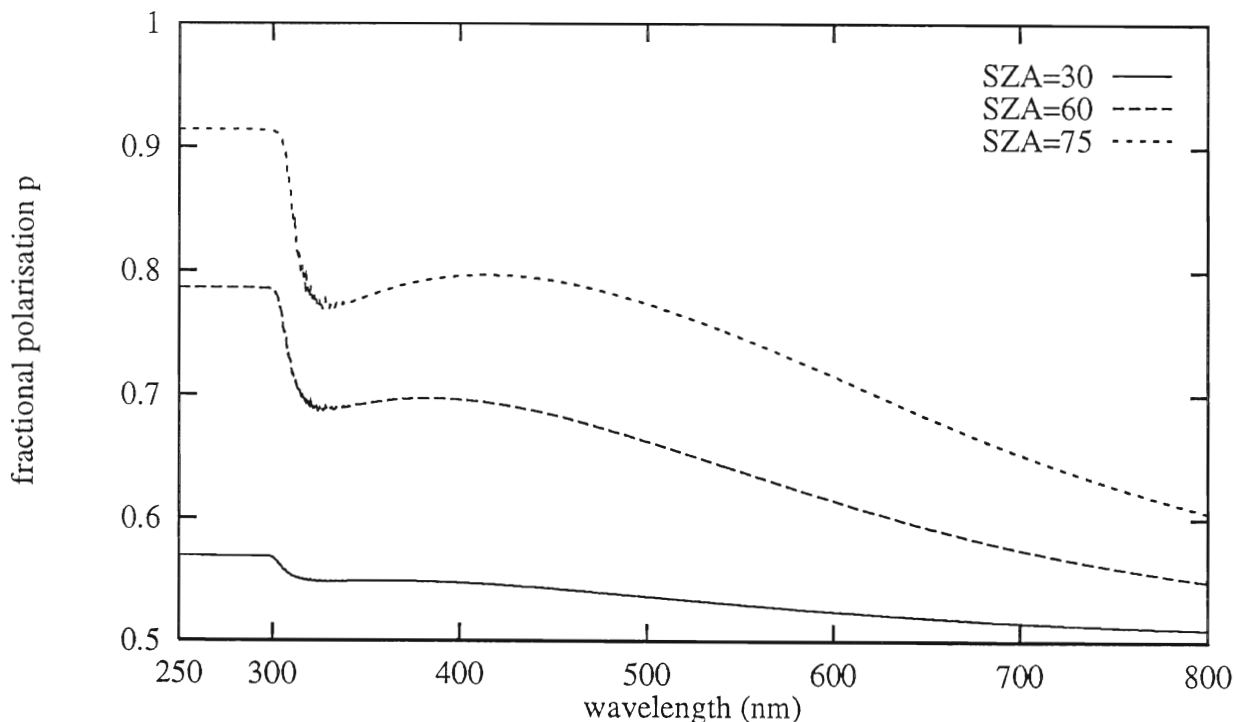


Figure 1: Fractional polarisation  $p(\lambda)$  as calculated by the DAK model for nadir view and three solar zenith angles (SZA); the relative azimuth is  $0^\circ$  (solar direction in the plane of scanning). Atmospheric model: Mid-Latitude-Summer, with only molecular scattering and ozone absorption; no aerosol or clouds present. Surface albedo is 0.05.

denotes unpolarised light, or polarised light having  $\chi = 45^\circ$  or  $135^\circ$ . The behaviour of  $p(\lambda)$  is flat below about 300 nm, then steeply falls off until about 320–330 nm, and is rather smoothly rising and then decreasing at the larger wavelengths. The small wiggles around 320 nm are due to the ozone Huggins bands. When aerosol is added to the atmosphere the general behaviour of  $p$  does not change much, but in general  $p$  becomes closer to 0.5. When the surface albedo is increased, the drop of  $p$  in the UV becomes steeper, and  $p$  becomes closer to 0.5 (i.e. unpolarised light) at the larger wavelengths. It should be noted that in this figure the single scattering polarisation value  $p_7$  would be indistinguishable from  $p$  at 290 nm.

## 4 Polarisation validation

We will first give an impression of the GOME polarisation measurements by considering the variation of  $p$  along an orbit. Next we will look into the polarisation measurements of a selected pixel, and compare those with model results.

### 4.1 Polarisation along an orbit

As an example of the PMD polarisation measurements, Figure 2 shows  $p$  versus latitude on 23 July 1995, orbit 1337 (pixels 1 to 1200, Nadir type). This part of the orbit was entirely above the Atlantic Ocean (see the PMD cloud image in Koelemeijer et al., 1996, this issue). In this case the scene is simple: clear and cloudy sky above a dark ocean. The three PMD curves follow each other nicely, and, apart from the peaks, they approximately follow the shape of the theoretical curve of  $p_7$ . The curves for  $p_7$  and the PMDs are in the correct spectral order for a low sun (latitude below about  $30^\circ$  S):  $p_7$  has the largest deviation from 0.5, then PMD1, PMD2, and PMD3. PMD3 usually has the largest peaks, which may occur due to clouds or aerosol in the boundary layer, or surface reflection. PMD1 is less affected by these effects, because it is more sensitive to molecular scattering than PMD3. Generally, the PMD polarisation measurements show reasonable values and behaviour along the orbit. For other orbits we found a similar behaviour.

The corresponding OVL1 and OVL2 polarisation measurements of this orbit are very poor: of the considered 1200 groundpixels OVL1 yielded only 5 (strongly deviating) data points, whereas OVL2 yielded no data points at all (which was expected). On the other hand, OVL3 yielded about 1000 data points, of which the Nadir pixel values are shown in Fig. 3. However, these overlap polarisation data cannot be trusted, since their variability is unphysically

large. A similar behaviour of the overlap polarisation measurements was found for other orbits.

### 4.2 Polarisation for a selected pixel

As an example of the GOME spectral polarisation measurements for one pixel, we chose a cloudless pixel measured on 22 July 1995, orbit 1322, over the North Sea. This pixel was cloudless according to the Meteosat image close to the time of overpass and the GOME level 2 cloud product. Figure 4 shows the three PMD polarisation points and  $p_7$  together with DAK calculations of  $p(\lambda)$ . In the calculations the albedo of the (Lambertian) sea surface was varied. One of the calculations was done for a spectrally dependent albedo measured on the North Sea (Althuis and Shimwell, 1994); the others were done for a constant albedo. Clearly, even small albedo changes have an appreciable influence on the polarisation of a clear pixel. Without aerosol the correct spectral behaviour could not be reproduced; the largest deviations occurred for the sea albedo case and the  $A_g = 0$  case. The addition of aerosol, of maritime type in the boundary layer and background type for free troposphere and stratosphere, led to a much improved fit. Here the aerosol was assumed to be polarising according to Mie theory and to have a total aerosol optical thickness of 0.13 at 550 nm. From this and similar analyses we conclude that the GOME polarisation measurements of clear ocean pixels can be well interpreted in terms of a realistic sea surface albedo and aerosol parameters.

## 5 Radiance validation

Next the GOME radiance measurements were investigated. Only data from channels 1B to 4 ( $\lambda \geq 307$  nm) with  $IT=0.375$  s were considered; data from channel 1A ( $\lambda < 307$  nm), which has a longer  $IT$ , were neglected. Furthermore, the part of channel 3 between 405 and 416 nm has been omitted, because of an anomalously steep spectral behaviour due to instrument calibration problems.

For atmospheric studies a more useful quantity than the radiance is the reflectivity  $R$ , which is defined as  $\pi$  times the Earth's radiance  $I$  divided by the solar irradiance at the top-of-the-atmosphere (TOA), and can be written as:

$$R = I/(\mu_0 F) \quad (4)$$

where  $\pi F$  is the solar irradiance perpendicular to the solar direction (as measured by GOME) and  $\mu_0$  is the cosine of the solar zenith angle.

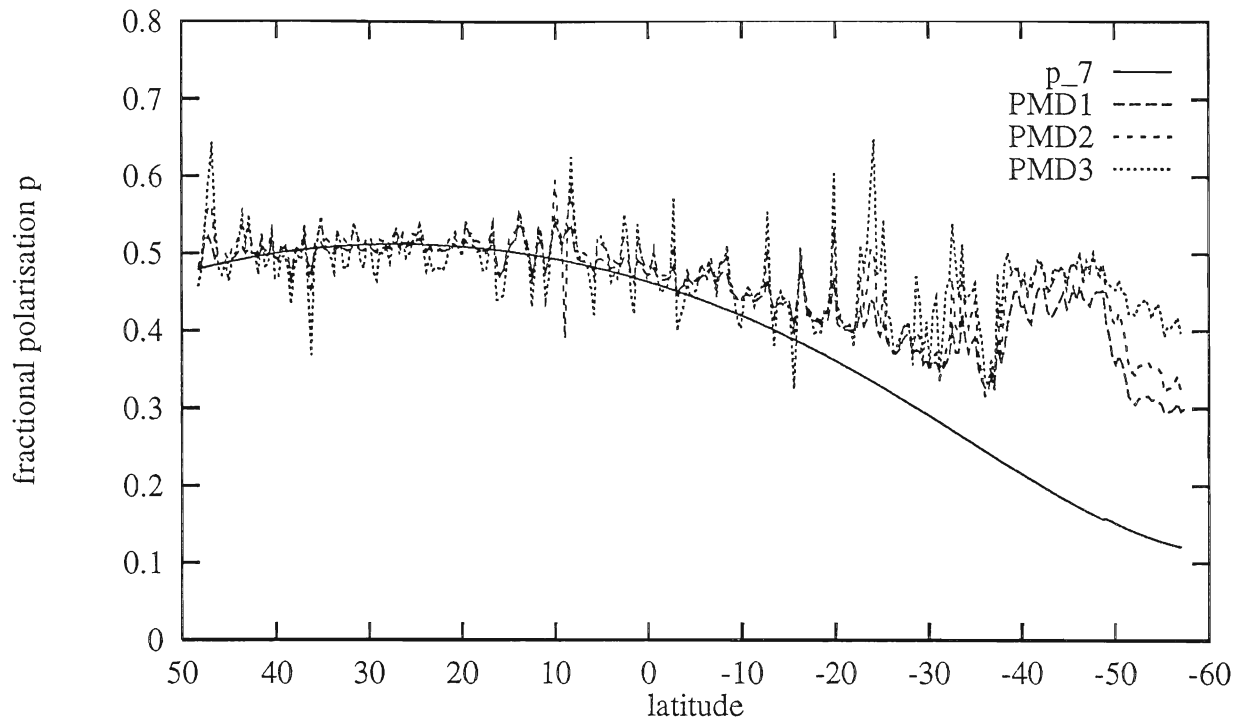


Figure 2: Fractional polarisation  $p$  as a function of latitude (+=North, -=South) as measured by the GOME PMDs on 23 July 1995, orbit 1337. Only nadir pixel data are shown. The curve of the theoretical value  $p_7$  is also given. All pixels were above the Atlantic Ocean.

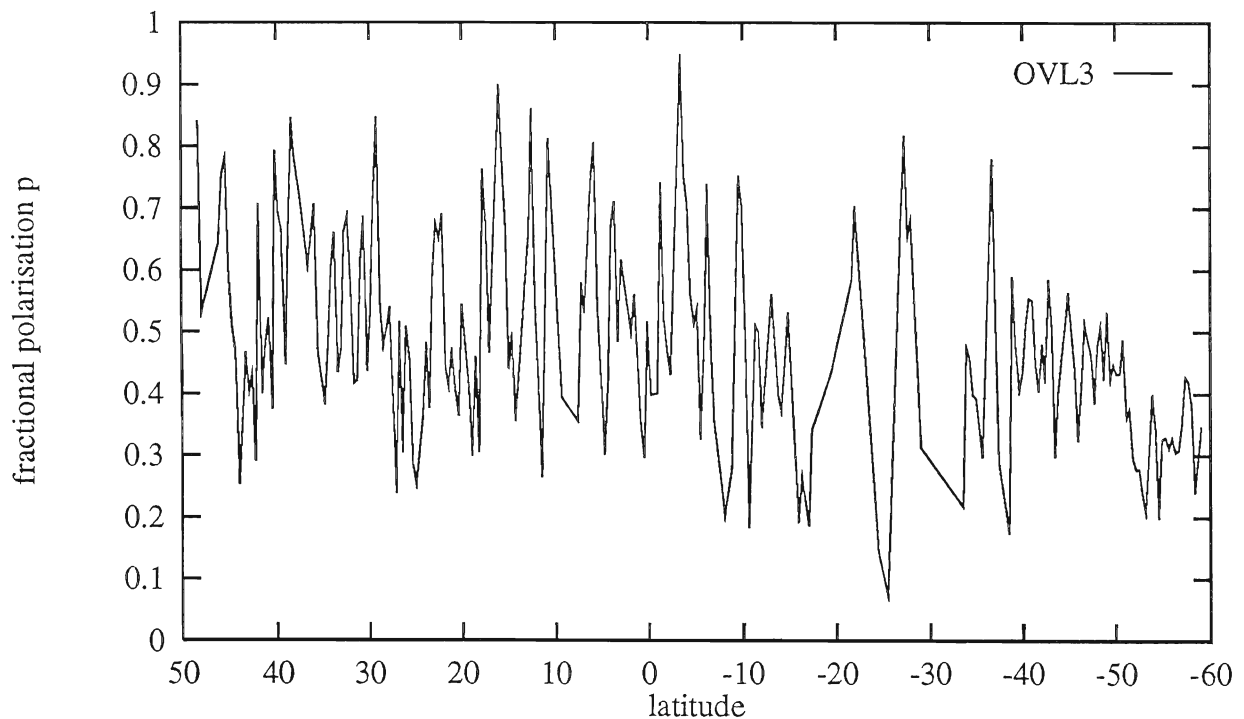


Figure 3: Same as Fig. 2, but for the OVL3 fractional polarisation.



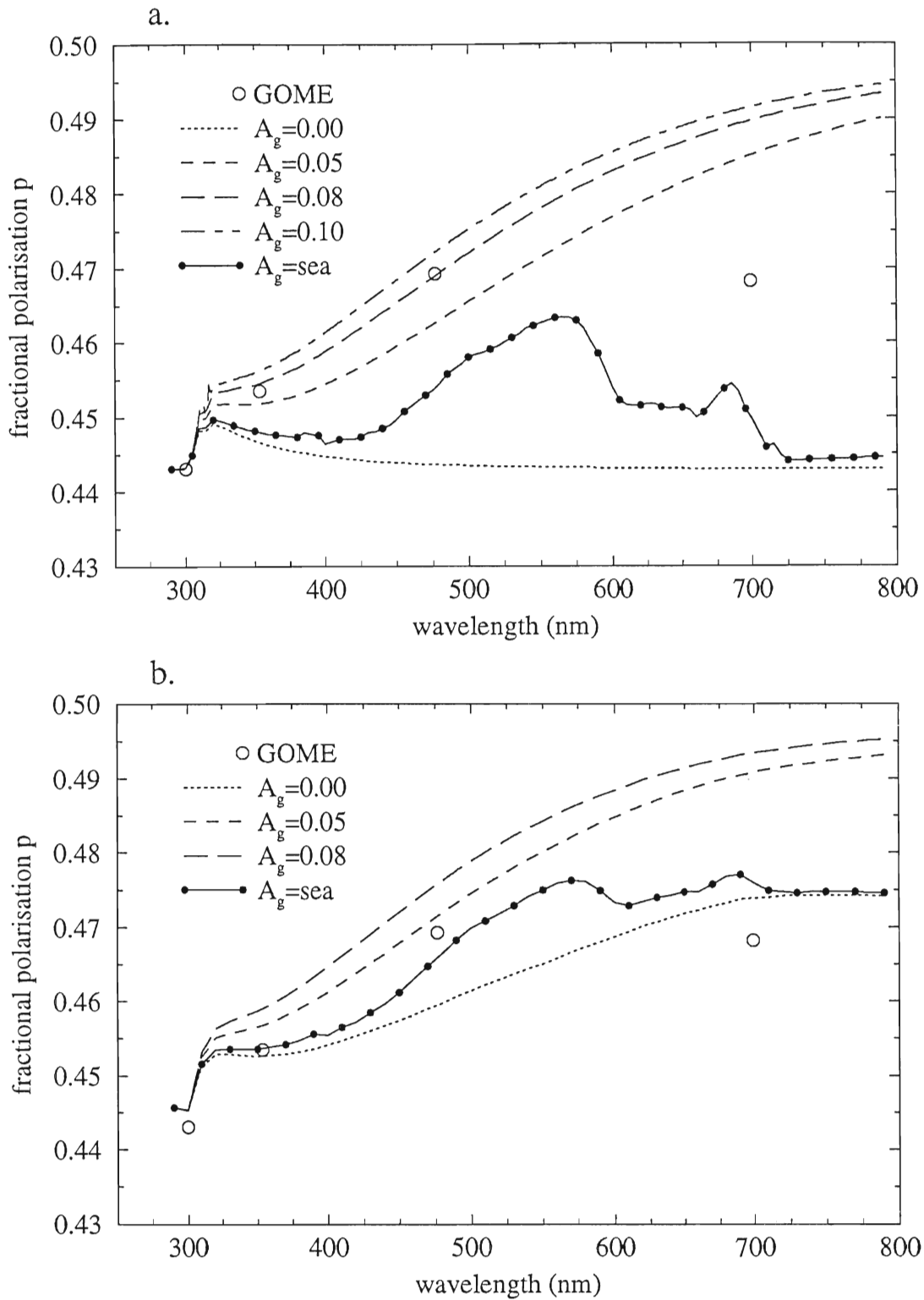


Figure 4: Spectral behaviour of the fractional polarisation  $p$  of a cloudless pixel on the North Sea as measured by the GOME PMDs together with calculated curves from the DAK model.  $p_7$  is shown as a GOME data point. Data belong to pixel 785 (W) of orbit 1322 on 22 July 1995. Location: 55° N, 2° E; SZA=35°. (a) Calculations without aerosol (only molecular scattering, ozone absorption, and sea reflection). The sea albedo,  $A_g$ , is varied;  $A_g = \text{sea}$  denotes a spectrally dependent sea albedo. (b) Calculations include maritime aerosol in the boundary layer and background upper tropospheric and stratospheric aerosol; total aerosol optical thickness is 0.13 at 550 nm.

## 5.1 Occurrence of jumps

Reflectivity spectra for various scene types were investigated. Spectra of clear pixels over ocean and land looked generally as expected, but the spectra of some cloudy pixels showed jumps between the spectral channels. In Fig. 5 the spectra of two “normal” cloudy pixels over land are shown. This is the expected spectral shape for a cloudy scene: a flat, “white” reflectivity spectrum. Note the numerous gaseous absorption features, e.g. the steep rise below 300 nm due to the ozone Huggins band, the broad depression around 600 nm due to the ozone Chappuis band, the oxygen B-band at 687 nm, the water vapour band around 720 nm, and the deep oxygen A-band at 761 nm. As an example of spectra with jumps, Fig. 6 shows the spectra of two other cloudy pixels over land. Here the reflectivities measured by spectral channels 2 and 3 do not match going from 405 to 416 nm, and those measured by channels 3 and 4 do not match around 605 nm. Channel-to-channel continuity of  $R$  is of course a basic requirement for the GOME data. A further investigation showed that these channel-to-channel jumps occurred frequently and not only for cloudy (i.e. high reflectivity) scenes. As an illustration of this, Fig. 7 shows the jumps at 605 nm for orbit 1337 (the first 1200 pixels), expressed as the ratio of the reflectivities of channels 3 and 4 at 605 nm. A ratio of 1 means no jump. Apparently, jumps occur all over the orbit and in both directions. They reach in this case as high as 40–80 %.

## 5.2 Explanation of jumps

An extensive investigation was performed to find the cause of these reflectivity jumps. Correlations with other measurements and parameters were investigated, and some suggested explanations could be excluded:

- (1) The solar irradiance spectrum did not show significant jumps, so the cause was the Earth’s radiance spectrum.
- (2) The GDP level 0–1 data processing did not show bugs. This was found by comparing measured GOME level 0 data (uncalibrated counts) with calculated level 0 data, as generated by the GOME Instrument Simulator (Slijkhuis, 1995) using level 1 radiances as input.
- (3) An error in the key data, especially in the  $\eta$ -function, would cause a systematic jump, which is not found. It is known that the  $\eta$ -function suffers from an uncertainty, especially in the overlap regions, due to the fact that it was not measured in vacuum. Systematically deviating reflectivities in the overlaps between channels 1B and 2 (around 313 nm) and between channels 2 and 3 (around 400 nm) are indeed observed. However, the observed jumps are not lim-

ited to the overlap regions, but cover a large spectral range.

- (4) No correlation of the jumps was found with the PMD  $p$  measurements, nor the  $p_7$  value, nor the reflectivity at 755 nm (i.e. no correlation with scene brightness).

- (5) The jumps at OVL2 correlated with the jumps at OVL3.

- (6) A strong correlation was found between the jump at 605 nm and the OVL3 polarisation, which is illustrated by Fig. 8. This suggests that both problems, the radiance jumps and the unreliable overlap polarisations, have the same cause.

The most probable explanation of the jumps, which was suggested by TPD and ESTEC, is the *serial read-out* of the array channels. Each Reticon array is read out serially, with a time difference of 0.094 s between the first and last diode; different channels are read-out simultaneously (details are given by Calles and Lefebvre, 1996). This means that, for a 960 km swath, the scenes seen by the first and last diodes are shifted 20 km across-track in the forward scan (80 km in the backscan). For ground pixels of 80 km across-track (240 km backscan) due to the 0.375 s integration time, this is a 25 % scene difference. This can introduce large radiance differences caused by e.g. broken clouds or surface inhomogeneities. The scene differences can be most clearly seen at the overlaps, where the last diodes of one array are compared to the first diodes of another array. The serial read-out also explains the erratic overlap polarisations: if the radiances at the end of one channel and the start of the next do not belong to the same scene, then the measured overlap polarisation is useless. An observation which supports the above explanation of the jumps, is that over homogeneous scenes, such as the Sahara or fully cloud covered areas, no jumps or only small jumps are found. For example, the small jumps in Fig. 7 for pixel number  $> 1000$  hold for the cloudy region at the lower end of orbit 1337, as shown in the PMD image of Koelemeijer et al. (1996, this issue).

The jumps will probably be reduced when the integration time of channels 1B to 4 is increased to 1.5 s, by means of co-adding four pixels of 0.375 s integration time in-orbit.

## 6 Conclusions

The GOME polarisation and radiance measurements have been validated by means of consistency checks, comparisons with single scattering theory, and comparisons with the polarised radiative transfer model DAK. The conclusions and recommendations that have been reached are given below in two parts.

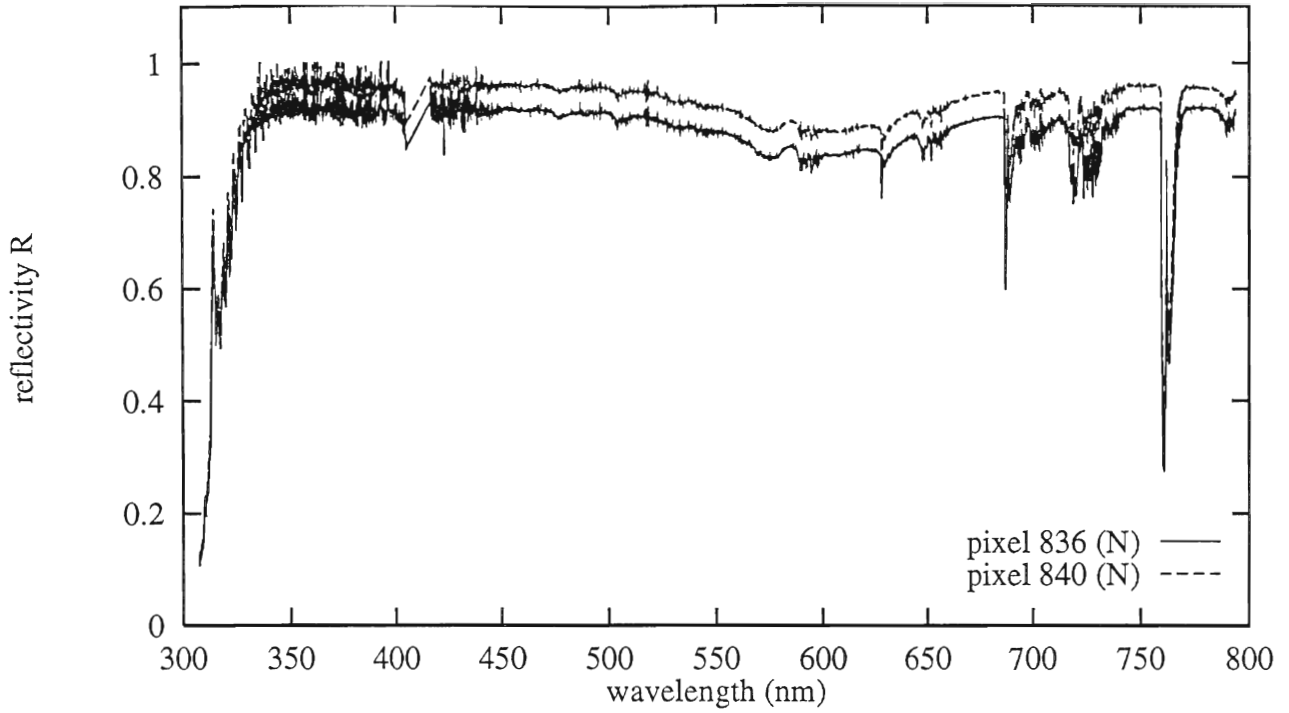


Figure 5: Spectral reflectivity of two adjacent cloudy pixels over land. Date: 22 July 1995, pixels 836 and 840 (N) of orbit 1322. SZA=31°. Location: 50° N, 5° E (Belgium).

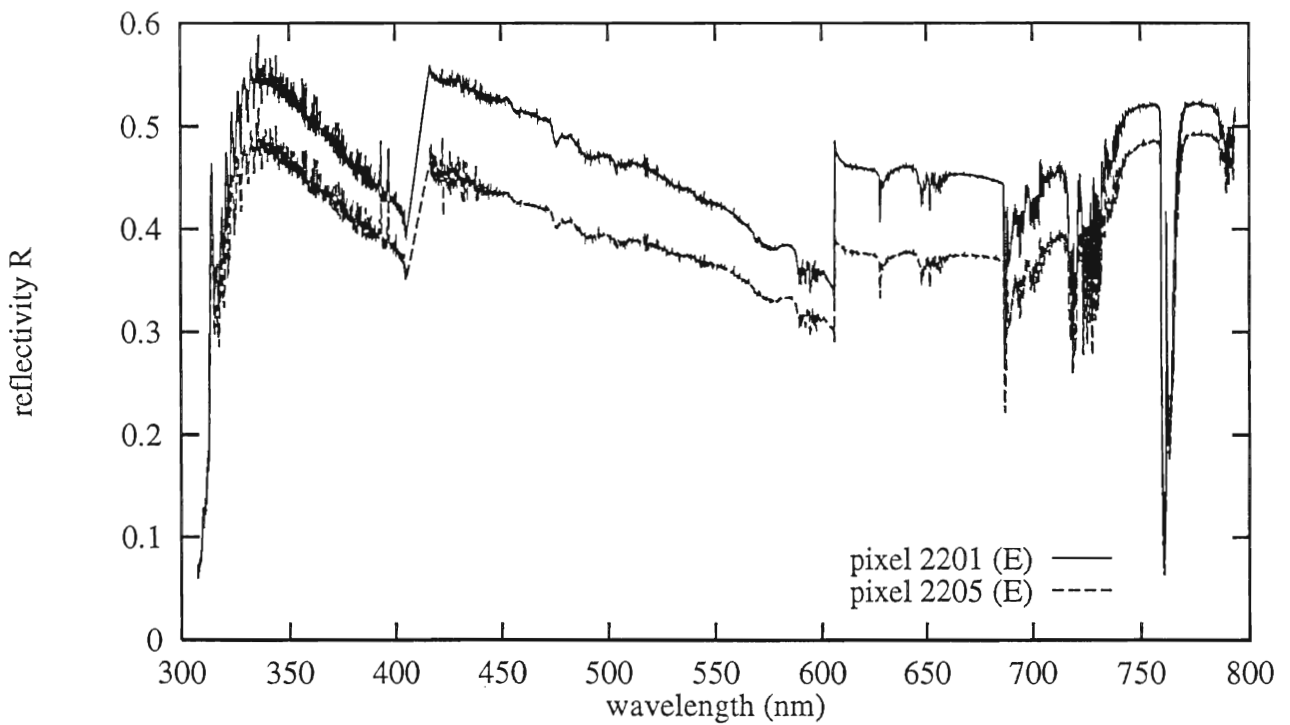


Figure 6: Spectral reflectivity of two adjacent cloudy pixels over land. Date: 23 July 1995, pixels 2201 and 2205 (E) of orbit 1335. SZA=30°. Location: 48° N, 16° E (Middle-Europe).

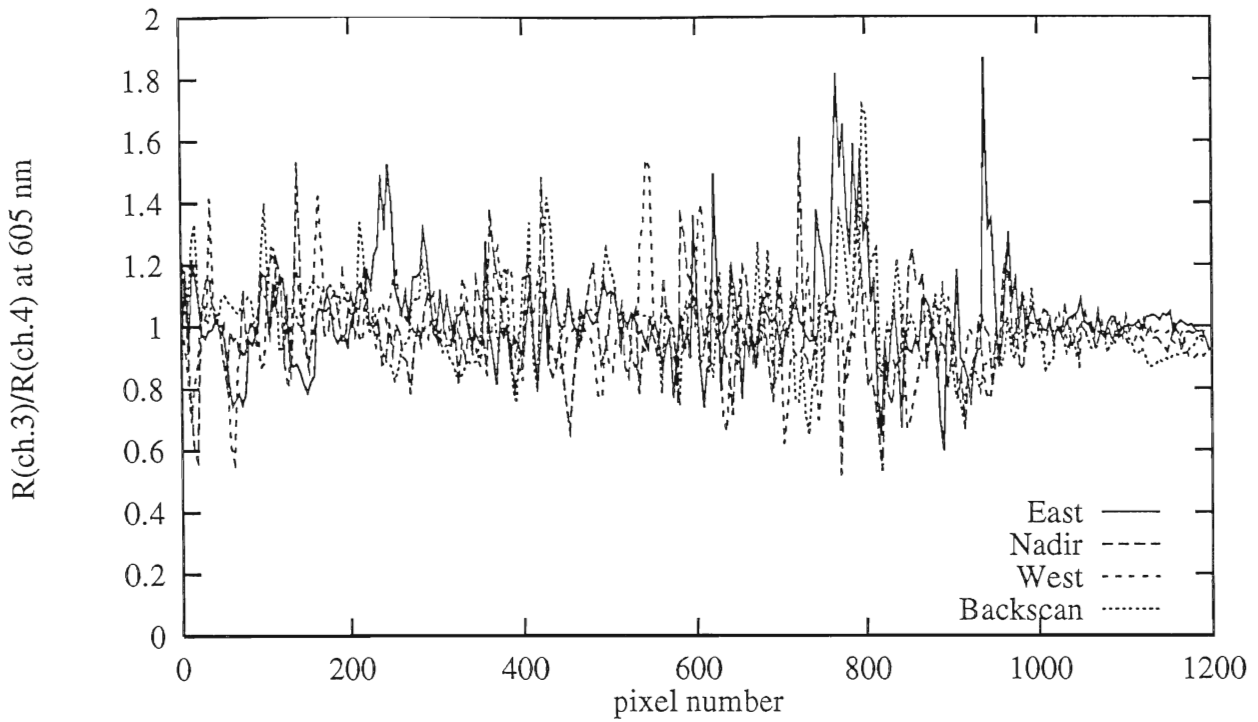


Figure 7: Reflectivity jumps between channels 3 and 4 at 605 nm, defined as  $R(\text{channel } 3)/R(\text{channel } 4)$ , for the first 1200 ground pixels of orbit 1337 on 23 July 1995 (same orbit as shown in Figs. 2 and 3). The four curves belong to the four pixel types.

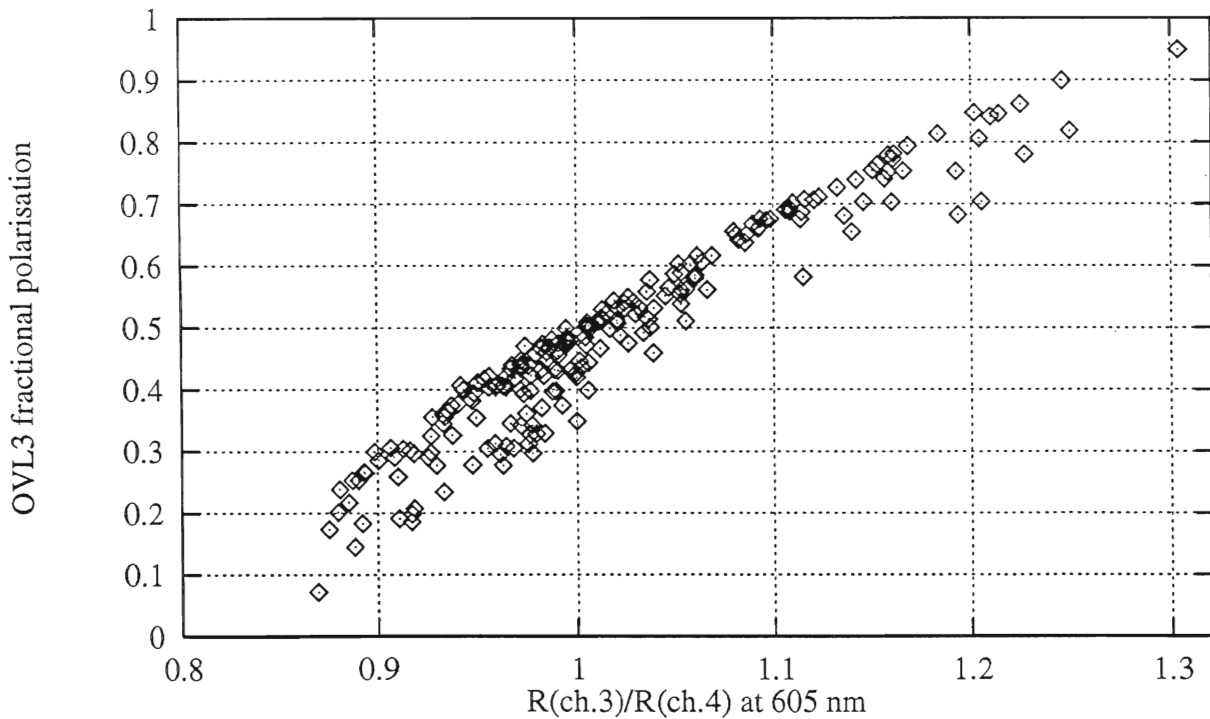


Figure 8: Correlation between the reflectivity jumps at 605 nm and the OVL3 fractional polarisations for the nadir pixels of Fig. 7.

## 6.1 Polarisation validation

1. The fractional polarisations measured by the PMDs are overall consistent with single and multiple scattering models.
2. The calculation of the theoretical fractional polarisation,  $p_7$ , is being performed correctly.
3. The OVL1 fractional polarisation is almost always absent or strongly deviating.
4. The OVL3 fractional polarisation is often deviating from the PMD2 and PMD3 values, and attains sometimes unphysical values. The problem with the overlap  $p$ -values is strongly correlated with the channel-to-channel radiance jumps (see below).
5. On the basis of an analysis involving pixels with a special geometry (so-called  $\cos 2\chi_{s.s.} = 0$  points), systematic and random errors on the  $p$ -values of the PMDs were found. These errors are reported and discussed in this issue by Aben et al. (1996).
6. Polarisation correction of the GOME radiances should be performed on the basis of the three PMD  $p$ -values and  $p_7$ . The overlap polarisations should not be used.

## 6.2 Radiance validation

1. At the overlaps of the channels 2, 3, and 4 often jumps in the radiance (or reflectivity) occur, which may be tens of percent. The jumps at OVL3 are strongly correlated with the  $p$  values of OVL3.
2. The main cause of these jumps is the difference in scene observed by the detector diodes at either side of the overlap due to the serial read-out of the four diode-array detectors. It takes 0.094 s between the read-out of the first and the last diode of an array. This is 1/4-th of the integration time of 0.375 s used in the GOME validation phase. Hence the diodes at the end of one channel and at the beginning of the next, share only 75 % of their field-of-views. In case of inhomogeneous scenes (e.g. cloudy scenes) large jumps in reflectivity may occur. For homogeneous scenes (e.g. Sahara) it has been observed that the jumps are smaller. A secondary cause is the difference in instantaneous field-of-view between detector pixels. This has been noted in the on-ground calibration, and during solar observation (see Slijkhuis, 1996).
3. Apart from the jumps, the reflectivity spectra are qualitatively correct. Many spectral features can be discovered, e.g. those of trace gases, vegetation, soil, aerosols, clouds, and Ring effect.
4. For spectral studies involving a large GOME wavelength range, or spectral studies needing absolutely calibrated radiances, spectra should be checked for jumps. This is a check for spectral integrity.

## Acknowledgements

The work presented here was performed in the framework of GOME validation project NL-109. ESA and DLR (Oberpfaffenhofen) have kindly provided help with using the GOME data and processing software. Discussions with J.F. de Haan, J.W. Hovenier, and W.J. Knibbe of Vrije Universiteit Amsterdam and S. Slijkhuis of SRON are gratefully acknowledged. The work was partly funded by Space Research Organization Netherlands (SRON) through project EO-009.

## References

- Aben, I., M. Dobber, D.M. Stam, P. Stammes, 1996, "Error analysis of polarisation measurements by GOME", this issue \*
- Althuis, W., and Shimwell, 1994, "Interpretation of remote sensing imagery for suspended matter monitoring in Coastal waters", EARSeL workshop on Remote sensing, GIS and Coastal Zone Management, 24-26 October 1994, Delft, The Netherlands
- Callies, J., Lefebvre, A., 1996, "GOME PMD reading timing", Fax of 11 Jan. 1996, Ref. LTP/0271/JC-uu, ESTEC, Noordwijk
- De Haan, J.F., P.B. Bosma, and J.W. Hovenier, 1987, "The adding method for multiple scattering calculations of polarized light", *Astron. Astrophys.* **183**, 371-391
- ESA, 1993, *GOME Interim Science Report*, ESA SP-1151, ESA/ESTEC, Noordwijk
- ESA, 1995, *GOME Users Manual*, ESA SP-1182, ESA/ESTEC, Noordwijk
- Koelemeijer, R.B.A., P. Stammes, A.J. Feijt, A.C.A.P. van Lammeren, 1996, "First validation of GOME cloud observations", this issue \*
- Slijkhuis, S., 1996, "GOME instrument properties affecting the calibration of radiance and polarisation", this issue \*
- Slijkhuis, S., 1995, "GOME/SCIAMACHY Instrument Simulation Software", Report GO/SCIA-IS-TR01, SRON, Utrecht
- Spurr, R., 1994, "GOME level 0 to 1 algorithms description", Report ER-TN-DLR-GO-0022, Issue 3A, DLR/DFD, Oberpfaffenhofen
- Stammes, P., 1994a, "The seventh point polarisation algorithm", Internal Report, KNMI, De Bilt
- Stammes, P., 1994b, "Errors in UV reflectivity and albedo calculations due to neglecting polarisation", SPIE Proceedings Vol. 2311, *Atmospheric Sensing and Modeling*, 227-235
- Van de Hulst, H.C., 1957, *Light scattering by small particles*, J. Wiley & Sons, New York (also: Dover, 1981)
- Van de Hulst, H.C., 1980, *Multiple Light Scattering, Tables, Formulas, and Applications, Volume 1 and 2*, Academic Press, New York

---

\* Proceedings of the GOME Geophysical Validation Campaign, ESA WPP-108, ESA/ESTEC, Noordwijk (1996)



# CHAPTER 3

## ERROR ANALYSIS OF POLARISATION MEASUREMENTS BY GOME

I. Aben<sup>1</sup>, M.R. Dobber<sup>1</sup>, D.M. Stam<sup>2</sup> and P. Stammes<sup>2</sup>

<sup>1</sup>) Space Research Organization Netherlands (SRON)  
Sorbonnelaan 2, 3584 CA Utrecht, The Netherlands

<sup>2</sup>) Royal Netherlands Meteorological Institute (KNMI)  
P.O. Box 201, 3730 AE De Bilt, The Netherlands

### ABSTRACT

At defined locations along the GOME orbit the geometrical conditions are such that the fractional polarisation, which is measured by GOME, can be predicted from the illumination and viewing geometry only. Deviations from this predicted value at these locations are used to assess the systematic and random errors of the polarisation measurements of the Earth by GOME. Only PMD polarisation measurements are considered, as the polarisation measurements obtained from the spectral overlap regions are not considered reliable at present. The analysis is applied separately to data corresponding to large ground pixels of size 40 x 80 km<sup>2</sup> (along x across track) and to small ground pixels of size 52 x 2 km<sup>2</sup>.

The systematic errors in fractional polarisation determined in this way are less than 0.02, thus less than a few percent. The resulting relative error in the radiances will be of similar magnitude. The systematic errors deduced for the two different sizes of ground pixels are very similar and suggest the need for out-of-band straylight correction for PMD 1 and PMD 2.

Furthermore, it is shown that the random errors in fractional polarisation for the large ground pixels are 1 to 2 orders of magnitude larger than those obtained for the small ground pixels. This is due to variation of the illumination and viewing geometry, and scene across the ground pixels. Such a variation is clearly more pronounced for the larger ground pixels. The random errors for the small ground pixels are the worst for PMD 3 but are still less than 1 %. This observed random error for PMD3 is most likely related to assumptions concerning the out-of-band straylight correction used in the level 0→1 polarisation correction algorithm.

An orbit propagator was used to derive the variation of geometrical parameters across ground pixels. Single scattering theory for molecules was then used to determine variations across ground pixels of the

polarisation characteristics of atmospheric light at short wavelengths ( $\lambda \leq 300$  nm) as observed by GOME.

### 1. INTRODUCTION

GOME has been designed to measure accurately the Earth's radiance from 240 to 790 nm. However, GOME is a polarisation-sensitive instrument and the atmospheric spectrum of the Earth is in general polarised. To correct for its polarisation-sensitivity, GOME measures the polarisation in six wavelength bands by means of three Polarisation Measuring Devices (PMDs) and by using the three polarisation-sensitive spectral overlap regions. The wavelength bands covered by the three PMDs are for PMD 1 : 295 - 397 nm, for PMD 2 : 397 - 580, and for PMD 3 : 580 - 745 nm. The spectral overlap regions are defined around the cross-over-points where the signals from the two channels are equal. For channel 1-2 overlap the cross-over-point is at  $\lambda = 313.4$  nm and for channel 3-4 overlap at  $\lambda = 606.5$  nm. There is no cross-over-point for the spectral overlap of channel 2-3 [ESA, 1995]. A seventh polarisation point,  $p_7$ , is calculated in the GOME data processing from single Rayleigh scattering by molecules and only depends on the illumination and viewing geometry. This single scattering assumption is valid for atmospheric light in the UV ( $\lambda \leq 300$  nm) [Stammes, 1994a]. An interpolation scheme is used to reproduce the polarisation curve across the entire wavelength range of GOME [DLR, 1995].

This paper presents an analysis to assess the systematic and random errors of the polarisation measurements by GOME and thus validates these measurements. The analysis is based on the identification of locations along the GOME orbit where the polarisation measurements can be predicted based on the illumination and viewing geometry alone.

The method used to assess these errors will be explained in the next section. The errors obtained for data

corresponding to different ground pixel sizes are then summarized. A discussion on possible causes for the observed systematic and random errors is presented thereafter. Finally, a suggestion is made which could improve the PMD 1 and PMD 2 polarisation measurements.

## 2. ANALYSIS METHOD

The amount of circularly polarised light reflected by the Earth's atmosphere is negligible [Coulson, 1988], and therefore only linearly polarised light needs to be considered. Linearly polarised light can be described by the Stokes parameters I, Q and U. The Stokes parameters are defined, relative to any reference plane, as follows [Van de Hulst, 1957] :

$$I = I_0^\circ + I_{90^\circ} \quad (1)$$

$$Q = I_0^\circ - I_{90^\circ} \quad (2)$$

$$U = I_{45^\circ} - I_{135^\circ} \quad (3)$$

where I is the total intensity and Q and U fully represent the linear polarisation. In Eq. (1) - (3) the angles denote the direction of the transmission axis of a linear polariser, relative to the reference plane. The degree of linear polarisation P is given by [Van de Hulst, 1957; Stammes, 1994a] :

$$P = (Q^2 + U^2)^{1/2}/I \quad (4)$$

The direction of polarisation  $\chi$  relative to the reference plane is :

$$\chi = 1/2 \arctan(U/Q) \quad (5)$$

In the following, we choose the local meridian plane as the reference plane, i.e. the plane of the local zenith and the viewing direction.

For polarisation correction purposes, GOME only measures the fractional polarisation p, which is defined as the ratio of the radiance polarised along the entrance slit of GOME to the total radiance. The fractional polarisation p is related to P and  $\chi$  as follows :

$$p = 1/2 (1 - P \cos 2\chi) \quad (6)$$

Both parameters P and  $\chi$ , and thus p, are in principle wavelength-dependent. However, extensive multiple scattering calculations with the polarisation radiative transfer model Doubling-Adding KNMI (DAK) [Stammes, 1994b] have shown that in general  $\chi$  can be

well approximated by its single scattering value,  $\chi_{s.s.}$ . This is illustrated in Figure 1, where  $\chi$  is shown as a function of wavelength for arbitrary ground pixels along GOME orbit 1335, and thus for varying geometries. The single scattering value  $\chi_{s.s.}$  can be calculated directly from the illumination and viewing geometry [Stammes, 1994a], the Sun-Earth-satellite geometry. The degree of polarisation P, however, is a quantity which can vary drastically with wavelength and scene. Therefore, p can vary also with wavelength and scene.

Fortunately, at defined locations along the GOME orbit the geometrical conditions are such that  $\cos 2\chi_{s.s.}$  is exactly zero. From Eq.(6) and the approximation of  $\chi$  by  $\chi_{s.s.}$ , it is clear that at these locations the fractional polarisation p should be equal to 0.5 independent of P, thus for all wavelengths and for any atmospheric condition. When the measured p deviates from 0.5 at these locations, this deviation implies an error in the estimate of p. Results of an analysis based on this principle will be presented in the next section.

## 3. RESULTS

Here results of the  $\cos 2\chi_{s.s.}=0$  analysis are given for polarisation measurements of a number of GOME orbits. Only the PMD polarisation measurements are considered in this study, because the polarisation measurements determined from the spectral overlap regions are presently not reliable. First the behaviour of  $\cos 2\chi_{s.s.}$  is considered.

In Figure 2 the value of  $\cos 2\chi_{s.s.}$  is shown along orbit 1335 of July 23, 1995, as a function of geographical latitude for east, nadir and west pixels. The theoretical fractional polarisation values  $p_7$  (the seventh point) for this orbit are shown in Figure 3. The pixels at the locations where  $\cos 2\chi_{s.s.}=0$ , correspond to the locations in Figure 3 where  $p_7=0.5$ . The integration time for these pixels is 0.375 s and the size of the ground pixel is 40 x 80 km<sup>2</sup>. The jumps in  $\cos 2\chi_{s.s.}$  around 48° S and above 70° N are due to a stepwise increase in integration time for large solar zenith angles. The backscan pixels are not considered as they are larger than the other pixels.

The  $\cos 2\chi_{s.s.}=0$  analysis was first applied to all the available orbits of July 23, 1995. Here 44 pixels were identified to fulfil the  $\cos 2\chi_{s.s.}=0$  condition. The corresponding 44 fractional polarisation measurements for each PMD are plotted in Figure 4. The average deviation of these measurements from  $p=0.5$  (i.e., the systematic error) and their spread (i.e., the random error)

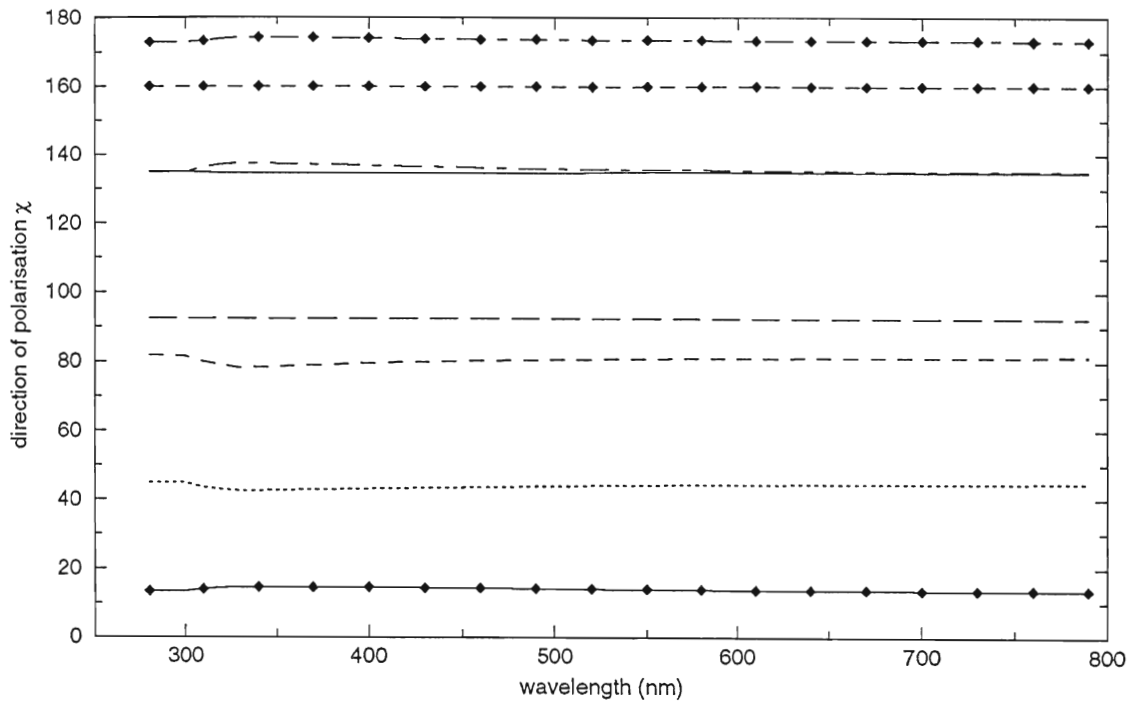


**Figure 1** Direction of polarisation  $\chi$  as a function of wavelength for a number of arbitrary GOME geometries along orbit 1335 July 23, 1995. All calculations were performed for a Midlatitude Summer profile [McClatchey *et al.*, 1972] and a surface albedo of 0.

**Table 1**  
Systematic and random errors in fractional polarisation  $p$  for all orbits of July 23, 1995.

	PMD 1	PMD 2	PMD 3
systematic error	0.005	0.018	-0.003
random error ( $1 \sigma$ )	0.01	0.025	0.06

are tabulated in Table 1.

To study the most homogeneous ground pixels, the same analysis was done for the orbits where the scan mirror was fixed in the nadir position. This is called the nadir static mode. The data obtained in this mode are from July 3, 1995. The integration time is 1.5 s and the size of the ground pixels is  $52 \times 2 \text{ km}^2$  (this results from the IFOV of  $2.87^\circ \times 0.14^\circ$  [ESA, 1995] and the satellite

velocity of 7.5 km/s with respect to the surface). Due to the longer integration time a large number of spectra from this dataset were saturated and could not be used in this analysis. Only 13 measurements for each PMD were used, which are shown in Figure 5. The deviation and spread obtained for these measurements are tabulated in Table 2.

**Table 2**  
Systematic and random errors in  $p$  for the nadir static orbits of July 3, 1995.

	PMD 1	PMD 2	PMD 3
systematic error	0.007	0.012	-0.004
random error ( $1 \sigma$ )	0.0002	0.0002	0.003

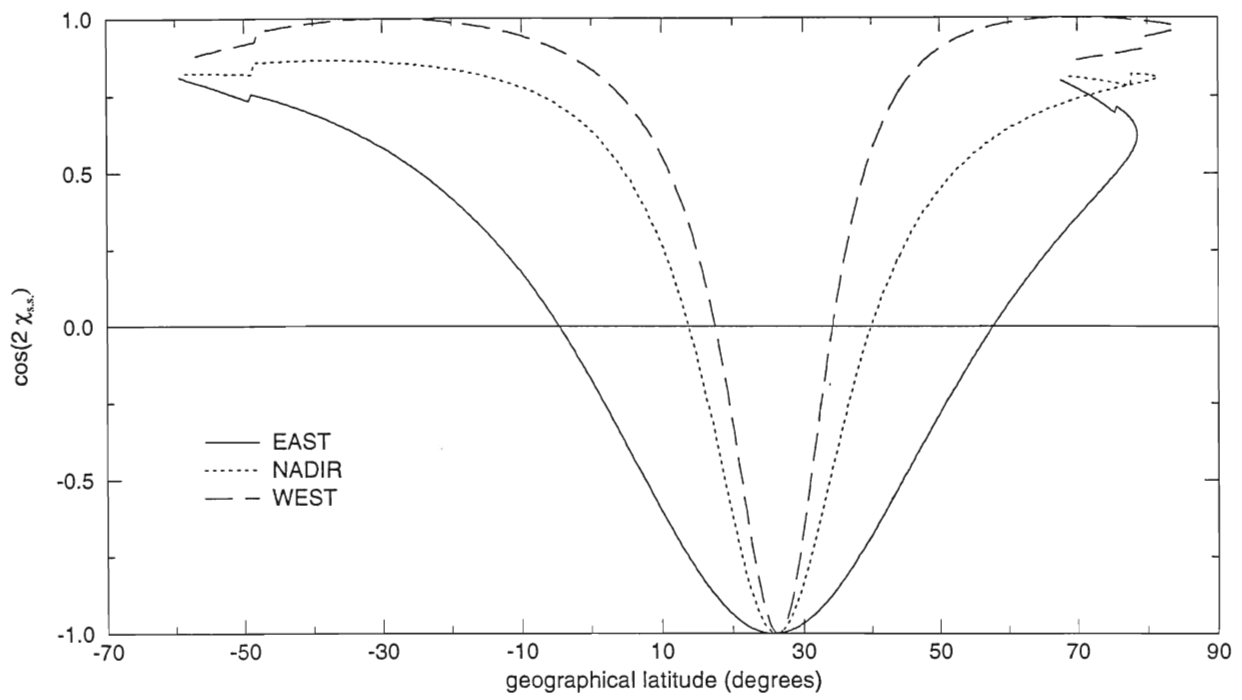


Figure 2  $\cos 2\chi_{s.s.}$  along orbit 1335 July 23, 1995.

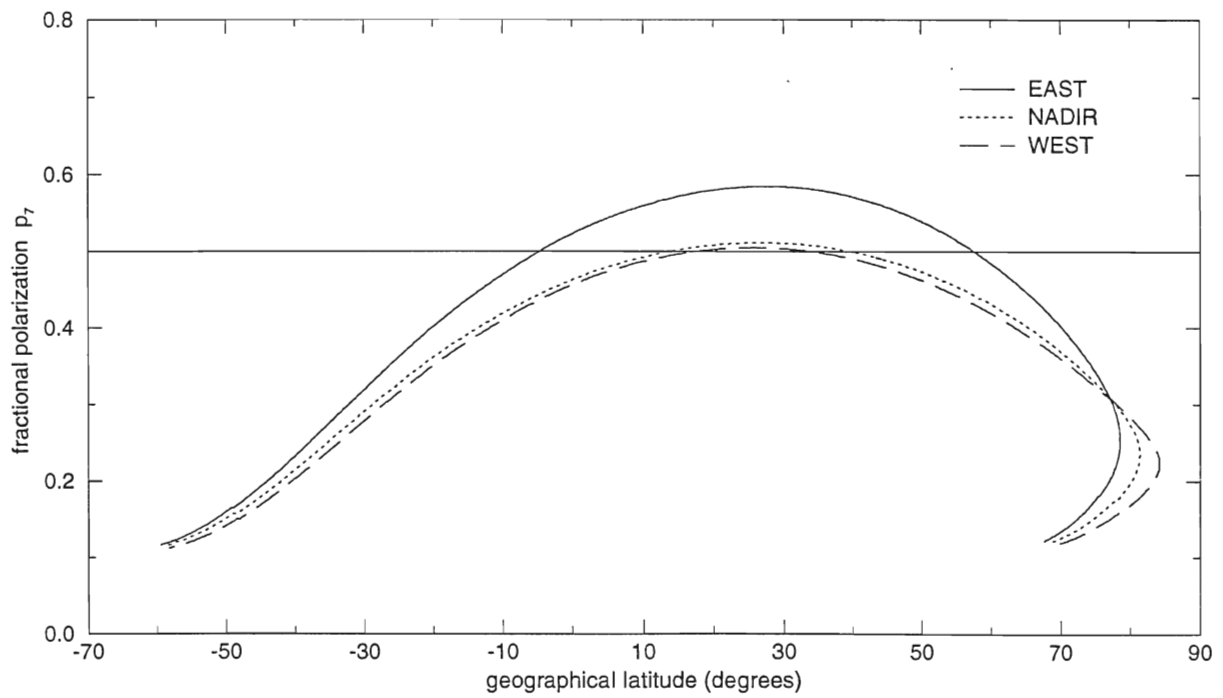


Figure 3 Fractional polarisation  $p_7$  along orbit 1335 July 23, 1995.

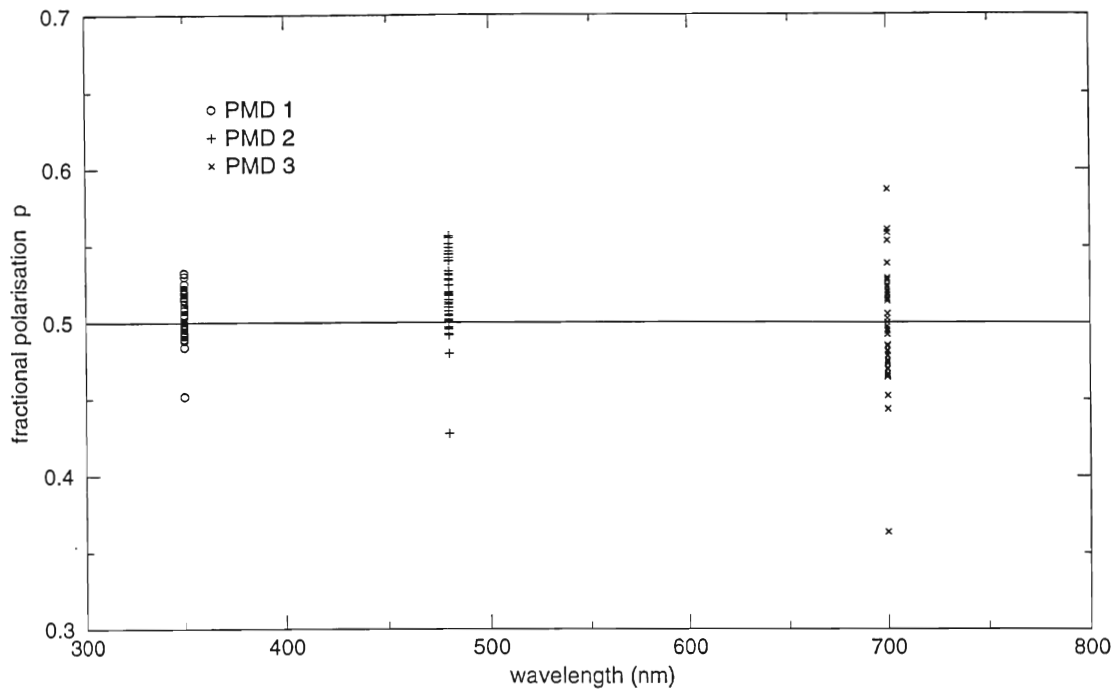


Figure 4 Fractional polarisation  $p$  measured by GOME July 23, 1995, at the  $\cos 2\chi_{s.s.}=0$  locations.

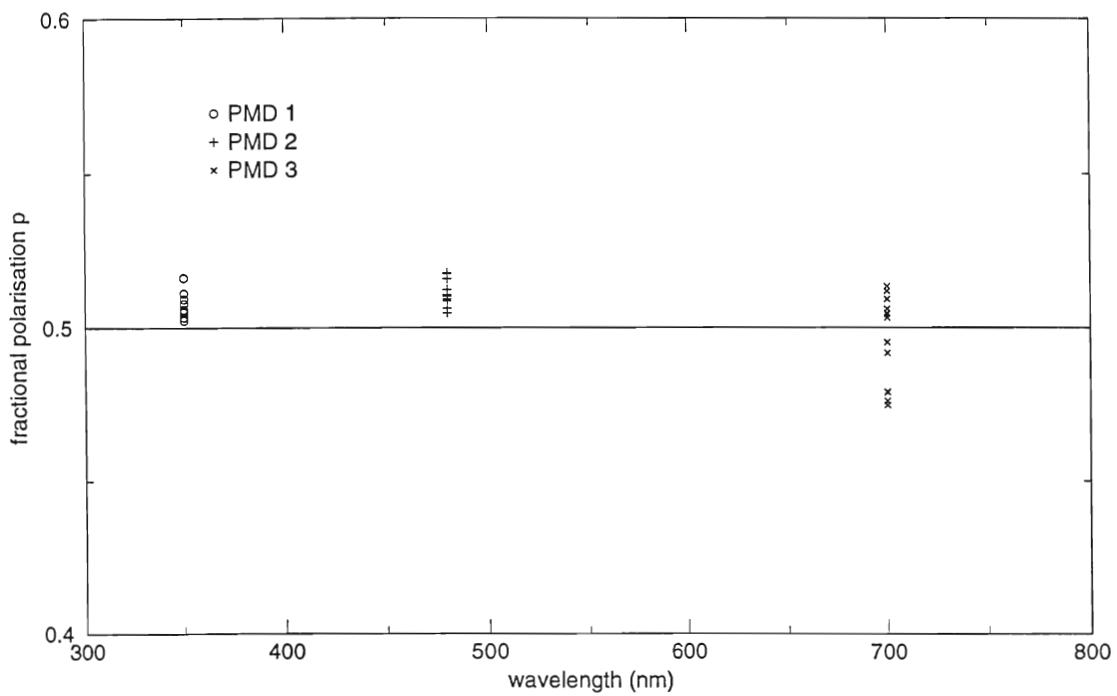


Figure 5 Fractional polarisation  $p$  measured in nadir static mode by GOME July 3, 1995, at the  $\cos 2\chi_{s.s.}=0$  locations.



It can be concluded that for both datasets the systematic errors are largest for PMD 2 and the random errors are largest for PMD 3.

#### 4. DISCUSSION OF ERRORS

##### Systematic errors

The systematic errors for the fractional polarisation  $p$ , as determined in the present paper, are less than a few percent (relative errors). The effect of these systematic errors on the systematic errors of the polarisation corrected Earth spectral radiances are of the same order of magnitude.

The systematic errors deduced for the large and small (static) ground pixels are very similar. This suggests that this error is not caused by phenomena related to the size of the observed scene or its inhomogeneity. Systematic errors as found in the present study, could suggest a slight misorientation of the main polarisation axes of the PMDs relative to the corresponding spectral channels. The measurements by TPD [TPD, 1994a] however, show no evidence to confirm this statement.

Furthermore, it was known that the DLR processing software used in this analysis produced slightly incorrect geolocation information [DLR, 1996]. However, the error introduced by this small effect should be similar for all three PMDs. Furthermore, this geolocation information was correct for the nadir static orbits. It is therefore concluded that the slightly incorrect geolocation information is not the cause for the observed systematic errors.

More likely, out-of-band straylight, which is not corrected for PMD 1 and PMD 2, causes the observed systematic deviations. The PMD out-of-band straylight measurements by TPD [TPD, 1994b; TPD, 1995] showed that the PMDs are sensitive to light beyond 790 nm. The correction for this out-of-band straylight is deduced from the GOME measurement of the solar spectrum and is based on the fact that the solar spectrum is known to be unpolarised. It is assumed that this correction is also appropriate when measuring an unpolarised Earth spectrum. The polarisation of a given PMD is then assumed to take the same (constant) value in the out-of-band straylight region [DLR, 1995]. This estimate is most appropriate for PMD 3, which has a wavelength range adjoining the straylight region beyond 790 nm. The correction for out-of-band straylight turns

out to be by far the largest for PMD 3, where this correction reduces the value of the fractional polarisation with  $\sim 17\%$  [Aberle, 1996]. Although slight correction factors are found for PMD 1 and PMD 2 [Slijkhuis, 1996], no out-of-band straylight correction is applied for PMD 1 and PMD 2.

It is concluded from this analysis that the out-of-band straylight correction for PMD 3 works quite well for cases where  $p = 0.5$ . The remaining systematic error in  $p$  is less than 1%. Application of the out-of-band straylight correction to PMD 1 and PMD 2 is expected to result in a decrease of their systematic errors, as suggested by this analysis.

##### Random errors

Differences observed between the random errors obtained for large and small (static) ground pixels are explained by two phenomena. The first reason is the variation of geometrical parameters across the ground pixels. Using an orbit propagator the variation in solar zenith angle, relative azimuth and view zenith angle was calculated along and across the GOME track. In Figures 6 and 7 the variations in  $\cos 2\chi_{s.s.}$  and  $p_7$  are shown for July 23, 1995 at 50°N. Each rectangle in these figures represents a 40 x 40 km pixel; the arrow denotes the GOME flight direction. From these figures it is clear that the variation in  $\cos 2\chi_{s.s.}$  and  $p_7$  across track is much larger than the variation along track. It can thus be concluded from these figures that the effect of variation in  $\cos 2\chi_{s.s.}$  is negligible for the observations made in nadir static mode, but could be important for the observations in scanning mode.

The second contribution to the random errors for larger ground pixels is due to the higher probability of observing an inhomogeneous scene. This introduces errors through the level 0→1 polarisation correction algorithm, which is based on the assumption of observing homogeneous scenes. Both effects are less severe in the case of observations in nadir static mode. This is clearly reflected in the results obtained in this study. The random errors for the large ground pixels are 1 to 2 orders of magnitude larger than those obtained for the small (static) ground pixels.

It was recognized that due to sequential readout of the array pixels the first and last array pixel of the spectral channels observe a somewhat shifted scene [Stammes *et al.*, 1996]. For the ground pixels of size 40 x 80 km<sup>2</sup> the scenes of the first and last array pixel are shifted by about 20 km across track. This could give rise to an error

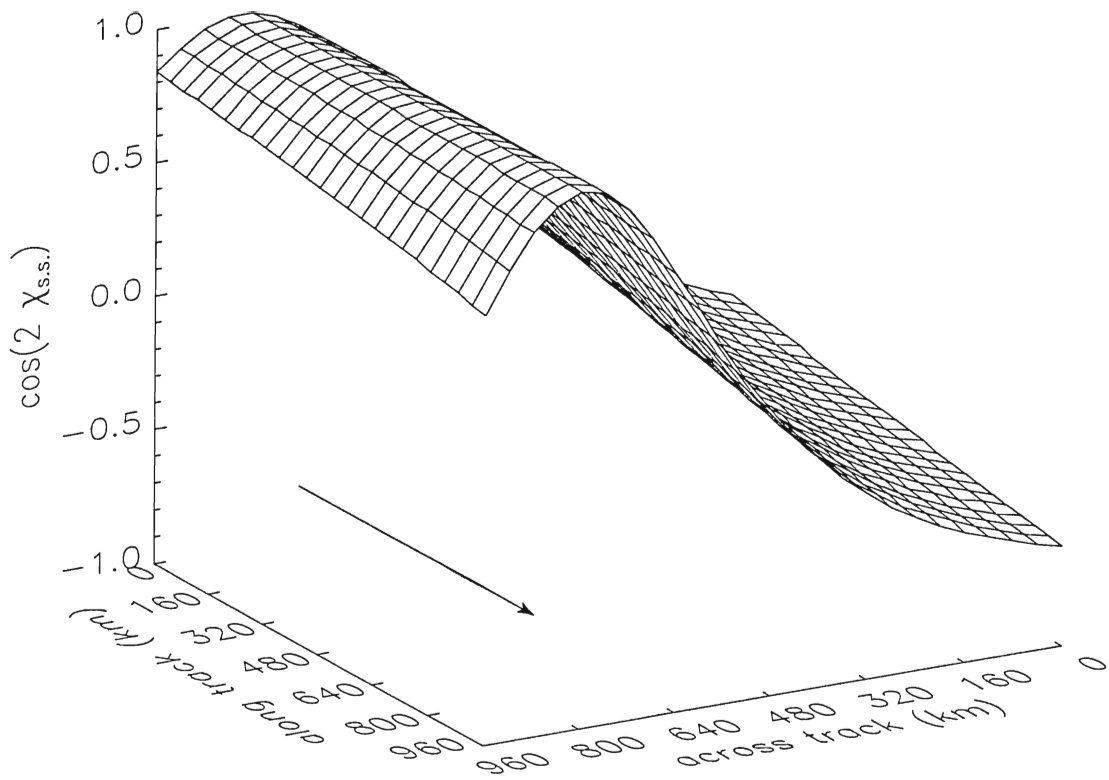


**Figure 6**  $\cos 2\chi_{s.s.}$  along and across the GOME track for July 23, 1995, at  $50^\circ\text{N}$ .

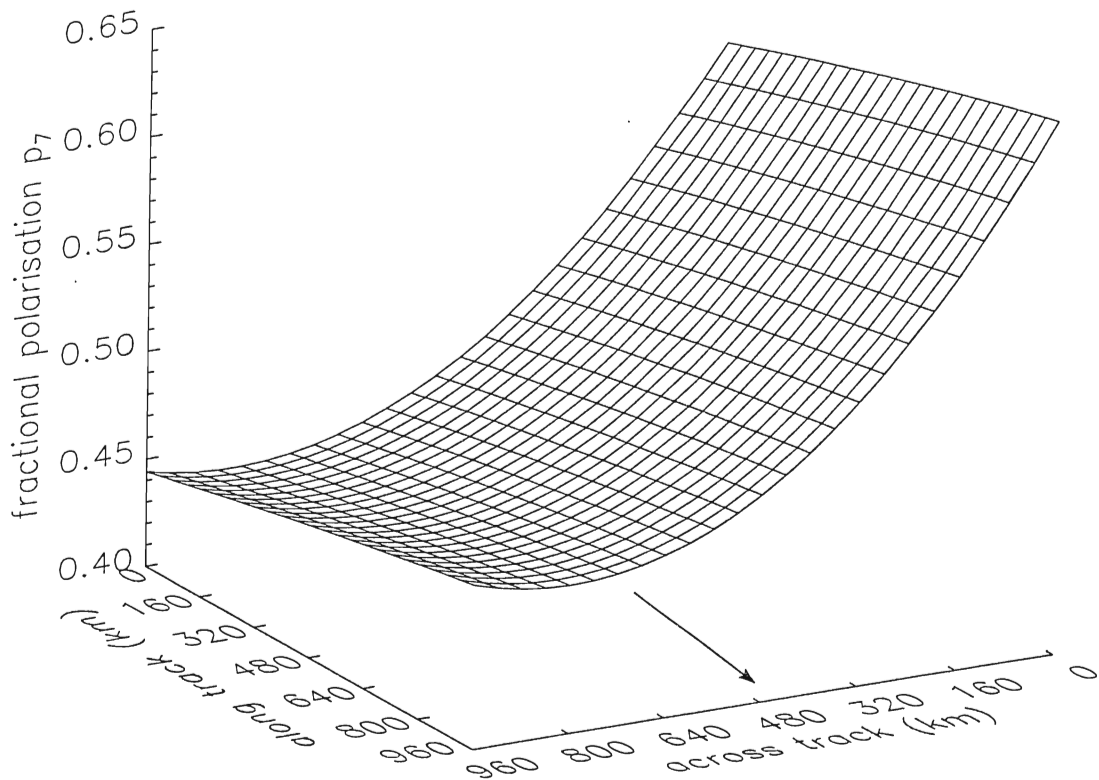


**Figure 7**  $p_7$  along and across the GOME track for July 23, 1995, at  $50^\circ\text{N}$ .

in the PMD polarisation measurements. However, for the data obtained in nadir static mode the two scenes are shifted by only 0.7 km along track, which will not influence the polarisation measurements.

In the case of the nadir static ground pixels, the random error obtained for PMD 3 is one order of magnitude larger than the random errors obtained for PMD 1 and PMD 2. One explanation for the spread in  $p$  is based on atmospheric scattering considerations. Scattering in the atmosphere by molecules, aerosols, and clouds and reflection by polarising surfaces, is capable of changing the direction of polarisation  $\chi$ . However, this change of  $\chi$  has a wavelength dependence which suggests the largest variations for PMD 1.

The observed large random error in the fractional polarisation for PMD 3 could more likely be related to the out-of-band straylight correction. This correction assumes that the out-of-band straylight correction for an unpolarised Earth spectrum is equal to the correction for the solar spectrum and independent of the actually observed spectrum. It is possible that for instance the presence of clouds or varying water absorption influences the amount of out-of-band straylight. As the out-of-band straylight correction is largest for PMD 3, the error introduced by this effect will be most pronounced for PMD 3.

## 5. CONCLUSIONS

The  $\cos 2\chi_{s.s.}=0$  analysis presented here has proved to be a useful diagnostic to assess the systematic and random errors in the fractional polarisation measured by GOME. Therefore, the effect of future processing software updates for GOME should be evaluated by means of this analysis. Preferably, it should be applied on data obtained with GOME operated in the nadir static mode to avoid complications introduced by the effect of measuring across (inhomogeneous) large ground pixels.

It is concluded that the PMD measurements of fractional polarisation  $p$  considered in this study are accurate to within a few percent. This is considered adequate for the purpose of the polarisation correction of the radiances.

It is concluded that the out-of-band straylight correction for PMD 3 works quite well for cases where  $p=0.5$ . Furthermore, improvements for PMD 1 and PMD 2 are anticipated after application of a correction for the out-of-band straylight.

## ACKNOWLEDGEMENTS

The work presented here was performed in the framework of GOME validation project NL-109. Discussions with Dr. S. Slijkhuis are gratefully acknowledged. The DLR-team is acknowledged for their assistance on software and level 0  $\rightarrow$  1 algorithm issues.

## REFERENCES

- Aberle, B., 1996, DLR, private communication.
- Coulson, K.L., 1988, "Polarisation and intensity of light in the atmosphere", A. Deepak Publ., Hampton (VA).
- DLR, 1995, Report ER-TN-DLR-GO-0022, "GOME level 0 $\rightarrow$ 1 algorithms description".
- DLR, 1996, 9<sup>th</sup> GOME Calibration and Characterisation Committee Meeting, 8 Jan. 1996, Oberpfaffenhofen, Germany.
- ESA, 1995, SP-1182 ESA, "GOME Users manual".
- McClatchey, R.A., R.W. Senn, J.E.A. Selby, S.E. Volz, J.S. Garing, 1972, "Optical properties of the atmosphere", 3<sup>rd</sup> edition Report AFCRL-72-0497, U.S. Air force Cambridge Research Labs.
- Slijkhuis, S., 1996, "GOME instrument properties affecting the calibration of radiance and polarisation", this issue. \*
- Stammes, P., 1994a, "The seventh point polarisation algorithm", Internal report, KNMI, De Bilt.
- Stammes, P., 1994b, "Errors in UV reflectivity and albedo calculations due to neglecting polarisation", SPIE Vol. 2311, Atmospheric Sensing and Modelling, pp. 227 - 235.
- Stammes, P., D.M. Stam, R.B.A. Koelemeijer, I.Aben, 1996, "Validation of GOME polarisation and radiance measurements", this issue. \*
- TPD, 1994a, Report TPD-ERS-GO-MIR-28, "Polarization properties of GOME FM".
- TPD, 1994b, Report TPD-ERS-GO-TN-96, "Out of band straylight in the GOME PMD channels".

---

\* Proceedings of the GOME Geophysical Validation Campaign, ESA WPP-108, ESA/ESTEC, Noordwijk (1996)

TPD, 1995, Report TPD-ERS-GO-MIR-29, "Straylight measurements of GOME FM".

Van de Hulst, H.C., 1957, "Light scattering by small particles", J. Wiley & Sons, New York.





## First validation of GOME cloud observations

R.B.A. Koelemeijer, P. Stammes, A.J. Feijt and A.C.A.P. van Lammeren

Royal Netherlands Meteorological Institute (KNMI)  
P.O. Box 201, 3730 AE De Bilt, The Netherlands

### Abstract

As a part of the ERS-2 GOME total ozone column retrieval algorithm, the Initial Cloud Fitting Algorithm (ICFA) [1] is used to account for the presence of clouds. Using ICFA, a cloud fraction is derived for each GOME pixel. This value has been compared with the cloud fraction derived from Meteosat data and ground-based lidar ceilometer measurements.

A good qualitative correlation between cloud fraction derived from ICFA, Meteosat and ground-based lidar measurements is found. However, the ICFA cloud fraction shows less variation than that derived from Meteosat and ground-based measurements. First results show that in case of *high* cloud fractions, ICFA *underestimates* the cloud fraction compared with Meteosat and ground-based measurements, especially for low clouds. In case of *low* cloud fractions over land surfaces, ICFA *overestimates* the cloud fraction. The underestimation for high cloud fraction is probably due to an underestimation of the cloud top pressure. The overestimation for low cloud fraction over land may be caused by an underestimation of the surface albedo.

It is shown that the PMD (Polarisation Measurement Device) measurements contain valuable information about cloud presence and structure. The use of the PMD cloud information could probably improve ICFA.

### 1. Introduction

The Global Ozone Monitoring Experiment (GOME), launched on board of the ERS-2 in April 1995, is a spectrometer measuring the terrestrial reflectivity in the UV and visible with a spectral resolution of

0.2–0.4 nm. The spatial resolution of the GOME measurements can be switched between  $40 \times 40 \text{ km}^2$  and  $40 \times 320 \text{ km}^2$ . The GOME measurements contain much information on e.g. trace gas and aerosol amounts. For accurate retrievals of trace gas and aerosol amounts from GOME measurements, the retrieval algorithms must account for the presence of clouds. Cloud detection is especially important if a large part of the atmospheric constituents of interest resides in the troposphere.

The emphasis of the GOME level 1 to 2 processing so far has been on the generation of the ozone vertical column amount. In the retrieval algorithm, the measured radiances are fitted using the Differential Optical Absorption Spectroscopy (DOAS) technique [1] to yield an ozone slant column. The vertical column is derived by dividing the slant column by the appropriate airmass factor (AMF). Since the airmass factor, which represents the effective atmospheric pathlength of photons, is influenced by the presence of clouds, cloud information is a necessary input for the AMF calculations. Another effect of clouds is their screening of tropospheric ozone, which would result in an underestimation of the total column if no correction were applied. To correct for these two effects of clouds, the Initial Cloud Fitting Algorithm (ICFA) has been incorporated into the ozone retrieval algorithm.

In this study, the cloud fractional coverage, or cloud fraction, derived using ICFA has been compared with that derived from Meteosat images and from ground-based lidar ceilometer measurements (Sect. 2). In Section 3, the potential of using the PMD (Polarisation Measurement Device) measurements for cloud detection has been investigated.

## 2. Validation of ICFA

### 2.1 Initial Cloud Fitting Algorithm

The diode-array detectors of GOME measure the solar irradiance and terrestrial reflected radiance with a high spectral resolution of 0.2–0.4 nm between 240 and 790 nm. From these measurements, the reflectivity, which is defined as  $\pi \times$  the reflected radiance divided by the incident solar irradiance at the top of the atmosphere, is obtained with a high degree of accuracy.

In order to derive the cloud fraction from GOME measurements, ICFA makes use of the reflectivity around the O<sub>2</sub> A absorption band, which is centered at about 761 nm. As an example, GOME measurements of nadir reflectivity around the O<sub>2</sub> A-band are shown in Fig. 1. The measurements have been performed at July 23 1995, over a cloudy scene above the Atlantic Ocean (latitude: 53.1° N, longitude: 34.1° W, solar zenith angle: 34°). The characteristic shape of the O<sub>2</sub> A-band is clearly visible. At wavelengths in the continuum, for which absorption is negligible, the reflectivity is high and nearly wavelength independent. Inside the O<sub>2</sub> A-band, the reflectivity

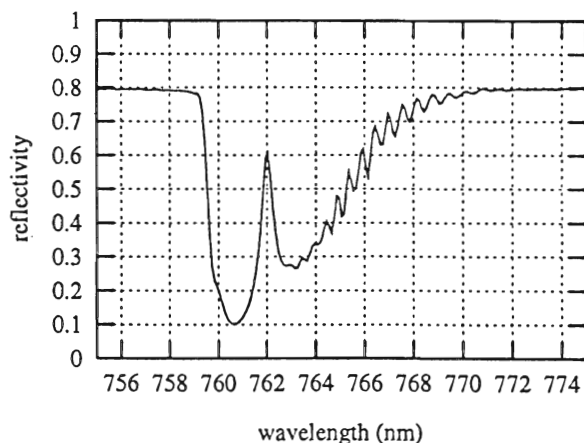


Figure 1: GOME reflectivity measurements between 755–775 nm, including the O<sub>2</sub> A absorption band. Data acquired at July 23 1995, over a cloudy scene above the Atlantic Ocean (latitude: 53.1° N, longitude: 34.1° W, solar zenith angle: 34°).

is much lower, especially in the centre of the band near 761 nm. The shape depends on the effective pathlength of light through the atmosphere, which depends mainly on cloud top pressure, cloud fraction, cloud optical thickness, surface pressure, solar zenith angle, viewing geometry and to a lesser extent on cloud bi-directional reflectivity and surface albedo [2], [3]. Since it is not possible to retrieve all these quantities simultaneously, various assumptions are made. In the first operational version of ICFA, clouds are regarded as bi-directional reflecting surfaces; enhanced absorption by multiple scattering inside clouds is neglected. Their reflectivity is assumed to be given by asymptotic relations for optically thick clouds, with a fixed optical thickness. Consequently, the cloud top reflectivity is prescribed. For the cloud top pressure, ground pressure and surface albedo, parameterisations and climatological databases are used. Based on these assumptions, radiative transfer calculations are performed for clear and completely cloudy situations. The cloud fraction is derived using least-squares fitting of the measured radiances with calculated radiances around the O<sub>2</sub> A-band.

### 2.2 Cloud fraction from Meteosat

Meteosat data over NW-Europe have been archived at KNMI since January 1993. Meteosat has a high temporal resolution (measurements each half hour) and a moderate spatial resolution ( $9 \times 5$  km<sup>2</sup> for the Netherlands and surroundings) which makes it suitable for validation of ICFA cloud fraction.

Cloud fraction is derived from Meteosat data in two steps. The first step involves cloud detection; each pixel is flagged cloud-free or cloudy. The cloud detection algorithm makes use of the temporal variability of clouds and uses weather forecast model analysis to improve thresholds [4]. The cloud fraction of the cloud-free pixels equals zero. The second step is to determine the cloud fraction of the cloudy pixels. In this study, a simple linear relationship between reflectivity and cloud fraction,  $C$ , is assumed:

$$C = \frac{R - R_s}{R_c - R_s}, \quad (1)$$

in which  $R$  is the measured reflectivity,  $R_s$  is the surface reflectivity and  $R_c$  is the cloud top reflectivity. The values for  $R_s$  and  $R_c$  have been chosen em-

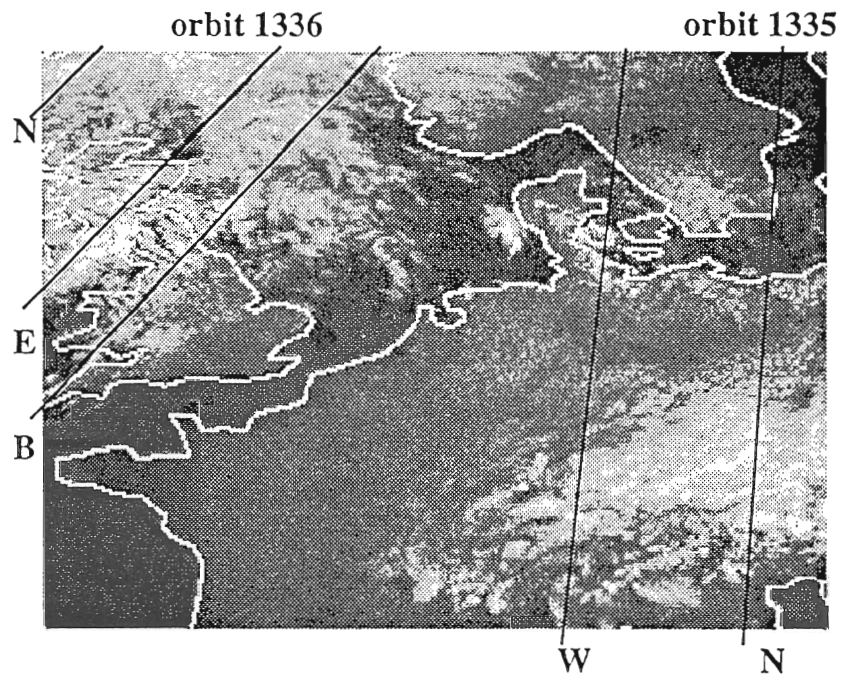


Figure 2: Meteosat visible image of NW-Europe at July 23 1995, 10:00 UT. The image is corrected for the variation of insolation. The black lines connect the centres of the different GOME pixels (East (E), Nadir(N), West(W) and Backscan(B)).

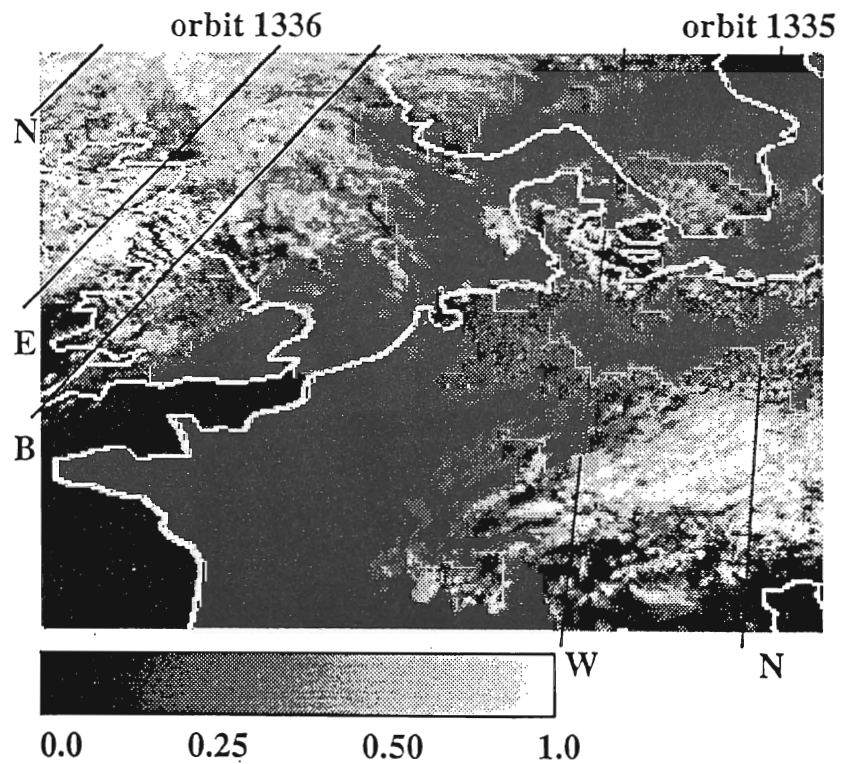


Figure 3: Grey scale plot of the cloud fraction derived from Meteosat data. Date: July 23 1995, 10:00 UT

pirically by selecting large cloud-free and completely cloudy areas. For land and sea surfaces different values for  $R_s$  have been taken. By assuming a linear relationship between reflectivity and cloud fraction, errors in cloud fraction arise in case of optically thin clouds. The cloud fraction can be interpreted as an effective cloud fraction for optically thick clouds. In this interpretation, the error in  $C$ , which is mainly due to the uncertainty in the cloud top reflectivity, is estimated to be  $\pm 0.07$ .

### 2.3 Comparison of ICFA with Meteosat

Two GOME overpasses of July 23 1995 over NW-Europe have been analysed: orbit 1335, time of overpass about 10:10 UT, and orbit 1336, time of overpass about 11:50 UT. The time difference between the GOME overpass and the acquisition of the Meteosat data was about 10 minutes for both overpasses.

The Meteosat visible image of 10:00 UT is shown in Fig. 2. Large cloud systems can be identified over the central part of Europe and over the North Sea and the UK. The image has been corrected for the variation of insolation. In Fig. 3, the derived cloud fraction is depicted in gray scale.

GOME has four pixel-types, 'East', 'Nadir', 'West' and 'Backscan', with approximate sizes during the first period of operation, which is considered here, of  $40 \times 80 \text{ km}^2$  for the East, Nadir and West pixels, and  $40 \times 240 \text{ km}^2$  for the Backscan pixels. The centres of the GOME pixels which fell inside the Meteosat image have been connected by black lines. The orbit-numbers and pixel-types have been indicated as well. In order to compare the Meteosat cloud fraction with the ICFA cloud fraction, the Meteosat cloud fraction has been averaged to the spatial resolution of the corresponding GOME pixel. Figure 4 shows both the ICFA cloud fraction and Meteosat cloud fraction for the West and Nadir pixels of orbit 1335. For comparison, the Meteosat cloud fraction is plotted at the left of the ICFA cloud fraction. Apparently, there is a good qualitative correlation between the ICFA cloud fraction and the Meteosat cloud fraction. However, the ICFA cloud fraction shows less variation than the Meteosat cloud fraction, especially over land surfaces. In Fig. 5, the ICFA cloud fraction of orbit 1335 is shown versus the Meteosat cloud fraction. It is clear that for *high* cloud fraction, ICFA *underestimates* the cloud fraction, up to 100 %. In case of *low* cloud fraction, ICFA *overestimates* the cloud fraction.

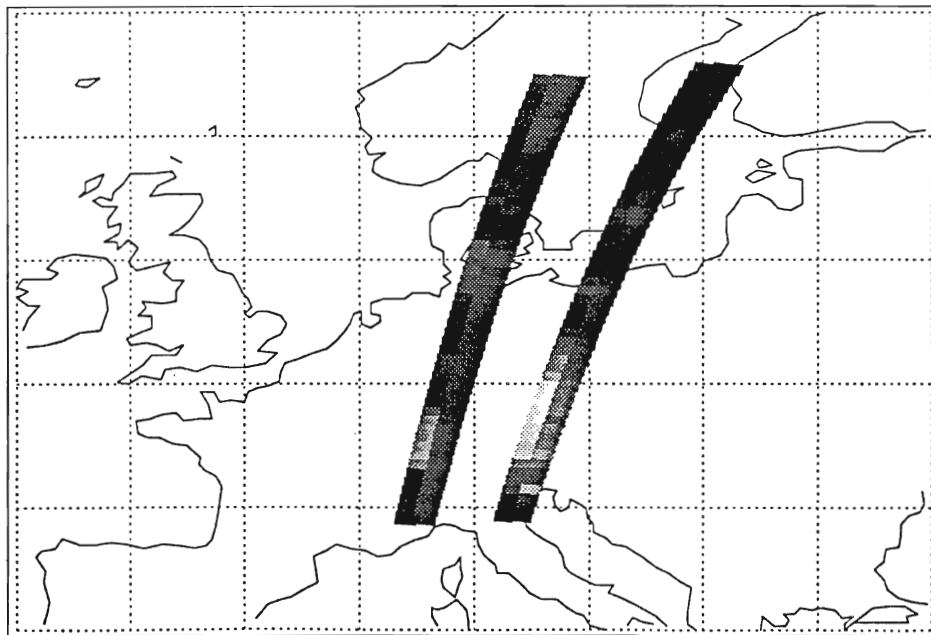


Figure 4: Cloud fraction from Meteosat (left) and ICFA (right) for the West and Nadir pixels of orbit 1335. The cloud fraction from Meteosat is averaged over a GOME pixel of  $40 \times 80 \text{ km}^2$ .

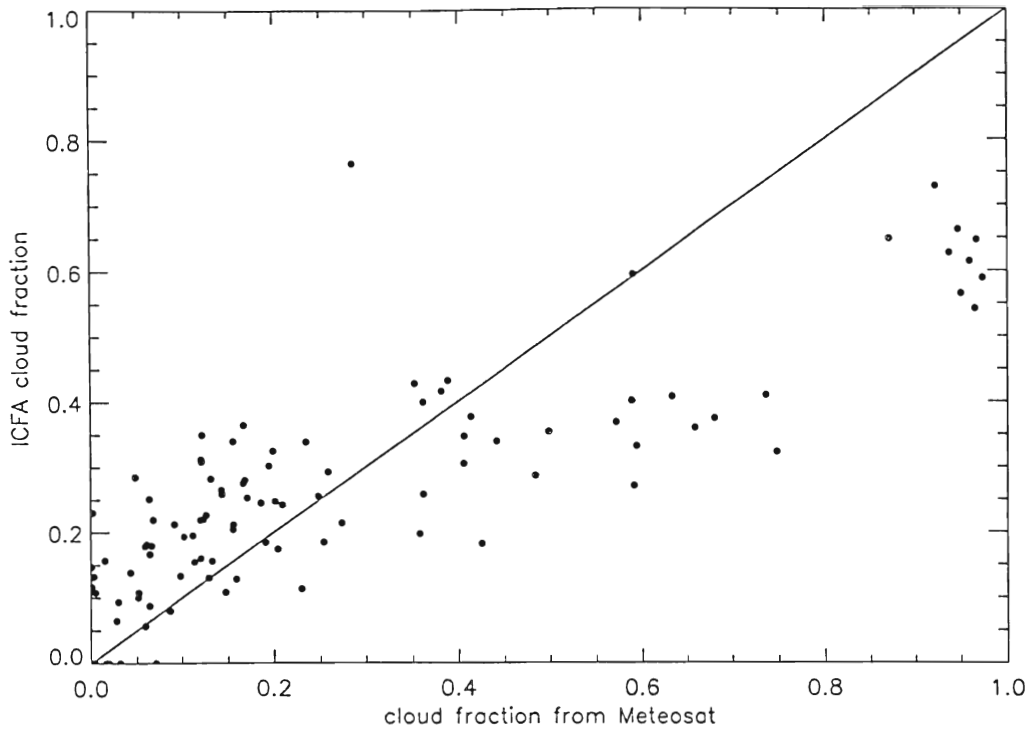


Figure 5: Correlation between ICFA cloud fraction and the cloud fraction derived from Meteosat data. Data acquired at July 23 1995, orbit 1335, 10:09 - 10:14 UT.

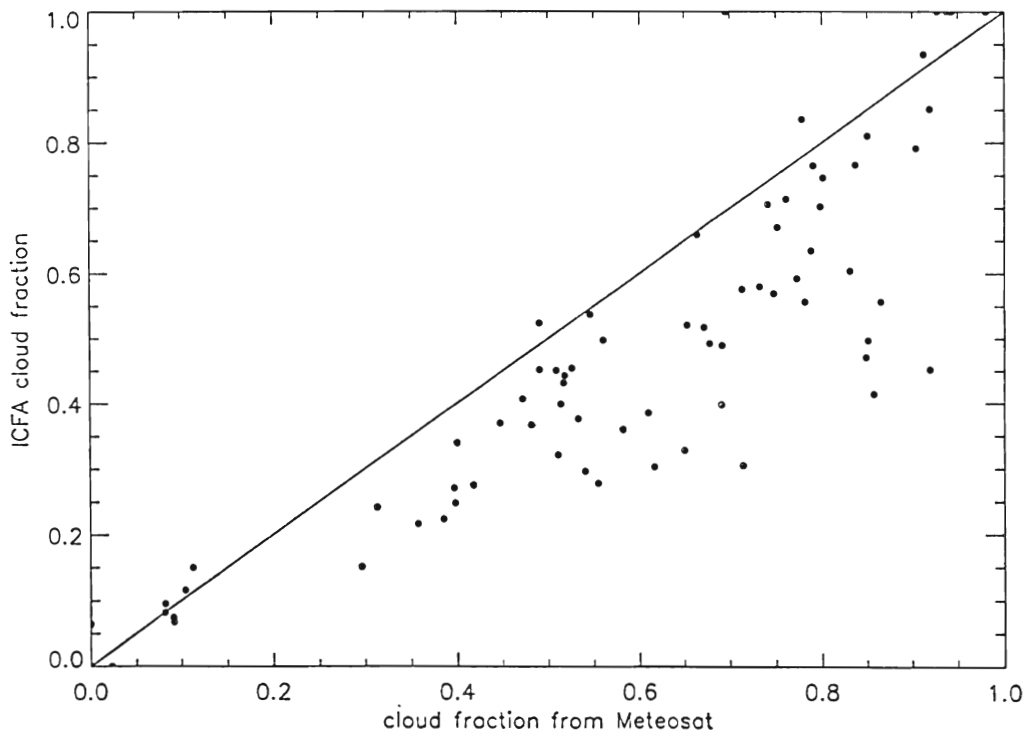


Figure 6: Same as 5, but for orbit 1336, 11:49 - 11:53 UT.



For orbit 1336, shown in Fig. 6, a better correlation between ICFA and Meteosat cloud fraction is found. The overestimation for low cloud fraction is not found in this case.

The underestimation for high cloud fraction is probably due to an underestimation of the cloud top pressure. In ICFA, the assumed cloud top pressure is about 500 hPa for the mid-latitudes, which is very low for most cases. An underestimation of cloud top pressure (= overestimation of cloud top height) leads to an underestimation of the cloud fraction. This is caused by the fact that the amount of oxygen screened by the clouds is the same for high clouds with low cloud fraction as for low clouds with high cloud fraction, and hence give the same depth of the oxygen A-band. The actual cloud top height, as estimated from the Meteosat IR images, appeared to be higher in orbit 1336 (cloud system over the North Sea and the UK) than in orbit 1335 (cloud system over the central part of Europe). If the actual cloud top height is closer to the assumed value, the error in the cloud fraction is smaller. The overestimation for low cloud fraction is especially found over land surfaces. This overestimation might be due to an underestimation of the surface albedo over land.

#### 2.4 Comparison of ICFA with lidar measurements

At the meteorological site of Cabauw, located in the central part of the Netherlands (51.97° N, 4.93° E), lidar ceilometer measurements are performed on a routine basis. The lidar ceilometer is limited to a height of 4 km. From those measurements, cloud base height and cloud fraction have been derived. The spatial resolution of the lidar measurements due to cloud motion is much higher than that of the GOME measurements. In order to match the horizontal scale of GOME, the lidar measurements have been averaged over one hour around the GOME overpass.

In Table 1, the cloud fraction derived from the Cabauw measurements and ICFA is shown. The approximate distance between the Cabauw site and the centre of the nearest GOME pixel is given in the fourth column. In the fifth column, the cloud base height of the lowest cloud layer as measured by the ceilometer is given. In Fig. 7, the ICFA cloud fraction

is plotted against the cloud fraction derived from the Cabauw measurements. Although caution should be used regarding the small number of overpasses considered here, the ground-based measurements seem to confirm that ICFA underestimates the cloud fraction for high cloud fractions. The overestimation for small cloud fractions can not be confirmed, because of the height limitation of the lidar: if the lidar does not detect any clouds, clouds may be absent, or present above 4 km height.

Table 1: Cloud fraction (CF) derived from the lidar measurements at the meteorological site of Cabauw and the ICFA cloud fraction. Fourth column: approximate distance between the Cabauw site and the centre of the nearest GOME pixel. Fifth column: cloud base height (CBH) of lowest cloud layer.

Day	CF Cabauw	CF ICFA	distance [km]	CBH [km]
Jul 22 1995	0.64	0.28	>100	1.0–1.6
Jul 25 1995	0.00	0.14	10	–
Aug 29 1995	0.75	0.47	10	0.8–2.5
Sep 17 1995	0.38	0.18	70	0.6–0.8
Oct 3 1995	1.00	0.45	10	0.4–0.5

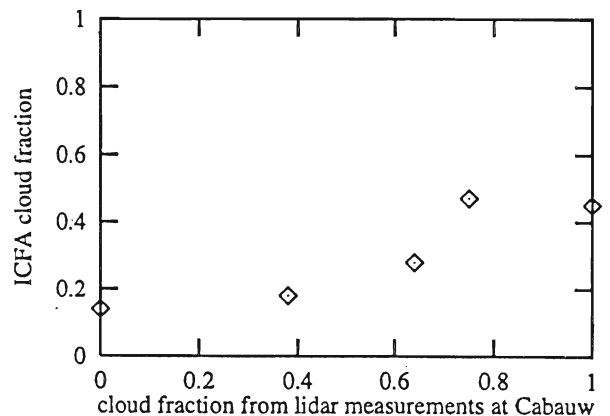


Figure 7: Correlation between ICFA cloud fraction and the cloud fraction derived from the ground-based lidar measurements at the meteorological site of Cabauw. The data are tabulated in Table 1.

### 3. Imaging of clouds with PMDs

To correct the GOME spectral reflectivity measurements for the polarisation sensitivity of the array detectors, Polarisation Measurement Devices (PMDs) have been added to the GOME instrument. The PMDs measure the solar irradiance and the terrestrial reflected radiance in three broad spectral bands, with effective wavelengths of 350, 490 and 700 nm for respectively PMDs 1, 2 and 3. The spatial resolution of the PMDs is  $20 \times 40 \text{ km}^2$  for a GOME swath width of 960 km, amounting to 48 PMD-pixels over the full swath. Evidently, the spatial resolution of the PMDs is much better than that of the array detectors. The polarisation sensitivity of the PMDs differs from that of the array detectors. By combining the PMD measurements and the measurements of the array detectors, the polarisation is obtained at three wavelengths for each GOME array detector groundpixel.

The PMD signal values which are supplied in the GOME extracted level 1 product, denoted by  $R_{PMD}$ , represent the ratio between the reflected radiance,  $I_{PMD}$ , and the direct solar irradiance perpendicular to the direction of propagation ( $\pi F_{\odot}$ ). In formula:

$$R_{PMD} = \frac{I_{PMD}}{\pi F_{\odot}}. \quad (2)$$

If polarisation correction is applied,  $I_{PMD}$  is corrected using the average polarisation of the array detector groundpixel.

Because of the better spatial resolution, the PMDs are useful for cloud detection and imaging. To illustrate this, PMD measurements of July 23 1995, orbits 1334 – 1338, over Europe, Africa and the Atlantic Ocean are shown in Fig. 8. The image is a colour composition of PMD 1, 2 and 3 measurements. The PMDs of the backscan pixels have not been used. In Fig. 9 a detail of this image is depicted, showing good correlation with the Meteosat visible image (Fig. 2). Obviously, the PMDs contain much information about cloud presence, cloud structures and surface type. The cloud information in the PMDs is presently not used in ICFA. ICFA could probably be improved by first using the PMD mea-

surements for the estimation of cloud fraction and then using the radiances around the O<sub>2</sub> A-band for the retrieval of cloud top height. This method would not suffer from large errors due to climatological estimates of cloud fraction or cloud top height.

### 4. Discussion and conclusions

The ICFA cloud fraction has been compared with the cloud fraction derived from Meteosat images and ground-based lidar measurements. A good qualitative correlation between the cloud fraction derived from ICFA, Meteosat and the lidar measurements has been found. However, ICFA shows less variation in cloud fraction than Meteosat and ground-based measurements. First results show that for *high* cloud fractions, ICFA *underestimates* the cloud fraction compared with Meteosat and ground-based measurements, especially for low clouds. The underestimation of the cloud fraction is probably caused by the overestimation of the cloud top height. In case of *low* cloud fractions over land, ICFA *overestimates* the cloud fraction, which might be due to an underestimation of the surface albedo.

The error in the ICFA cloud fraction leads to errors in the ozone vertical column in two ways. In the first place, the error in the ICFA cloud fraction leads to errors in the air mass factor (AMF). In the operational ozone vertical column retrieval algorithm, the AMF of a partly cloudy scene is computed by computing the AMF for a cloud-free and a completely cloudy situation. Linear combination with the cloud fraction as weighting function yields the AMF of the partly cloudy scene. To estimate the error in the AMF introduced by a 100% underestimation of the cloud fraction, test calculations have been performed with the Doubling-Adding KNMI (DAK) radiative transfer model [5]. From these calculations, it is concluded that the AMF is underestimated by 2–3% for a 100% underestimation of the cloud fraction. Consequently, the total ozone vertical column is overestimated by 2–3%. In the second place, the error in the ICFA cloud fraction leads to errors in the estimated amount of ozone screened by clouds (the so-called ghost vertical column). However, the error in the

ghost vertical column due to the underestimation of the cloud fraction may be largely compensated by the overestimation of the cloud top height.

It has been shown that the PMD measurements contain valuable information about cloud presence and cloud structure. This information is presently not used in ICFA. In ICFA, it is problematic to discriminate between cases of high clouds with small cloud fraction and cases of low clouds with high cloud fraction. In the current algorithm, the cloud fraction is derived assuming that the cloud top height is known in advance. ICFA could probably be improved by first using the PMD measurements for the estimation of cloud fraction and then using the radiances in the O<sub>2</sub> A-band for the retrieval of cloud top height.

## Acknowledgements

This study was performed within the framework of the GOME validation project NL-114 of which Hans van der Woerd (National Institute of Public Health and Environmental Protection (RIVM)) was the coordinator. The GOME data were kindly provided by the European Space Agency (ESA), and processed by the Deutsche Forschungsanstalt für Luft- und Raumfahrt (DLR). The Space Research Organisation of the Netherlands (SRON) is acknowledged for the financial support of part of this work.

## References

- [1] Spurr, R. 1994: "GOME level 1 to 2 algorithms description", Technical Note ER-TN-DLR-GO-0025, Iss./Rev. 1/A, DLR, Oberpfaffenhofen.
- [2] Fischer, J. and Grassl, H. 1991: "Detection of cloud top height from backscattered radiances within the oxygen A band. Part 1: theoretical study", *J. Appl. Met.*, Vol. 30, pp. 1245–1259
- [3] Kuze, A. and Chance, K.V. 1994: "Analysis of cloud top height and cloud coverage from satellites using the O<sub>2</sub> A and B bands", *J. Geophys. Res.*, Vol. 99, No. D7, pp. 14481–14491
- [4] Feijt, A.J. and van Lammeren, A.C.A.P. 1996: "Ground based and satellite observations of cloud fields in the Netherlands", *Mon. Wea. Rev.* (accepted)
- [5] Stammes, P. 1994: "Errors in UV reflectivity and albedo calculations due to neglecting polarisation", in: *Proceedings of the European Symposium on Satellite Remote Sensing*, 26–30 September, 1994, Rome. EOS/SPIE volume 2311, 227–235

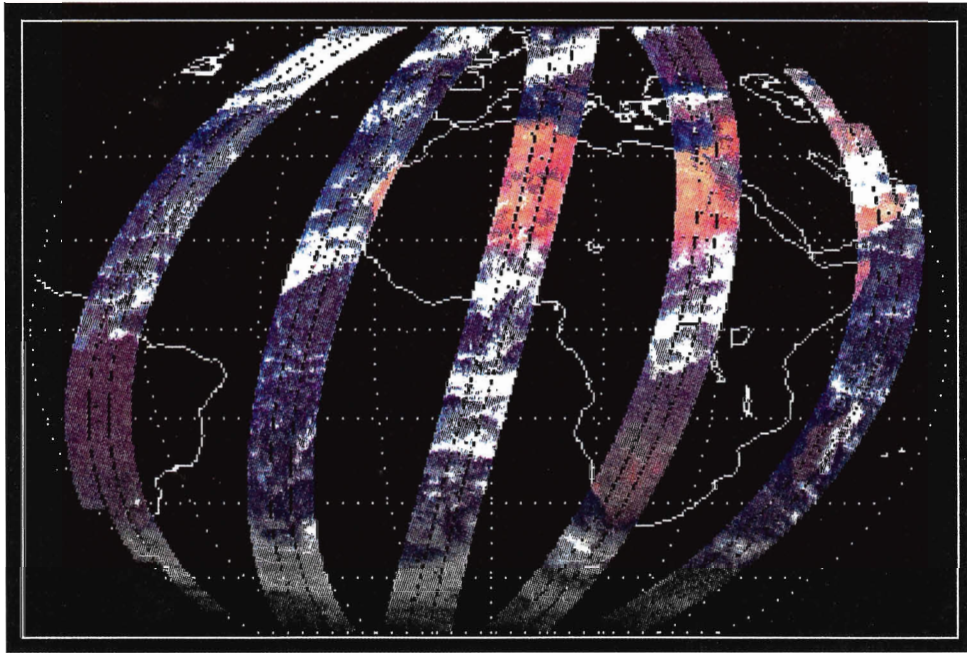


Figure 8: Colour composite of PMD 1, 2 and 3 measurements of July 23 1995, orbits 1334 – 1338. The PMD measurements provide valuable information on cloud presence, cloud structure and scene type.

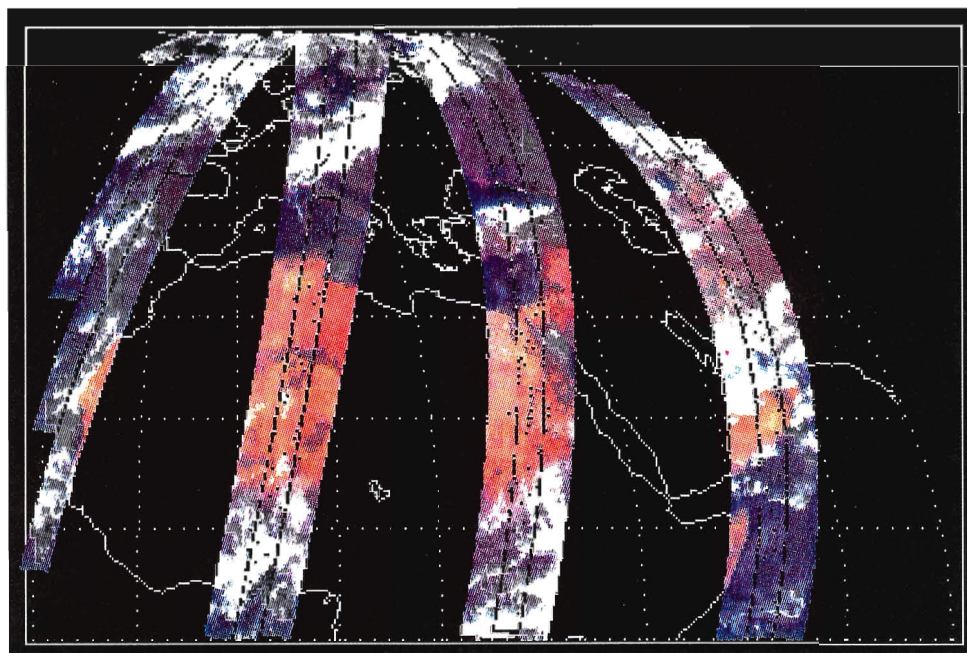


Figure 9: Detail of fig. 8. A good correlation is found with the Meteosat visible image of Fig. 2.



# Studies on DOAS Ozone Column Retrieval from the UV and Visible Measurements of GOME

M. Eisinger, A. Richter, J. P. Burrows

Institute of Environmental Physics, University of Bremen, Germany

A. Piters

Royal Dutch Meteorological Institute, De Bilt, The Netherlands

## Abstract

Various aspects of ozone column retrieval from GOME channel 2 and 3 spectra by the Differential Optical Absorption Spectroscopy (DOAS) method have been investigated. DOAS evaluation has been performed on GOME level 1 data. In the UV some sensitivity tests have been undertaken and improvements for the GOME Data Processor (GDP) are suggested. In the visible region the suitability of four different wavelength windows for ozone column retrieval has been investigated. Ozone columns retrieved by the GDP both in the UV and the visible have been compared. The results indicate a good potential for the visible but still columns on average 30% higher than from the UV. The largest deviations occur at small ICFA cloud fractions. Finally, it is recommended to modify the calculation of air-mass factors in the GDP. For the future a combination of UV (for low solar zenith angles) and visible (for high solar zenith angles) ozone is proposed.

## 1 Introduction

The remote sensing of atmospheric gases from ground-based, balloon-borne, aircraft or satellite platforms utilizes the characteristic absorption or emission features of a particular gas. Remote sensing of ozone has been shown to be possible from the UV to the microwave spectral regions. Each part of the electromagnetic spectrum, coupled with a particular viewing geometry has specific advantages and disadvantages for the retrieval of ozone for different parts of the atmosphere (*Ozone Measuring Instruments...*, 1989).

The GOME (Global Ozone Monitoring Experiment) is a new instrument launched aboard ERS-2 in April 1995. GOME observes the spectral region from 240 to 790 nm (*Burrows et al.*, 1988; *GOME Interim Science Report*, 1993).

In the wavelength range covered by the GOME instrument both the Hartley-Huggins bands in the near UV and the Chappuis bands in the visible can be utilized to determine atmospheric ozone columns. Traditionally, ozone has been retrieved from the UV spectral information by the SBUV/TOMS

satellite instruments and by ground-based Dobson, Brewer, and several filter instruments. Alternatively in ground-based zenith-sky measurements ozone columns are usually calculated from the visible absorption bands.

Currently the ozone columns in the GDP *main* product are derived from the UV (GOME channel 2) via the DOAS method. A major advantage of the UV is the high signal-to-noise ratio for the absorbances because differential absorptions are more than ten times larger in the Huggins bands than in the Chappuis bands. However, the retrieval of ozone from the UV has several disadvantages as well. The most important are the temperature dependence of differential absorption cross sections and the wavelength dependence of air-mass factors (AMFs) by which the slant column densities from the DOAS fits have to be divided in order to get vertical column densities.

The objective of this study was to investigate a number of aspects of relevance to the DOAS ozone retrieval in both the UV and visible spectral regions. This is of great importance for the GOME data interpretation and usage. In the following sections several aspects of DOAS ozone retrieval in both the UV and the visible bands are discussed. Section 2 describes tests performed using level 1 data (radiance/irradiance). Section 3 compares ozone vertical columns retrieved from the UV and visible as given by the GOME Data Processor (GDP) in the level 2 product.

## 2 DOAS studies using GOME level 1 data

Measurements of atmospheric trace gas columns employing the difference in absorption at different wavelengths date back to the time of *Dobson* (1926), who used wavelength pairs to derive ozone columns. *Noxon* (1975) derived NO<sub>2</sub> columns from the depth of absorption bands in continuous spectra. The differential absorption technique became a standard method for zenith sky measurements (e.g. *Noxon et al.*, 1979, *Solomon et al.*, 1987). The term DOAS (Differential Optical Absorption Spec-



troscopy) was first applied to long-path measurements of tropospheric trace gases (e.g. *Perner and Platt, 1979*). DOAS was chosen as the method for operational retrieval of trace gas columns from GOME measurements. It is the first time this method has been applied to measurements from space-borne instruments.

DOAS evaluation was performed on GOME level 1 data as extracted by the DLR program `gdp01.exe` (version 1.71) with all options<sup>1</sup> set “on” except unit conversion. The DOAS fit runs presented in this study were performed with the program which is used for analysing the ground-based zenith-sky measurements of the Bremen group (e.g. *Richter et al., 1995*). (From this program the operational DOAS routine in the GDP was developed.) Given the solar irradiance  $I_0(\lambda)$  and the earth radiance  $I(\lambda)$  measured by GOME, and the differential absorption cross sections  $\sigma'_i(\lambda)$  of the relevant species, their slant column densities  $L_i$  are fitted together with polynomial coefficients  $c_j$  according to the Lambert-Beer law

$$\ln I(\lambda) = \text{SOL} \ln I_0(\lambda) - \sum_i L_i \sigma'_i(\lambda) + \sum_j c_j \lambda^j.$$

For a discussion of the additional fit parameter “SOL” see below. “SOL” is set to 1 unless otherwise stated.

## 2.1 Reference spectra

Absorption cross sections of ozone and NO<sub>2</sub> have been measured as a function of temperature with the GOME flight model (FM) (*Dehn, 1995*; Final Report to ESA in preparation). In this study O<sub>3</sub> cross sections measured at  $T = 221$  K and NO<sub>2</sub> cross sections measured at  $T = 241$  K have served as references.

The empirical spectrum used to account for the Ring effect, the partial filling-in of Fraunhofer lines in earthshine radiances by inelastic (mainly Raman) scattering, was also measured with the GOME FM (*Burrows et al., 1995*).

It is recommended to use the ozone, NO<sub>2</sub>, and Ring spectra measured with the GOME FM for operational processing. This was already substantiated in detail during the Validation Campaign. Tests on GOME level 1 data showed that the fit using the GOME FM O<sub>3</sub> and NO<sub>2</sub> data was superior (i.e. resulted in less residual error) to any literature spectra available (*Bass and Paur, 1985*; *Schneider et al., 1987*; *Harwood and Jones, 1994*). The main advantage of using the GOME FM reference spectra for DOAS analysis of GOME FM in-orbit data arises from their having appropriate spectral resolution so

<sup>1</sup>These options are controlling the calibration steps to be applied on the raw (level 0) data: Leakage / fixed pattern noise / straylight correction, normalisation (Binary Units (BU) → BU/s), polarisation correction, radiometric calibration (BU/s → mW/m<sup>2</sup>.nm.sr), unit conversion (mW/m<sup>2</sup>.nm.sr → photons/s.m<sup>2</sup>.nm.sr).

that convolution with the instrumental slit function is not necessary.

For O<sub>4</sub> the measurements by *Greenblatt et al. (1990)* with some corrections to the wavelength axis proposed by *Burkholder* were used. The spectrum of H<sub>2</sub>O was calculated (*Chance, 1994*) from the HITRAN database and convoluted with the GOME slit function.

Since GOME spectra are given in vacuum wavelengths all trace gas references were converted to vacuum wavelengths according to the *Edlén (1953)* formula.

## 2.2 Ultraviolet window tests

The UV fitting window used in the present GDP, 325–335 nm, was chosen for the tests described below. They were performed on a set of 57 ground pixels from orbits 1351 and 1352 (24th July 1995) covering the complete solar zenith angle range from 19° to 93°. O<sub>3</sub> was the only trace gas fitted (with the exception of the tests described in the next paragraph).

### NO<sub>2</sub>

Fit runs were performed with and without NO<sub>2</sub> as species in addition to ozone. For most ground pixels negative, i.e. unphysical, NO<sub>2</sub> slant columns with large fit errors were found. This is explained by the small absorbance of NO<sub>2</sub> compared to O<sub>3</sub> in the UV window. NO<sub>2</sub> normally cannot be found because uncertainties in the ozone cross sections and the wavelength dependence of the AMFs (which are neglected) are of the same order of magnitude as the NO<sub>2</sub> differential spectrum in this region.

Including NO<sub>2</sub> in the fitted species, however, leads to a reduction of the retrieved ozone slant columns of up to 4% for solar zenith angles above 80°. (For smaller zenith angles the effect on ozone is quite small.) It is therefore recommended to use only ozone as trace gas reference for the UV fits.

A quality control test is however also recommended. This involves the determination of the NO<sub>2</sub> slant column in the window 425–450 nm and subsequently estimation of the UV NO<sub>2</sub> differential absorption. Provided the latter is less than 1% of the O<sub>3</sub> absorption then NO<sub>2</sub> can be neglected in the UV window.

### Solar irradiance in linear fit

Comparison of fits where the factor “SOL” is a free parameter and fits with “SOL” fixed to 1 were made. The only trace gas considered was ozone. Note that “SOL” is an exponent for the solar irradiance  $I_0$  and that there is no physical reason for it to have a value other than 1. If “SOL” is included as a fit parameter its value ranges between 0.86 and 0.96 and ozone fit errors are drastically reduced. The reason is that a “SOL” factor less than 1 at least in

part accounts for the Ring effect, because “Ring( $\lambda$ )” correlates strongly to  $(I_0(\lambda))^{-1}$ . However, including the solar irradiance in the linear fit can have quite a strong impact on the ozone slant columns. Ozone slant columns where “SOL” was fitted were up to 12% higher than with “SOL” = 1. The proper way to take account of the Ring effect is fitting an empirical (i.e. measured) or theoretical “Ring spectrum” in addition to ozone and to fix “SOL” to 1, i.e. to exclude the solar irradiance from the linear fit. This strategy is strongly recommended, both for the UV and the visible region.

### Temperature dependence

The differential absorption cross sections in the Huggins bands decrease with increasing temperature (Figure 1). For the “classical” DOAS fitting an ozone spectrum at a certain temperature has to be chosen, thereby neglecting the real temperature profile of the atmospheric ozone. In the GDP the temperature at the ozone concentration maximum from climatology is selected. To estimate the error introduced by deviations of the actual temperature from climatology, fits were performed with ozone reference spectra measured by the GOME flight model at  $T = 202$  K,  $T = 221$  K, and  $T = 241$  K.

It was found that raising the temperature of the ozone reference by 20 K increased the ozone slant column density calculated by the DOAS fit (and thereby the vertical column) by 6%. This implies a temperature effect of 0.3%/K or, put into a simple rule of thumb, assuming an ozone vertical column of 330 DU: 1 K temperature deviation means 1 DU ozone deviation<sup>2</sup>. In this simple estimation the atmospheric temperature profile has been neglected.

In conclusion it is vital in GOME ozone validation to regularly check the deviations of the actual temperature profile from the climatology used in the GDP because these deviations might lead to systematic errors of a few percent in the retrieved ozone column. For example, in winter 1995/96 stratospheric temperatures over the Arctic have been unusually low for several weeks (*von der Gathen*, 1996). The GDP, assuming climatological values, is expected to somewhat overestimate ozone columns in this situation.

### Air-mass factors

Air-mass factors for scattered light observations depend on a large number of parameters, e.g. the measurement geometry (solar zenith angle, line-of-sight zenith angle, relative azimuth), wavelength, air and ozone density profiles, aerosol loading and the density profile of the molecule considered. For the ozone Huggins bands the situation is special because of their large absorption. The atmosphere cannot be considered optically thin at these wavelengths.

<sup>2</sup>Note that this number depends on the fitting window. It is given for the 325–335 nm window.

At ozone absorption minima the light penetrates deeper into the atmosphere, leading to a lowering of the most probable scattering height compared to absorption maxima. Thus UV AMFs are significantly dependent on wavelength (much more than VIS AMFs). An example is shown in Figure 2.

The AMF follows the shape of the ozone absorption bands, being lowest in the absorption maxima. It varies between 4.69 and 4.87 or by 3.8% over the fitting window in this example<sup>3</sup>. In the present GDP the “classical” DOAS approach is implemented. The AMF is calculated for the window center wavelength, i.e. 330 nm, where the AMF is near its upper limit. Thereby systematic errors are introduced which possibly lead to ozone columns which are too low. Since the wavelength dependence of the AMF is larger for larger slant columns, these errors are expected to increase with increasing solar zenith angles.

Furthermore, the AMFs in the UV are more sensitive to the ozone total column, the ozone vertical profile, and the stratospheric aerosol loading, than the AMFs in the visible. In addition, the temperature profile influences absorption and thereby also the AMF. More detailed AMF sensitivity studies for “real” GOME situations are clearly needed, but it is safe to say that, considering the atmospheric variability, there are large uncertainties in the UV AMFs due to (at present necessary) simplifications in level 1 to 2 processing, and that these uncertainties are largest for large solar zenith angles. AMFs will be a key issue both in understanding GOME deviations from ground-based measurements and in future improvements of the algorithm. It is recommended that in the long run “classical” DOAS where ozone absorption cross sections (at a certain temperature) are fitted, is replaced in the UV by “modified” DOAS where the wavelength dependence of the AMF is taken into account by fitting optical densities calculated by a radiative transfer model.

### 2.3 Visible windows tests

In the visible wavelength range several wavelength windows within GOME channel 3 were tested in order to derive an optimum for ozone retrieval. These tests were performed on orbits 1322 (22nd July 1995, the first GOME orbit available) and 2123 (16th September 1995).

Based on *Diebel et al.* (1995) the following criteria have to be applied for window optimisation:

1. strong differential ozone absorption structures;

<sup>3</sup>The AMF can be evaluated at any wavelength within the fitting window since the center wavelength is not *a priori* suited better than other wavelengths. [For the 325–335 nm window the center wavelength is probably even a bad choice. Note that at 330 nm the temperature dependence of the absorption cross section (and thereby of the AMF) is relatively large.] Choosing another AMF wavelength can result in vertical columns shifted by a few percent. However, it is recommended to refer to physical reasons for choosing the AMF wavelength(s) rather than to fine-tune vertical columns by adjusting the AMF wavelength.

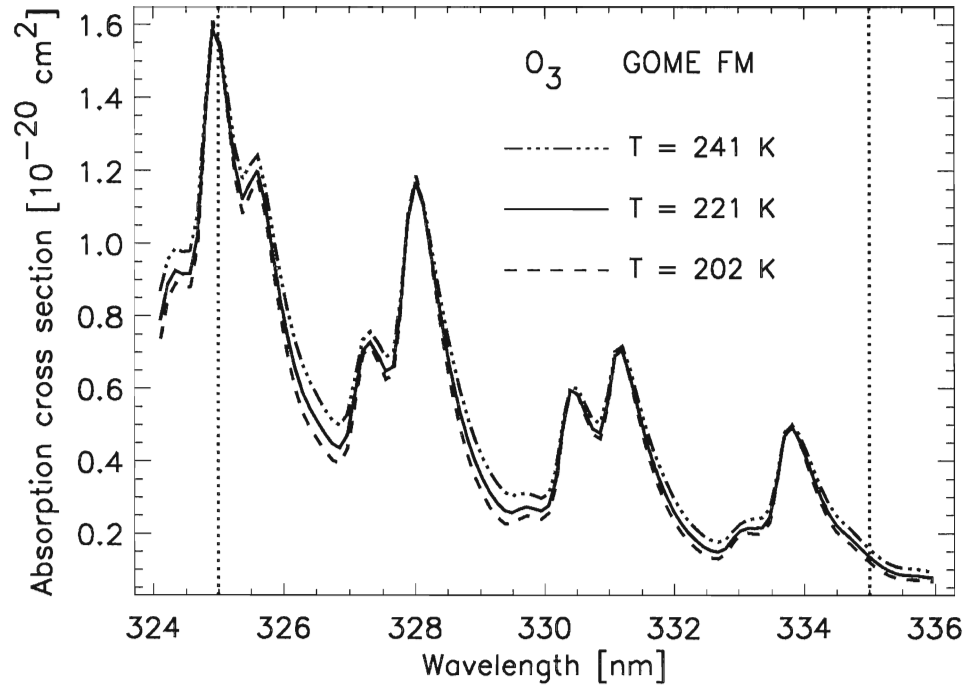


**Figure 1:** Absorption cross sections of the ozone Huggins bands as measured with the GOME flight model at  $T = 202$  K,  $T = 221$  K, and  $T = 241$  K. The vertical dotted lines denote the present UV fitting window in the GOME Data Processor.

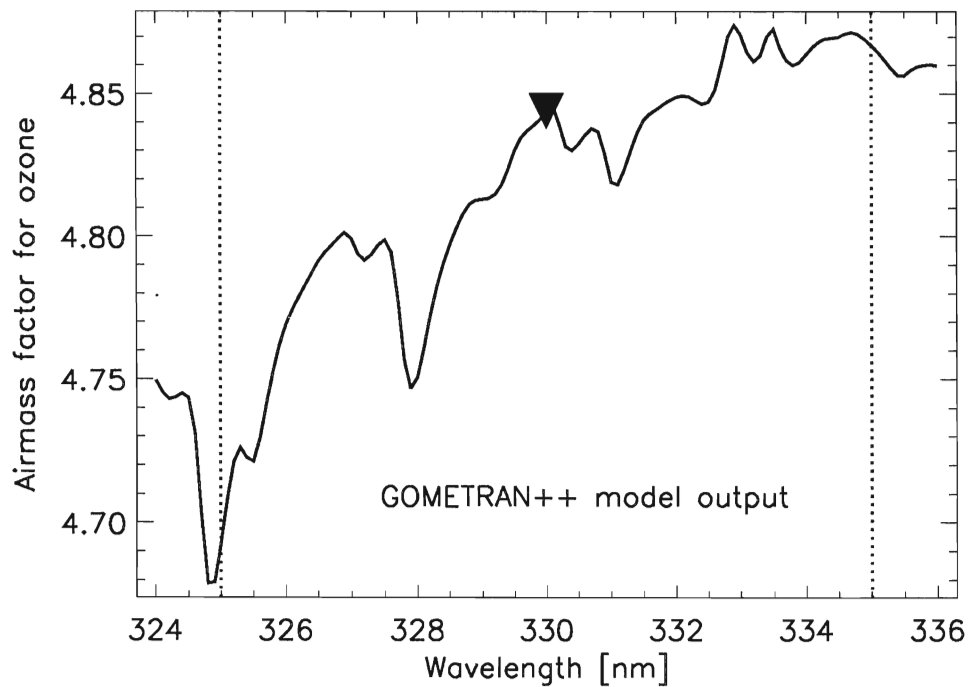


**Figure 2:** Air-mass factor for ozone as calculated by the radiative transfer model GOMETRAN++. Scenario: solar zenith angle  $77^\circ$ , line-of-sight zenith angle  $0.5^\circ$ , relative azimuth  $119^\circ$ , January, latitude band  $50\text{--}60^\circ\text{N}$ , ozone vertical column 348 DU. Trace gas reference spectra as described in section 2.1. The triangle indicates the air-mass factor at window center which is used in the GOME Data Processor for conversion to vertical columns.

2. minimal interference by O<sub>4</sub>, H<sub>2</sub>O, and by strong Fraunhofer lines;
3. window size between 100 and 300 pixels (20–60 nm in the visible);
4. moderate variations of the air mass factor across the window;
5. high signal-to-noise ratio;
6. no crossing of GOME channel boundaries;
7. minimal interference by instrumental features such as etaloning and polarisation sensitivity effects.

The last item has been added to the *Diebel et al.* list after the experience with the GOME data (see below). Differential absorptions of the relevant species are shown in Figure 3. Ozone differential absorptions are largest above 490 nm while interference by O<sub>4</sub> and H<sub>2</sub>O is smaller below 500 nm, so that the first two criteria compete against one another and a compromise has to be found.

Three wavelength windows were studied in detail:

- 425–450 nm (A);
- 450–500 nm (B);
- 500–565 nm (C).

#### Window A (425–450 nm, fit: O<sub>3</sub>, NO<sub>2</sub>, Ring)

This window is well suited for NO<sub>2</sub> retrieval (Figure 4). However, the differential absorption cross sections of ozone are only about  $6 \cdot 10^{-23}$  cm<sup>2</sup> peak-to-peak in this region. Assuming for example an ozone vertical column of 300 DU and an AMF of 4 (corresponding to a solar zenith angle around 70°), a differential optical density of only  $2 \cdot 10^{-3}$  results. (For comparison: The UV differential optical density around 328 nm for the same slant column would be near 0.3 which is larger by a factor 150.) Additional errors can easily be introduced by a changing etalon effect. As a result ozone fits are not recommended to be used from this window.

#### Window B

##### (450–500 nm, fit: O<sub>3</sub>, NO<sub>2</sub>, O<sub>4</sub>, Ring)

This or a similar window is commonly used for determining ozone columns from ground-based DOAS measurements. Ozone differential absorptions are about five times higher than in window A. It includes only weak water absorption bands and an O<sub>4</sub> band which does not correlate with ozone. However, the GOME measurements are compromised by residuals dominated by “dichroic ripples” (Figure 5). These are introduced by the wavelength dependence of the instrumental nadir polarisation sensitivity  $\eta$ , which is dominated in this wavelength region by the behaviour of the dichroic mirror separating the light

between GOME channels 3 and 4. (For details see *Eisinger et al.*, this issue.) Until the  $\eta$  issue in the key parameters is resolved, this window is also not to be recommended for O<sub>3</sub> retrieval.

#### Window C

##### (500–565 nm, fit: O<sub>3</sub>, NO<sub>2</sub>, O<sub>4</sub>, H<sub>2</sub>O)

As ozone absorption cross sections are comparable to those in window B ozone fit errors are expected to be relatively small in this window. The polarisation sensitivity  $\eta$  is smooth (no small-scale structure) and should not disturb the fits. Indeed, when solar zenith angles are not too low, ozone can be fitted with low residuals (Figure 6). However, an O<sub>4</sub> band at 530 nm and (although to a less extent) two H<sub>2</sub>O bands at 500–513 nm and 537–554 nm are interfering with ozone absorption bands. Interference is confirmed by the differences in the fitted O<sub>3</sub> slant columns if O<sub>4</sub> (or H<sub>2</sub>O) are also fitted in addition to O<sub>3</sub>. The differences can be 10–20%. The ozone columns from this window are also sensitive to the order of the fitted polynomial. They are higher for a 4th order polynomial than for a 2nd order polynomial. This means the polynomial might interfere with ozone absorption.

For operational processing it is important to note that windows B and C are large (containing 240–310 detector pixels), thus increasing the computer time per DOAS fit considerably.

#### Summary

It is clear that window A is not suited for ozone fits in the visible. The choice between window B and C depends mainly on the evolutionary status of the GDP. In the long run improvements in the polarisation correction should result in reliable ozone fits using window B. In the meantime window C represents a good alternative. Interference by O<sub>4</sub> and H<sub>2</sub>O, however, has to be carefully investigated. In the next section some GDP results from a window similar to C will be discussed. This window (C') has been made somewhat smaller than C to reduce processing time. Unfortunately, thereby also O<sub>4</sub> interference is increased (compared to C).

## 3 Validation of ozone columns retrieved in the VIS window

In this section the total ozone vertical columns retrieved from the 510–560 nm (VIS) window (C') are compared with the total ozone column retrieved from the 325–335 nm (UV) window. Both ozone columns were derived with the GDP level 1–2 software (version 1.20). The DOAS fitting included the following species: O<sub>3</sub>, NO<sub>2</sub>, and BrO in the UV window and O<sub>3</sub>, NO<sub>2</sub>, and O<sub>4</sub> in the visible window. The solar spectrum was included in the linear part of the

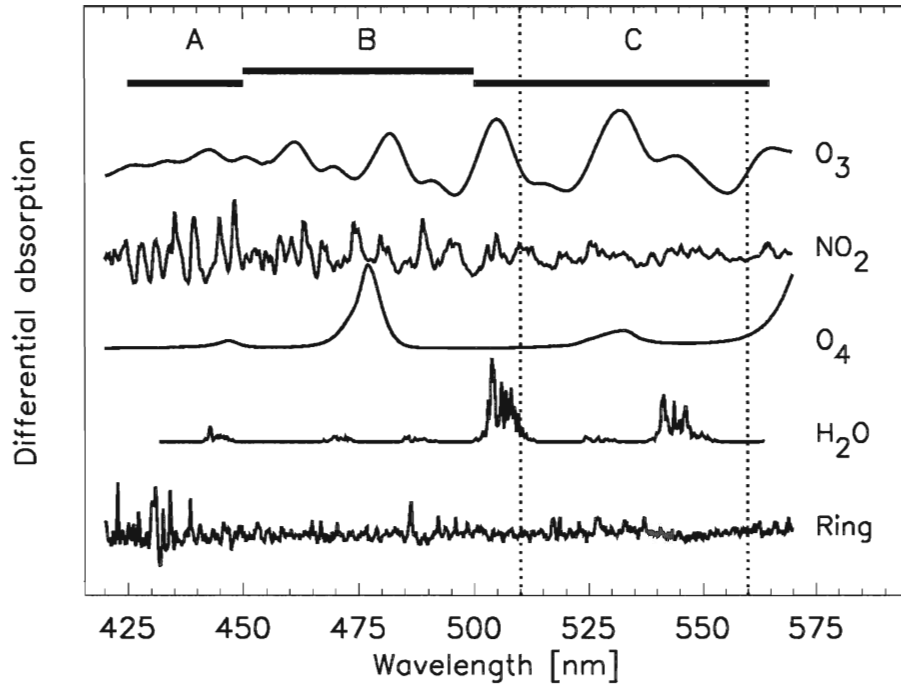


**Figure 3:** Differential absorptions of the most important gases and empirical “Ring spectrum” in the visible part of the spectrum (GOME channel 3). Note that the amplitudes are not to scale. The bars indicate the three test windows used in this study. The vertical dotted lines are the borders of the VIS fitting window C’ used by the GDP in version 1.20 (until November 1995). Results from this window are discussed in section 3. In Version 1.21 the GDP moved to window A.

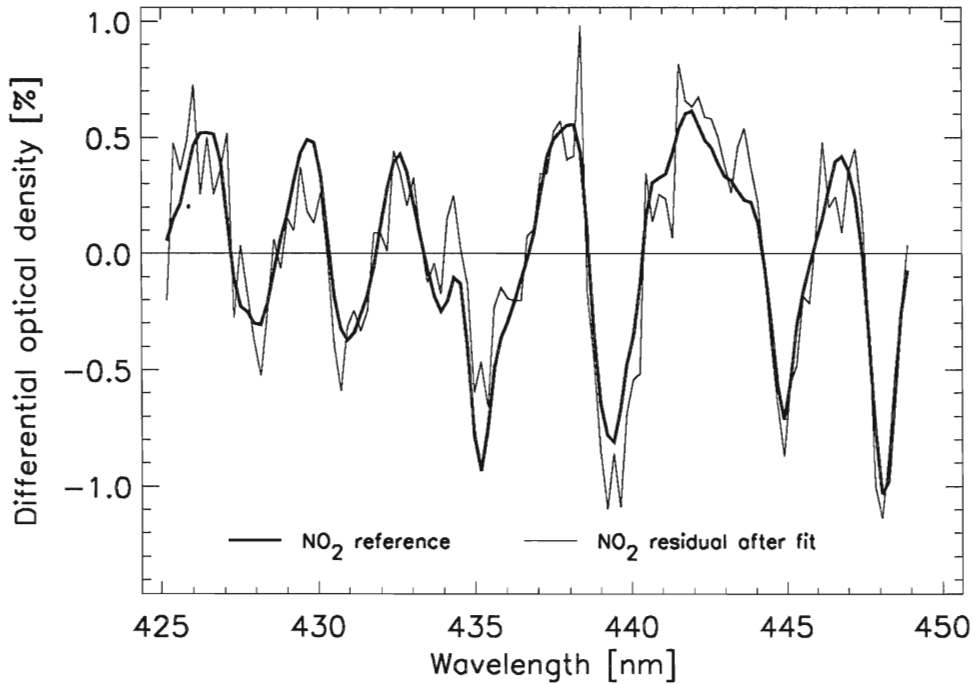


**Figure 4:** Window A: NO<sub>2</sub> fit results for groundpixel 3206 from orbit 2123 (16th September 1995, 11:12:42 UT, integration time 6 s, solar zenith angle 86.97°, latitude 81.04°N, longitude 99.27°E).

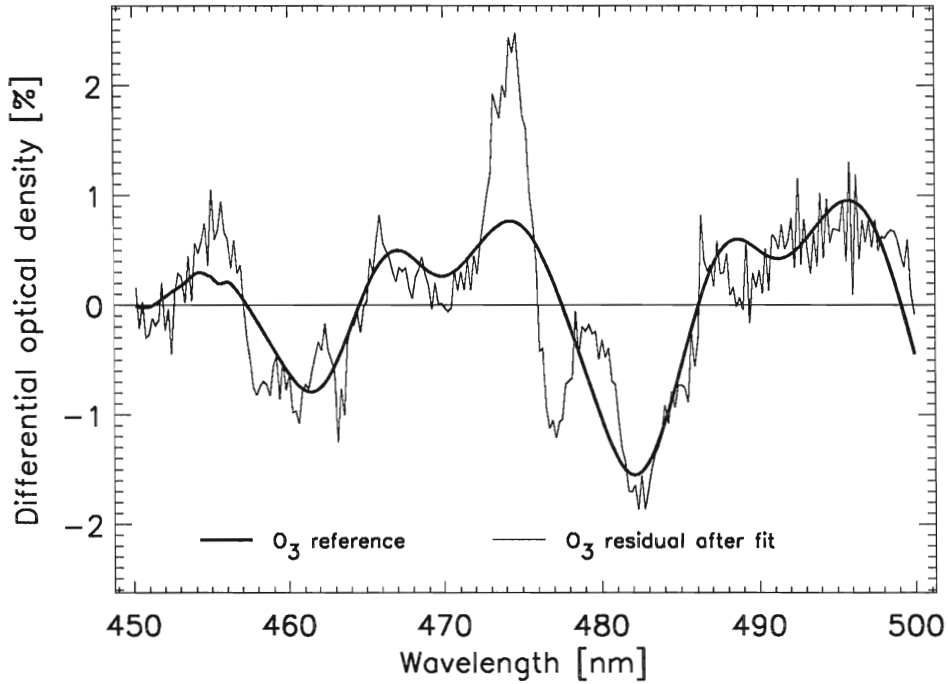


**Figure 5:** Window B:  $O_3$  fit results for groundpixel 3236 from orbit 2123 (16th September 1995, 11:13:29 UT, integration time 1.5 s, solar zenith angle  $84.37^\circ$ , latitude  $84.23^\circ N$ , longitude  $80.23^\circ E$ ). The large residuals around 457 nm and 477 nm are mostly introduced by an inadequate polarisation correction.

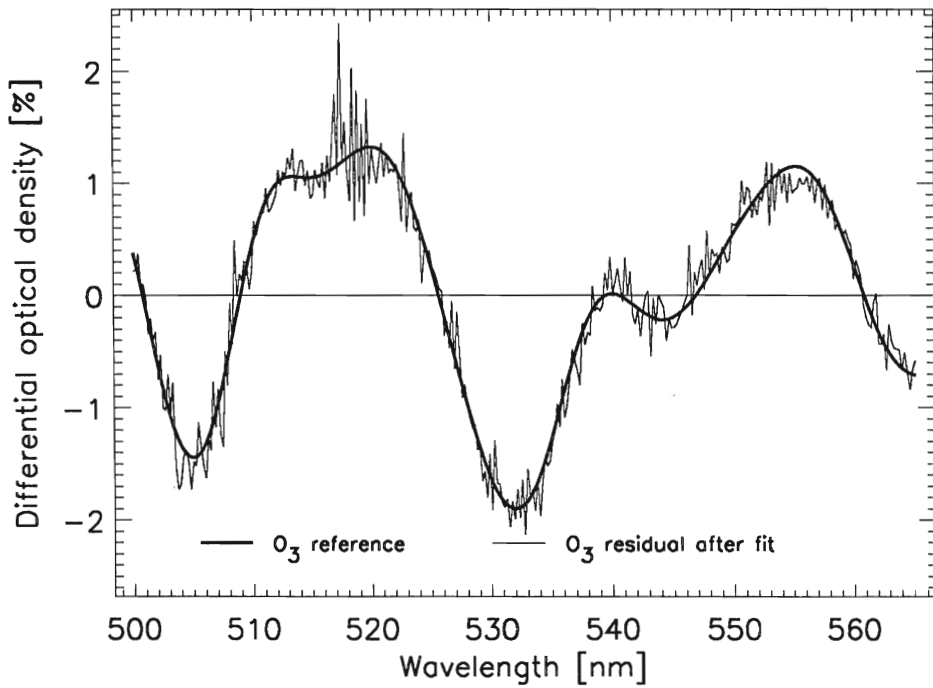


**Figure 6:** Window C:  $O_3$  fit results for groundpixel 3236 from orbit 2123. The residuum is somewhat larger between 515 and 520 nm due to the Ring effect. Fit results: Ozone slant column 2640 DU, fit error 2.4%.

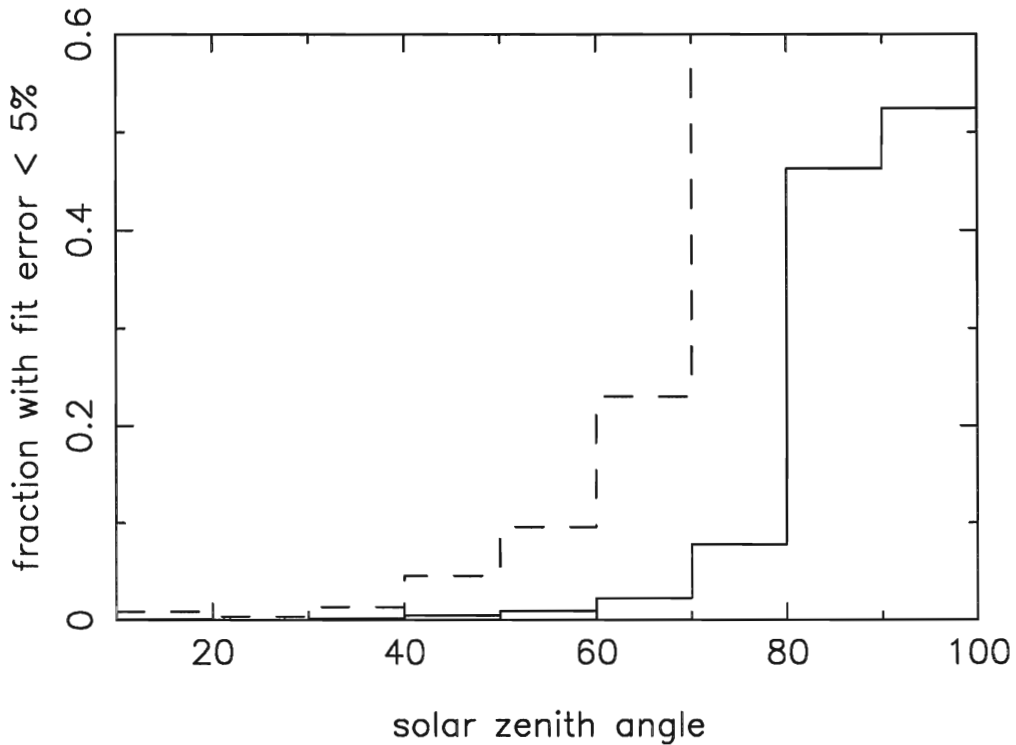


**Figure 7:** The fraction of VIS ozone values with fit errors less than 5% (solid line). The dashed line is the same, but enhanced by a factor 10.

fitting process, but the Ring spectrum was not included. A total of 15 days of GOME data (between approximately 6 UT and 22 UT) have been used in this comparison: 23–25 July, 25–27 August, 15–17 September, 5–7 and 29–31 October.

In the level 1–2 software version considered in this study, AMFs for the visible window were calculated assuming single scattering, while the AMFs for the UV window (for solar zenith angles less than  $74.6^\circ$ ) were calculated assuming multiple scattering. Since single scattering AMFs normally are lower than multiple scattering AMFs the total ozone columns retrieved from the visible window are expected to be a few percent higher than the UV values. For a first comparison of total ozone columns retrieved from the visible window with those from the UV window, all values having solar zenith angles less than  $74.6^\circ$ , with ozone fit errors (both UV and VIS) less than 5%, and with viewing angles less than  $7^\circ$  (“nadir” pixels) were selected.

### 3.1 Comparison of UV and VIS ozone from the GDP

Only a relatively small number of the ozone values retrieved from the visible window by the current version of the GDP have fit errors less than 5%. In general fit errors are smaller for larger values of the slant ozone column, so the number of values with fit errors smaller than 5% increases with increasing solar zenith angle (Figure 7).

Figure 8 shows the comparison of the two  $O_3$  re-

trievals for the 514 selected values. The majority of the ozone total column values retrieved from the visible window correlate well with values retrieved from the UV window, however the columns from the visible window are about 30% higher. These values have a range of about 8%. The latter arises in part from the errors associated with individual ozone values (the average fit error in the VIS values is 4.5%, and in the UV values 1.9%).

About 15% of the selected VIS values are more than 60% and up to a factor 4 larger than the corresponding UV values. The DOAS fit errors, however, are smaller than 5% (the selection criterium). In order to understand why the VIS values are so high in some cases, one GOME orbit was examined in more detail as described in the next subsection.

#### Dependence on ICFA cloud cover fraction

In Figure 9 an example is given of the behaviour of the total ozone column retrieved from the visible window compared to that retrieved from the UV window. Shown are the GOME data of the 16th September, 1995, between 9:56 and 10:23 UT (orbit 2123, Southern Hemisphere). This orbit is nadir static (the scan mirror was fixed to the nadir-looking position) so subsequent values are only about 10 km apart for solar zenith angles below  $75^\circ$ . The error bars plotted are the DOAS fit errors. Note that in this plot all values are shown (i.e., not only those with fit errors smaller than 5%, as in the previous subsection). The UV values show the expected relatively smooth be-



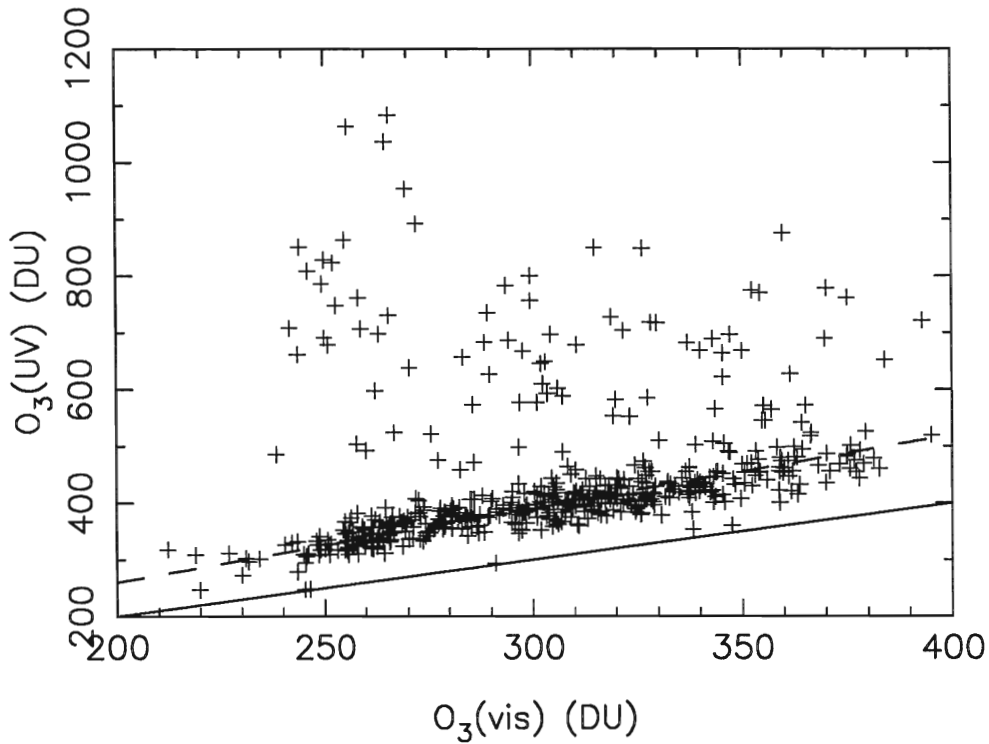


**Figure 8:** The total ozone (vertical) column as retrieved from the visible window,  $O_3(\text{vis})$ , versus the ozone column from the UV window,  $O_3(\text{UV})$ . The solid line is the line  $O_3(\text{vis}) = O_3(\text{UV})$ . 85% of the data is distributed around the line  $O_3(\text{vis}) = 1.30 \cdot O_3(\text{UV})$  (dashed), with a spread of about 8%.

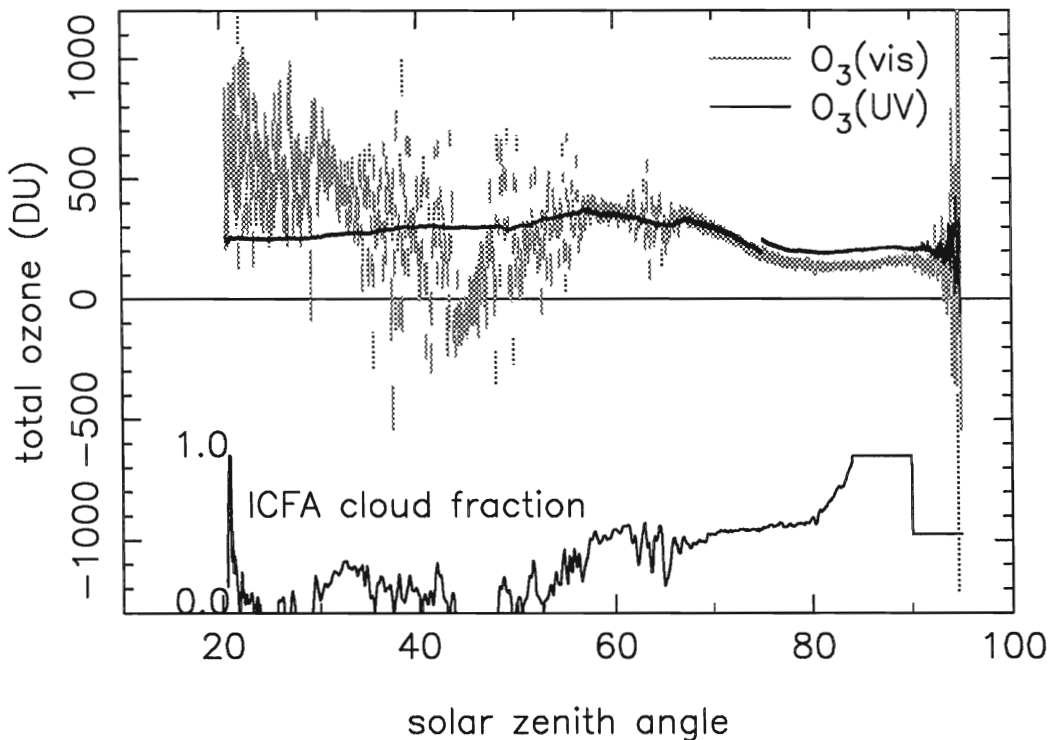


**Figure 9:** The total ozone columns for 16th September 1995, between 9:56 UT and 10:23 UT as a function of the solar zenith angle (Southern hemisphere). The error bars are the DOAS fit errors: UV values in black, and VIS values in grey. The solid line at the bottom indicates the corresponding ICFA cloud-cover fraction. The jump in the UV values at a solar zenith angle of  $74.6^\circ$  is caused by the assumption of single scattering used for the calculation of AMFs above this solar zenith angle. This will be changed in future versions of the GDP.

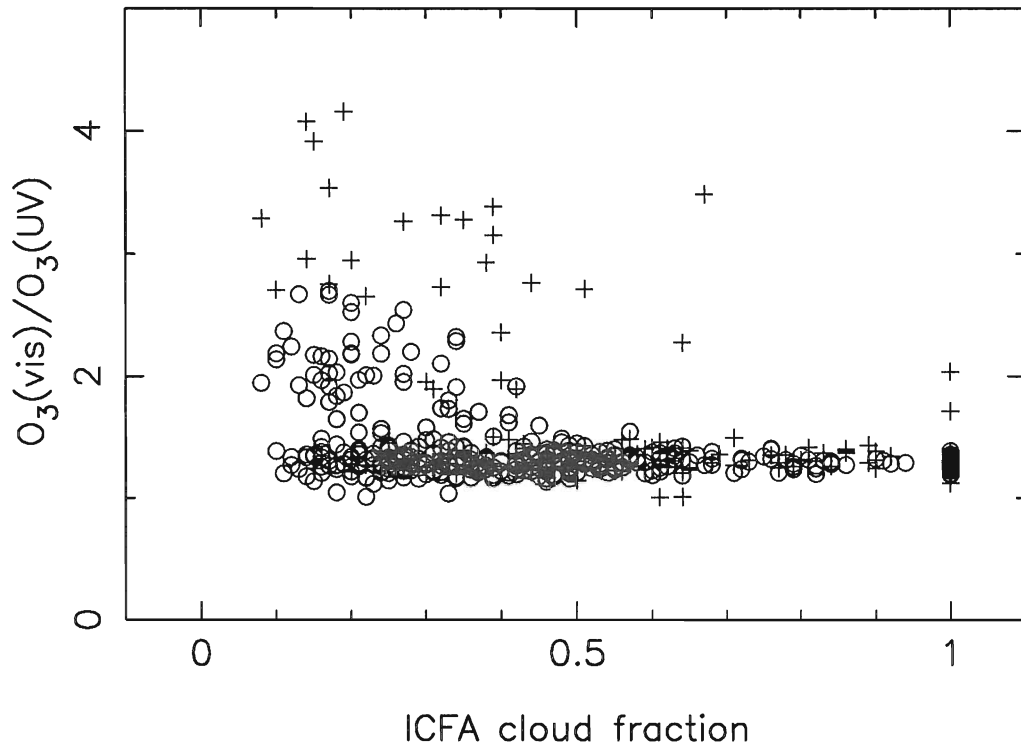


**Figure 10:** The ratio of the vertical ozone column retrieved from the visible window and that retrieved from the UV window as a function of the ICFA cloud-cover fraction. Included are only those values for which the DOAS fit errors are less than 5%. Circles indicate (UV) ozone values larger than 280 DU, crosses indicate smaller ozone values.

haviour. The VIS values show a smooth behaviour for a few restricted time intervals (= solar zenith angle intervals). In other time periods the VIS values are widely spread around the UV values. The cloud-cover fraction as calculated by the initial cloud fitting algorithm (ICFA) is plotted in the same figure. It appears that regions with high cloud-cover (> 0.5) result in a “better” behaviour of the VIS values than regions with low cloud-cover. This hypothesis was tested by studying the behaviour of the ratio of the VIS value and the UV value with respect to the ICFA cloud-cover fraction (Figure 10). The data used are the same as in the previous subsection (solar zenith angles less than  $74.6^\circ$ , fit errors less than 5%, only “nadir” pixels). It appears that large deviations between UV values and VIS values occur mostly in pixels with small cloud-cover fractions. Furthermore, it appears that the deviations can be larger (both absolute and relative) for smaller (UV) ozone values (< 280 DU). Also it is clear from Figure 10 that most of the VIS values are comparable to the UV values (apart from a small systematic difference as discussed earlier). Even for very small cloud-cover fractions (< 0.2) half of the VIS values correlate well with the UV values.

In summary, the total ozone column retrieved from the visible window (510–560 nm) is often larger than the column retrieved from the UV window, more often at lower ICFA cloud-cover fractions, and with (on average) larger deviations for smaller (UV) ozone

columns.

### 3.2 Discussion

DOAS fit errors for ozone retrieved from the visible window are in general much larger than those retrieved from the UV window. But the (relatively few) VIS values with small fit errors (< 5%) are in most cases (85%) comparable to the corresponding UV values, apart from a systematic offset.

The 30% systematic offset (the VIS values being higher than the UV values) can at least partly be caused by the assumption of single scattering in the calculation of the VIS AMFs. However, AMF calculations performed at KNMI (*Koелеmeijer, 1996*) and at IUP Bremen (*Buchwitz, 1996*) show that the differences between single scattering AMFs and multiple scattering AMFs in the visible are probably not much larger than about 10%. There are therefore other contributions to this behaviour.

In addition, further 15% of the VIS values with small fit errors are much larger (60% up to a factor 4) than the corresponding UV values.

The tests done in section 2.3 show that there is strong *interference* of the ozone reference spectrum with the reference spectra of  $O_4$  and  $H_2O$ . Leaving one (or both) of these latter species out of the fitting process results in ozone deviations of 10–20%. Although this is a considerable amount it does not account for the large deviations found in section 3.1

(e.g., Figure 8).

*Etalon* structures, which can appear in the differential spectrum if the solar and the earth spectrum are observed with a relatively long time gap, can interfere with the ozone structures. This would, however, result in an alternating in time of “wrong” and “right” VIS values on a rather long timescale. This is not observed.

In the previous subsection it was shown that the large deviations occur more often at low ICFA cloud-cover fractions. Clouds play an important role in the visible window: the intensity of the backscattered solar radiation, is usually higher for a cloudy sky than for a clear sky. This is less significant in the UV range. This suggests that the retrieval of ozone in the VIS is sensitive to the signal level. High radiances mean high *signal-to-noise* ratio. However, it is difficult to understand why the VIS value is not in all cases affected by this sensitivity. Still most of the VIS values appear to be o.k.

It might be that the wavelength dependence of the *surface albedo* interferes with the ozone reference spectrum. This effect can only show up when the pixel is not fully cloudy. And it might be different for different types of surfaces.

Another possibility is that it has something to do with the *polarisation* of the radiance, because clouds (and ice surfaces) tend to depolarise the radiation. In window C' the polarisation sensitivity is a relatively smooth function of wavelength (no differential structures), but it is not yet clear whether this polarisation sensitivity is fully accounted for by the fitted polynomial, or whether a residual can still be in the spectrum which then can interfere with ozone.

Since VIS window C' is quite large the possibility of *spatial aliasing* should at least be mentioned. The systematic offset observed can however not be explained by spatial aliasing which should result in symmetrical deviations.

### 3.3 Conclusions

In section 3.1 it was stated that the relative ozone fit error in the visible window is smaller for larger solar zenith angles, caused by the increasing *slant* columns as a function of solar zenith angle. Furthermore, the spatial variability of the VIS values is much smaller at large solar zenith angles than at small solar zenith angles (Figure 11). This is possibly related to the behaviour of the VIS values as a function of the reflectivity or the cloud-cover fraction (section 3.1). For solar zenith angles larger than 70° the average ICFA cloud-cover fraction for the 15 days studied is larger than 0.5. Note that the pixel-to-pixel variation of the UV values *increases* with solar zenith angle, from about 3 DU for angles smaller than 50° to 16 DU for angles larger than 90°. The small fit error and small spatial variability of the VIS ozone values for large solar zenith angles, indicates that ozone columns from the absorption in the visible should be of high precision. That there are some

VIS ozone values with small fit errors which deviate strongly from the UV values should be a reminder not to equate fit errors and total errors of the vertical columns.

After changes to the GDP (e.g. AMFs with multiple scattering, GOME FM reference spectra) it is anticipated that the VIS ozone values might change by 10-50% from the present values.

Finally, it is of importance that the VIS ozone can be derived for larger solar zenith angles than the UV ozone. This is especially important in spring in both polar regions when the depletion of ozone becomes important.

## 4 Conclusions and Recommendations

### 4.1 Slant column fitting (DOAS)

It is recommended for the level 1–2 processing to use O<sub>3</sub>, NO<sub>2</sub>, and “Ring” spectra measured with the GOME flight model as reference spectra. For the UV window from which the GOME *main* product is calculated at present, it is recommended to exclude NO<sub>2</sub> and BrO from the fit and to include fitting of a Ring spectrum. The solar irradiance has to be excluded from the linear fit. These and some other recommendations have already been discussed and will be implemented in the next version of the GOME Data Processor.

Concerning the VIS window the situation is more complicated. In the tests described in section 2.3 were only slant columns were calculated. However, fit quality is only one criterion. Accuracy of vertical columns has to be the final criterion. During the Validation Campaign in the GDP first a window 510–560 nm (C'), then 425–450 nm (A, the “NO<sub>2</sub> window”) was used. The comparison between ozone vertical columns retrieved from C' and those retrieved from the UV (section 3) indicates a good potential for window C' but the columns are still systematically too high. Furthermore, interference by O<sub>4</sub> and H<sub>2</sub>O cannot be neglected above 500 nm. The 450–500 nm (window B) fits were shown to be disturbed by “dichroic residuals” due to a non-perfect polarisation correction. Their influence on ozone vertical columns retrieved from window B, however, still has to be estimated. Therefore, it is suggested to test also window B in the GDP by choosing it as the visible window for some time of the operational processing (e.g., to process with window B the same days which were already processed with window C', which would allow a direct comparison between both VIS windows.) The results can then again be compared to the results from the UV window which should enable a “final” decision on the optimal fitting window in the visible. Of course, in parallel the keydata (and possibly the polarisation correction algorithm) will have to be modified in such a way that the “dichroic residuals” in window B are minimised.

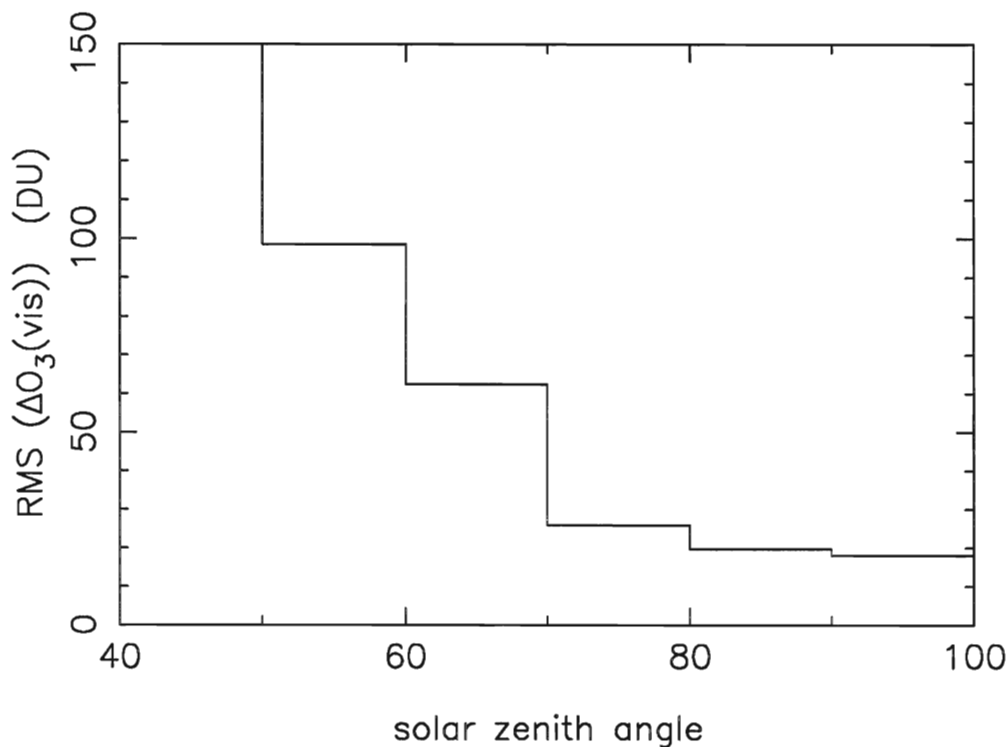


**Figure 11:** Pixel-to-pixel variation of the ozone columns retrieved in the visible, expressed in rms difference between the VIS values from neighbouring pixels (maximum distance 40 km) as a function of solar zenith angle.

## 4.2 Air mass factors

We believe that most of the remaining discrepancies between GOME and ground-based measurements are caused by air mass factors. On the one hand, there are principal limitations because the knowledge of the state of the atmosphere is always less than what is required for “exact” calculations, so that climatological profiles have to be assumed. However, there is still a lot of potential for improvements in the current AMF algorithm. Due to historical reasons at present single scattering AMFs are calculated by one radiative transfer model (AMFTRAN) and afterwards corrected for multiple scattering with factors calculated by another model (GOMETRAN++). This separation is not only artificial but inconsistent because the two models are known to yield somewhat different results in their single scattering modes. It is strongly recommended for future versions of the GDP to calculate *only* multiple scattering AMFs. If this is not possible *on-line* for each ground pixel (which is expected due to processing time limitations) look-up tables for the multiple scattering AMFs have to be created from which the actual values can then be interpolated.

## 4.3 Outlook

It was pointed out that ozone columns retrieved from the UV have their strength at low solar zenith angles because AMFs are best known there. Ozone columns from the visible region are most reliable at large solar zenith angles since absorbances are high there. For very large zenith angles retrieval from the VIS is su-

perior compared to the UV because the UV radiation will not reach the lower atmosphere any longer (the UV sun has already set). It is therefore natural to envisage a “smart” combination of UV and visible for the main ozone product, thereby taking full advantage of the enormous wealth of spectral information from the multi-channel instrument GOME.

## Acknowledgements

We thank W. Balzer, D. Loyola, E. Mikusch, W. Thomas (DLR-DFD), and R. Spurr (DLR/SAO) for their patience in putting up with and thinking over our numerous and long lists of wishes for “improvements” of the GOME Data Processor. We are grateful to M. van Roozendaal (IASB) for redrawing our attention to the O<sub>4</sub> interference in the visible region and to M. Weber (IUP) for helpful comments. This work was funded in part by the University of Bremen, the State of Bremen, DARA (contract No. 50EE9439), and SRON, The Netherlands.

## References

- Bass, A. M., and R. J. Paur, The ultraviolet cross-sections of ozone, *Proc. Quadr. Ozone Symp. 1984, Halkidiki, Greece*, 1985.
- Buchwitz, M., private communication, 1996.
- Burkholder, J. B., private communication.
- Burrows, J. P., *et al.*, SCIA-Mini, Proposal to ESA, Max-Planck-Institut für Chemie, Mainz, 1988.

Burrows, J. P., *et al.*, Study of the Ring Effect, ESA Contract No. 10996/94/NL/CN, 1995.

Chance, K., private communication, 1994.

Dehn, A., Temperaturabhängige Absorptionsspektroskopie bedeutender Spurengase der Atmosphäre im ultravioletten und sichtbaren Spektralbereich, Thesis, University of Bremen, 1995.

Diebel, D., *et al.*, Tracegas study: Detailed analysis of the retrieval algorithms selected for the level 1-2 processing of GOME data. Final progress report, 1995.

Dobson, G. M. B., and D. N. Harrison, *Proc. Roy. Soc. London*, **A110**:660, 1926.

Edlén, B., The dispersion of standard air, *J. Opt. Soc. Am.*, **43**:339–344, 1953.

Eisinger, M., *et al.*, Studies on the precision of GOME irradiance and radiance products... , this issue. \*

von der Gathen, P., private communication, 1996.

Greenblatt, G. D., *et al.*, Absorption measurements of oxygen between 330 and 1140 nm, *J. Geophys. Res.*, **D95**:18577–18582, 1990.

Global Ozone Monitoring Experiment: Interim Science Report, European Space Agency (ESA), SP-1151, 1993.

Harwood, M. H., and R. L. Jones, Temperature dependent ultraviolet-visible absorption cross sections of NO<sub>2</sub> and N<sub>2</sub>O<sub>4</sub>, *J. Geophys. Res.*, **D99**:22955–22964, 1994.

Koelemeijer, R., private communication, 1996.

Noxon, J. F., Nitrogen dioxide in the stratosphere and troposphere measured by ground-based absorption spectroscopy, *Science*, **189**:547–549, 1975.

Noxon, J. F., *et al.*, Stratospheric NO<sub>2</sub>. 1. Observational method and behavior at mid-latitude, *J. Geophys. Res.*, **C84**:5047–5065, 1979.

Ozone Measuring Instruments for the Stratosphere, ed. by W. B. Grant, *Opt. Soc. Am.*, 1989.

Perner, D., and U. Platt, Detection of nitrous acid in the atmosphere by differential optical absorption, *Geophys. Res. Lett.*, **6**:917–920, 1979.

Product Specification Document of the GOME Data Processor, Deutsche Forschungsanstalt für Luft- und Raumfahrt (DLR), ER-PS-DLR-GO-0016, 1995.

Richter, A., *et al.*, Ground based UV/vis measurements of O<sub>3</sub>, NO<sub>2</sub>, BrO, and OCIO over Bremen (53°N), *Proc. 3rd European Symposium on Polar Stratospheric Ozone Research, Schliersee, Germany, 1995*.

Schneider, W., *et al.*, Absorption cross sections of NO<sub>2</sub> in the UV and visible region (200–700 nm) at 298 K, *J. Photochem. Photobiol.*, **A40**:195–217, 1987.

Solomon, S., *et al.*, On the interpretation of zenith sky absorption measurements, *J. Geophys. Res.*, **D92**:8311–8319, 1987.

---

M. Eisinger, present address: Alfred Wegener Institute for Polar and Marine Research, D-14401 Potsdam.

A. Richter and J. P. Burrows, Institute of Environmental Physics, University of Bremen, D-28334 Bremen.

A. Pijpers, Royal Dutch Meteorological Institute, NL-3730 AE De Bilt.

GOME Validation Projects D-131 and NL-112

---

\* Proceedings of the GOME Geophysical Validation Campaign, ESA WPP-108, ESA/ESTEC, Noordwijk (1996)



## GROUND-BASED MEASUREMENTS AT KNMI USED FOR GOME VALIDATION

Ankie J.M. Piters, Pieter F. Levelt, Foeke Kuik, Marc A.F. Allaart, and Hennie M. Kelder  
KNMI, PO Box 201, 3730 AE De Bilt, The Netherlands

**Abstract**

During the validation campaign of GOME, ground-based measurements of total ozone and of ozone profiles have been performed at KNMI, The Netherlands. Total ozone columns have been measured with a Brewer instrument around the GOME overpass times. Sondes, measuring the ozone profiles, were launched when it was most likely that the sonde would measure the same air mass as GOME at the overpass time. The retrieved GOME total ozone columns are on average 4–5% lower than the corresponding Brewer values.

**1. INTRODUCTION**

During the 6 months validation campaign (21 July 1995 – 23 January 1996) of the Global Ozone Monitoring Experiment (GOME) on board the European satellite ERS-2, KNMI (De Bilt) performed ground-based measurements of total ozone and ozone profiles. The total ozone measurements, obtained with a Brewer instrument, are used for direct comparison with the total ozone columns retrieved from GOME observations. The first results of this comparison are presented here. The ozone profiles, obtained with ECC sondes, will be used for validation of (future) GOME ozone profiles. The development of profile retrieval algorithms using forward modelling methods will also benefit from these ozone sonde profiles. The retrieval algorithms will be used for validation of GOME ozone profile retrieval.

In Section 2 we shortly describe the instruments used. Section 3 discusses the selection criteria used for the comparison of the total ozone columns measured with the Brewer instrument with those retrieved from GOME observations. In the same Section we present the strategy used for launching the ozone sondes. In Section 4, we show the first results of the comparison of GOME total ozone with the Brewer measurements.

**2. THE INSTRUMENTS****2.1. Brewer spectrophotometer**

The Brewer instrument is a double monochromator type MK III. Brewer #100 is operational at KNMI since 1 January 1994. The Brewer derives total ozone, using the measurement of solar radiation at four wavelengths (310.1 nm, 313.5 nm, 316.8 nm, and 320.1 nm). The radiance calibration and wavelength stability of the Brewer are checked several times a day with an internal tungsten halogen lamp and an internal mercury lamp, respectively. In normal operational mode total ozone is measured roughly every 15 minutes from sunrise to sunset. When the sun is visible, direct solar radiation is measured. These 'direct sun measurements' have a precision (i.e., due to measurement uncertainties) of 1%. When the sun is not visible, the Brewer measures the solar radiation scattered from the zenith. These 'zenith sky measurements' have a precision of 5%. However, the *accuracy* (i.e., due to systematic errors) can be larger than these measurement

uncertainties. Comparison of the observations from the Brewer #100 and those from the Brewer in Uccle (#16; 50.8 N, 4.35 E) show that a possible systematic offset between these two instruments is less than 2%, part of this offset may even be caused by a ('real') average ozone gradient over the distance between De Bilt and Uccle (~ 170 km). Near-simultaneous zenith sky and direct sun ozone values can differ up to 8%.

**2.2 Ozone sondes**

The ozone sondes used at KNMI are Electrochemical Concentration Cell (ECC) sondes, which measure profiles up to an altitude of approximately 30 km, with a resolution of about 100 m. Also measured are the pressure, temperature, humidity, and position of the sonde. The accuracy of the measured ozone partial pressure is estimated to be better than 10%. Ozone sondes are normally launched once a week, more often during the GOME validation campaign (see Section 3). The quality checks performed on the observed profiles include the comparison of the Brewer total ozone column with the integrated profile. If the integrated profile differs from the Brewer total ozone column by more than 30 DU, the profile is marked unreliable.

**3. DATA SELECTION AND MEASUREMENT STRATEGY****3.1 Total ozone**

The data used for the validation of the total ozone column is listed in Table 1. For the comparison of Brewer total ozone values with GOME values we used only Brewer direct sun measurements, because of the larger uncertainties in the zenith sky measurements (see Section 2.1). From the GOME data we selected one ground pixel per day, the one closest to De Bilt (52.1 N, 5.18 E). The value retrieved from this GOME pixel was compared with the Brewer (direct sun) measurement closest in time to the GOME overpass time. Due to possible strong gradients in the ozone field, e.g. during front passages, total ozone amounts can differ up to 50–100 DU for distances in the order of 200 km and a time interval of about two hours. The distances of the closest GOME pixel to De Bilt can still be as large as 400 km, and the difference in time between the two measurements can be as large as 4 hours (for cloudy days; see Table 1). In these cases, a direct comparison with the Brewer measurement, in the presence of strong gradients in the ozone fields, will be of less value than when the GOME pixel co-incides with the De Bilt measurement, both in time and in place. Therefore, we classified the Brewer data used for the comparison in Section 4 with respect to their distance to the closest GOME pixel centre, and with respect to their time difference with the GOME observing time.



Table 1: The data used for the validation of the total ozone column. Column 1 gives the day of the observation; columns 2 and 3 the time (UT) and value (DU) of GOME total ozone; columns 4 and 5 the time (UT) and value (DU) of Brewer (direct sun) total ozone; column 6 lists the difference  $\Delta O_3$  in DU between GOME and Brewer total ozone value; column 7 gives the distance ('dist') in km from the GOME pixel centre to De Bilt; column 8 the pixel-type (B, E, N, C, W, corresponding to five different scanning angles of the instrument mirror: approximately  $-23^\circ$ ,  $-13^\circ$ ,  $0^\circ$ ,  $+7^\circ$ ,  $+27^\circ$ , respectively); column 9 gives the solar zenith angle ('sza'); column 10 the cloud cover fraction as calculated by the GOME Data Processor.

day	GOME time	GOME O <sub>3</sub>	Brewer time	Brewer O <sub>3</sub>	$\Delta O_3$	dist	type	sza	cloud fraction	day	GOME time	GOME O <sub>3</sub>	Brewer time	Brewer O <sub>3</sub>	$\Delta O_3$	dist	type	sza	cloud fraction
23-7	10:12:23	302	10:16	304	-2	278	W	32.2	0.19	16-9	11:23:31	298	11:37	293	5	123	B	51.0	0.20
24-7	11:20:47	310	11:17	311	-1	80	B	34.2	0.10	17-9	10:52:19	295	10:51	302	-7	67	C	50.0	0.18
25-7	10:49:29	287	10:53	294	-7	20	C	33.5	0.14	20-9	10:58:03	287	10:42	300	-13	133	E	51.2	0.41
25-8	11:15:01	300	10:45	294	6	16	B	42.9	0.43	21-9	10:26:39	265	10:25	284	-19	40	W	50.9	0.40
26-8	10:43:43	280	10:47	286	-6	78	C	42.2	0.27	22-9	11:34:50	253	9:12	266	-13	303	B	53.8	0.27
27-8	10:12:18	306	10:22	309	-3	278	W	41.9	0.43	23-9	11:03:43	257	9:44	269	-12	39	E	52.6	0.54
29-8	10:49:23	299	10:52	305	-6	26	C	43.4	0.32	27-9	10:37:59	294	10:37	289	5	157	W	53.7	0.19
30-8	10:18:03	320	10:09	316	4	182	W	42.8	0.30	28-9	10:06:38	300	10:46	323	-23	375	W	53.2	0.19
31-8	11:26:21	320	10:58	326	-6	168	B	45.3	0.20	1-10	10:12:24	235	15:00	245	-10	278	W	54.3	0.57
1-9	10:55:09	306	10:15	317	-11	114	C	44.4	0.00	2-10	11:20:47	233	11:20	254	-21	80	B	56.7	0.45
2-9	10:23:43	280	12:43	310	-30	85	W	44.1	0.69	3-10	10:49:29	274	9:38	284	-10	20	C	56.0	0.45
3-9	11:32:00	313	11:44	334	-21	259	B	46.6	0.30	5-10	11:26:27	303	11:49	308	-5	170	B	58.1	0.11
4-9	11:00:47	294	11:04	311	-17	87	E	45.7	0.39	6-10	10:55:09	276	10:50	301	-25	114	C	57.4	0.06
5-9	10:29:30	283	10:20	302	-19	407	N	45.0	0.16	7-10	10:23:49	259	8:35	287	-28	85	W	56.8	0.53
6-9	11:37:43	310	11:36	324	-14	347	B	48.2	0.21	29-10	10:32:22	273	10:40	284	-11	64	W	64.8	0.13
7-9	11:06:27	266	10:35	299	-33	15	E	47.0	1.00	30-10	11:40:27	262	11:38	280	-18	393	B	68.2	0.53
15-9	10:15:13	266	9:37	295	-29	230	W	48.4	0.35	11-11	10:23:40	243	10:21	271	-28	86	W	68.9	0.41

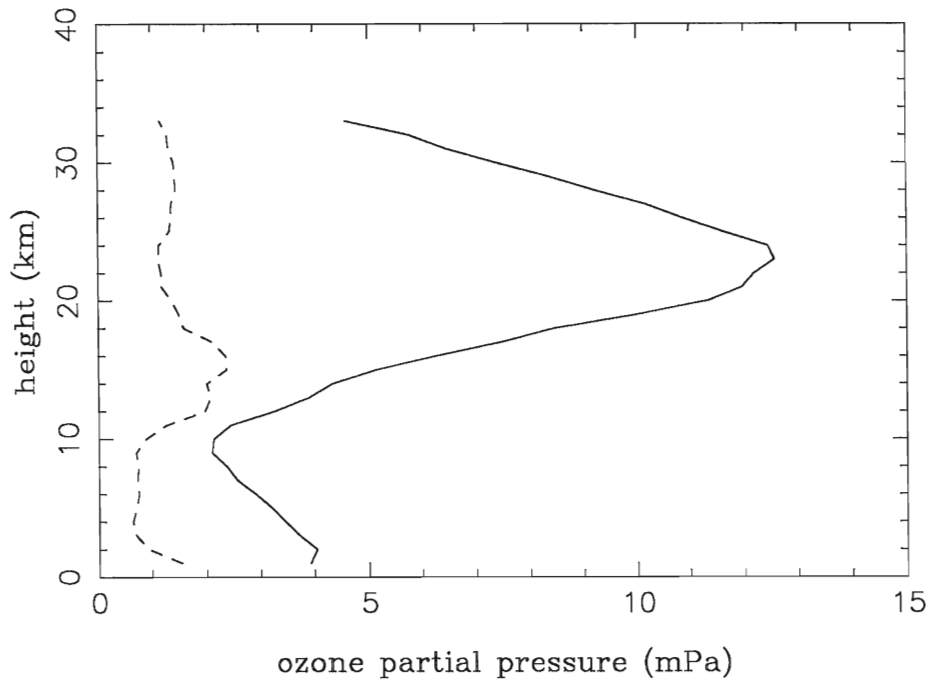


Figure 1: The average ozone profile of the 26 ozone sondes launched during the GOME validation period (solid line), and the standard deviation (dashed line).

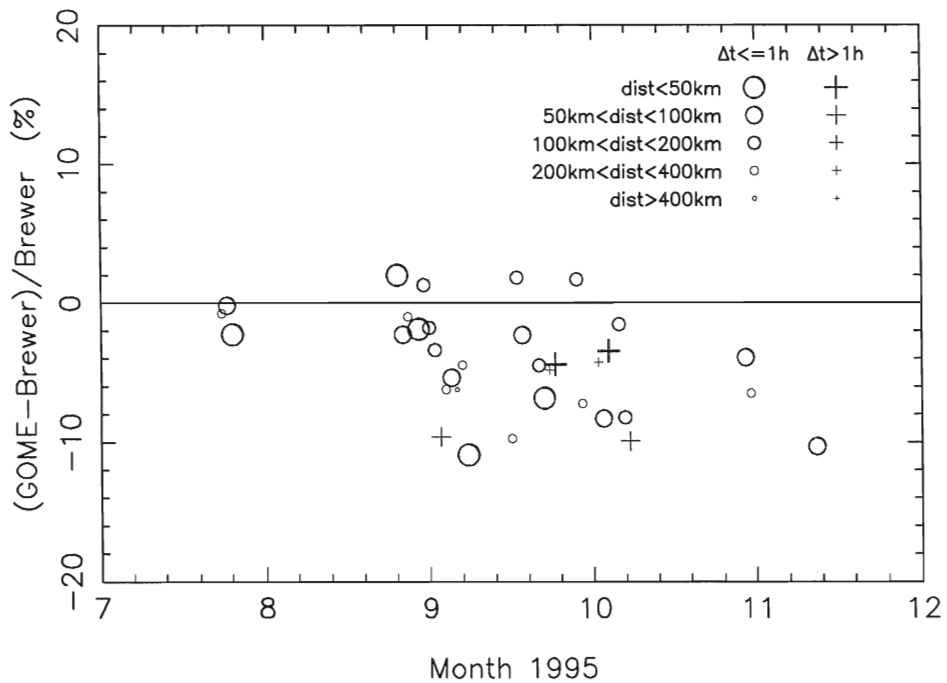


Figure 2: The relative difference between the GOME ozone column and the ozone column measured by the Brewer instrument as a function of time. Plusses denote values which have been measured with more than 1 hour time difference, circles denote values which have been measured with less than 1 hour time difference. The size of the symbols indicate the distance of the GOME pixel centre to De Bilt (large is close by, small is far away, see Table 1).

## 3.2 Ozone profiles

The ozone sondes have been launched only on those days for which the sonde was expected to fly through roughly the same air mass as that observed by GOME. This was estimated using the information on the movements of previous sondes. High priority was given to the launch of sondes which were expected to pass the ozone maximum (at an altitude between 15 and 20 km) at a (projected) position co-located with a GOME ground pixel. A total of 26 sondes resulted in reliable ozone profiles, and can be used for validation of future GOME ozone profiles. The average and standard deviation of these profiles is plotted in Figure 1.<sup>1</sup>

## 4. RESULTS AND DISCUSSION

The differences between the GOME total ozone columns and the Brewer values range from +2% to -11% (see Figure 2). The average offset of the GOME values with respect to the Brewer values is  $-4.4 \pm 0.6\%$  with a standard deviation of 4%. This standard deviation is partly caused by differences in time and space between the GOME and the Brewer observations. But even if the Brewer observation would be simultaneously measured and co-located with the GOME ground pixel, some scatter is expected due to the averaging of GOME over a  $40 \times 80\text{km}^2$  (or  $40 \times 240\text{km}^2$ ) ground pixel. The standard deviation of the differences between total ozone columns of GOME and Brewer is relatively small (4%) when compared to the variation in ozone itself ( $\sim 7\%$  for the studied period, Table 1). If we select only the values with a distance less than 100 km and a time difference less than 30 minutes, the average offset is  $-4.5 \pm 1.1\%$ , which is not significantly different from the average offset including all observations from Table 1, and the standard deviation is 3%. On the basis of this relatively limited data set (34 measurements) we cannot find a significant dependence on solar zenith angle or on the cloud cover fraction calculated by the GOME Data Processor or on the GOME viewing direction (as reported in several papers in this issue), but we cannot rule out such a dependence either. Sensitivity studies of this kind should be done using the total data set obtained by Brewer and Dobson instruments participating in the validation campaign (see also Koopman and Van der Woerd 1996).

## Acknowledgements

We gratefully acknowledge Hugo de Backer and Els Schoubs (KMI, Uccle, Belgium) for their cooperation in the comparison of the Brewer instruments. We would like to thank R. Agterberg, P. van der Veer, and R. Rothe for the preparation and launching of the ozone sondes. Ankie Piters is funded by SRON, The Netherlands, Pieter Levelt is funded by BCRS, The Netherlands.

## References

Koopman R.M., Van der Woerd H.J., Validation of GOME ozone columns using DOBSGOME and GOME ICFA cloud cover using ATSR-2, this issue, 1996

<sup>1</sup>The ozone variability is largest in a small vertical layer around 16 km, just above the tropopause. The total ozone column variability is dominated by the ozone variability in this vertical layer. This principle is used in the two-dimensional assimilation model developed at KNMI (see Piters et al. 1996).

Piters A.J.M., Levelt P.F., Allaart M.A.F., Kelder H.M., Validation of GOME total ozone column with the Assimilation Model KNMI, this issue, 1996 \*

\* Proceedings of the GOME Geophysical Validation Campaign, ESA WPP-108, ESA/ESTEC, Noordwijk (1996)

## CHAPTER 7

### VALIDATION OF GOME TOTAL OZONE COLUMN WITH THE ASSIMILATION MODEL KNMI

Ankie J.M. Piters, Pieter F. Levelt, Marc A.F. Allaart, and Hennie M. Kelder  
KNMI, PO Box 201, 3730 AE De Bilt, The Netherlands

#### Abstract

The two-dimensional global Assimilation Model KNMI (AMK) is used to validate GOME total ozone columns. A method is developed to derive an upper limit on the intrinsic (random) uncertainty in the GOME ozone values. This method makes use of the information on the model reliability. It is found that the intrinsic (random) uncertainty in GOME total ozone columns is rather small: less than 6 DU (or about 2%). Furthermore, a systematic error is identified which depends on the viewing direction.

#### 1. INTRODUCTION

The Global Ozone Monitoring Experiment (GOME) on board the European satellite ERS-2 measures the spectrum of solar radiation scattered from the Earth's atmosphere between 240 and 790 nm (GOME Interim Science Report, 1993). Apart from ozone, several other trace gas densities can be derived from this spectrum. The technique used by the GOME Data Processor (GDP) to derive these trace gases on an operational basis is Differential Optical Absorption Spectroscopy (DOAS). The DOAS method fits the ratio of the scattered solar radiation (radiance) and the direct solar radiation (irradiance) to reference spectra of the trace gases absorbing in this wavelength region. The *slant* column densities derived in this way are then divided by an effective air mass factor in order to obtain the *vertical* column densities. The air mass factors — which account for the light path of the solar radiation through the atmosphere — are calculated by the GDP with radiative transfer models, developed at the Institutes for Environmental Physics of Heidelberg and Bremen (see other papers in this issue).

In this paper the Assimilation Model KNMI (AMK; Levelt et al., 1996), which is initially developed for imaging of global ozone maps, is used to validate ozone vertical column densities as retrieved by the GDP from GOME observations. The AMK calculates two-dimensional global ozone maps at any given time, using observations of total ozone columns and observations of horizontal wind fields.

Data assimilation as performed by, for instance, the AMK is an essential tool for the validation of satellite data (for several methods of data assimilation see, e.g., Daley, 1991). GOME overpasses are often at large distances from the different ozone measuring ground stations used in the validation campaign. Furthermore, it is not always possible to obtain a ground-based measurement simultaneously with a GOME overpass. Since the ozone column is highly variable in time and space, a lot of ground-based measurements are not suitable for direct comparison. However, data assimilation presents a tool to use these measurements for comparison with GOME, because it takes into account the knowledge about the dynamical behaviour of ozone. Future plans at KNMI, The Netherlands, include combining the AMK with the ground-based measurements gathered by many institutes during the validation period (see other papers in this

issue).

Another way of using the AMK for validation is the comparison of GOME observations with predicted ozone values based on *previous* GOME observations, the main topic of this paper. Differences between the ozone columns directly observed by GOME and the predicted AMK ozone columns gives information on the self-consistency of GOME. An important point to be considered here are the uncertainties in the model itself.

Section 2 describes the AMK and discusses its uncertainties, Section 3 presents the GOME data used for the present study, and Section 4 discusses the results.

#### 2. MODEL DESCRIPTION

The AMK is a two-dimensional (latitude, longitude) global model. It advects the ozone column using the horizontal wind at a single pressure level. The wind fields are obtained from the European Centre for Medium-range Weather Forecast (ECMWF). Observations of total ozone columns are assimilated into the model with the single-correction method. For details on the advection and assimilation methods see Levelt et al. (1996).

The three main assumptions in the model are: (i) The total ozone column variability is dominated by the variability in a relatively thin vertical layer; (ii) Chemical processes have much larger timescales than dynamical processes; (iii) The wind fields transporting the ozone are approximately horizontal.

The first assumption is based on observations of ozone profiles. In normal atmospheric conditions the variability is largest around the tropopause. For ozone-hole conditions the assumption still holds, but here the altitude of the largest variability is much higher. The second assumption is usually valid for the upper troposphere and the lower stratosphere, where the chemical lifetime of ozone varies from weeks to months. However, it is not valid under ozone-hole conditions. The third assumption is based on the knowledge that wind tends to flow along isobaric surfaces, which are in first order approximation horizontal. For a more detailed discussion on the validity of these assumptions we refer to Levelt et al. (1996).

Model uncertainties introduced by making these assumptions can stay relatively small, as long as the AMK is continuously fed with observations. Experiments with TOVS data show that the (root mean square) difference between observations and model output is dominated by the uncertainty in the TOVS data. If the assimilation of new observations is turned off, this difference increases with approximately a factor of two in two days (see Levelt et al., 1996). In general, the reliability of the AMK predicted ozone column at a given time and place decreases as a function of the elapsed time after the last contributing assimilated observation.

The AMK has been optimized for the assimilation and advection of NOAA-TOVS data (Levelt et al., 1996). The assimilation technique makes use of empirically determined coefficients, which are sensitive to the uncertainties in both the model and the observations (in



Table 1: The GOME data used in the present study. Listed are for every day the start and end time of the available observations (columns 2 and 3), and the GDP level 1–2 software version (column 4).

day in 1995	start time	end time	version
25 August	6:03:23	21:50:08	1.20
26 August	5:31:52	21:18:37	1.20
27 August	6:40:57	20:47:07	1.20
28 August	—	—	—
29 August	0:36:13	23:05:10	1.21
30 August	0:04:43	23:59:58	1.21
31 August	0:00:00	23:42:45	1.21
1 September	5:44:07	21:30:38	1.21
2 September	5:12:35	20:59:07	1.21
3 September	6:21:40	20:27:37	1.21
4 September	5:50:10	21:36:42	1.21
5 September	5:18:39	21:05:11	1.21
6 September	6:27:46	20:33:41	1.21
7 September	5:56:14	21:42:47	1.21
8 September	5:24:44	21:11:17	1.21
9 September	6:33:51	20:39:47	1.21

this case TOVS observations). Using GOME data in the model instead of TOVS data, in principle requires other coefficients. These coefficients can be calculated after running the model with at least one month of consecutive observations. Since the present study only uses 15 days of observations (and for most days only 9 out of 14 orbits), we will use as a first order approximation the TOVS coefficients. Tests with TOVS data show that the model output is not very sensitive to small changes in these coefficients (ibid).

The present advection scheme of the AMK uses wind fields at a single pressure level. The specific pressure level used is again empirically determined on TOVS data (ibid), for a time period without an ozone hole. Since this level (200 hPa; comparable to results of Riishojgaard and Lary, 1994) approximately equals the level where the ozone variability is observed to be largest (the tropopause, except under ozone hole conditions), we believe that the best pressure level will not be very different for the GOME data studied here (no ozone hole present). This will be verified when more consecutive GOME data are available. Future versions of the AMK will be using wind fields at different pressure levels, to account for the different altitudes of highest ozone variability, which is clearest in the presence of an ozone hole.

### 3. THE GOME DATA

The GOME data used in the present paper cover the period between 25 August and 9 September 1995. This period is selected because it is the largest (semi-)consecutive period of processed observations in the validation data set. However, this time period still has some gaps: one day (28 August) was not processed and for most of the other days only 9 out of 14 orbits were processed (those received at the Kiruna ground station). Table 1 shows for every day the start and end time of the processed data used in this study.

Note that during the time period studied here ozone values are relatively low and the ozone variability is relatively small when compared to other seasons. Therefore, the conclusions drawn in this paper might only be valid for these relatively quiet periods.

From the data listed in Table 1 we used only the ozone

values with DOAS fit errors less than 5%, with solar zenith angles at the time of observation less than  $74.6^\circ$ , and for which no errors were reported (according to the flags in the ‘Intermediate Results Record’ of the GDP level 2 product). The threshold for the solar zenith angles is chosen, because in the GDP software version 1.20 and 1.21 (used here) the air mass factors for larger solar zenith angles ( $> 74.6^\circ$ ) are still calculated using the first order approximation of single scattering, while for smaller solar zenith angles multiple scattering has been included in the calculations. For large solar zenith angles, ozone values are expected to be 20 – 30% too high. In future releases the air mass factors will all be calculated with the multiple scattering included.

## 4. RESULTS

### 4.1. The experiment

The start field at 25 August 1995 at 0 UT is chosen to be a field with ozone values of 300 DU everywhere.<sup>1</sup> In the present experiment, AMK runs from 25 August, 0 UT, until 10 September 1995, 0 UT, and is fed by the GOME observations listed in Table 1. Figure 1 (left column) shows the resulting ozone fields every third day, at 0 UT.

Due to the time gaps in the GOME data, a large part of the Earth (containing Australia and South-East Asia) is not fed with observations. So the ozone values predicted by the AMK will be uncertain in this region. Furthermore, even if the AMK *would* be continuously fed with observations, it still needs a spin-up period in the order of a few weeks, before the ozone column values are reliable.

Therefore, we define a ‘reliability flag’  $q_i \in [0, 1]$  for each grid cell  $i$ , which depends on the time elapsed after the last observation contributing to the ozone value in this grid cell. The ‘flag field’  $q_i$  is advected in the same way as the ozone field, so that the reliability information on the ozone values keeps attached to it. However, the flag is ‘devaluated’ in time: it is assumed to decline exponentially as  $\exp\{-0.01\Delta t\}$ , where  $\Delta t$  is in hours. This means that, starting with a fully reliable ozone field (i.e.,  $q_i = 1$  for every  $i$ ), after 2 days without any observations the flag would be 0.6 everywhere, and after 3 days it would be 0.5 everywhere. For the start field we take  $q_i = 0$ , for all  $i$ , and every time an ozone observation is assimilated in the ozone field, the value  $q = 1$  is assimilated in the ‘flag field’  $q_i$ , at the same location and with the same assimilation coefficients as for the ozone (see Section 2 and Levelt et al., 1996).

In the right column of Figure 1 the regions with flag  $q_i < 0.5$  (corresponding to about three days without observations) are coloured brown. The spin-up period of the model and the missing data regions are clearly visible.

### 4.2. GOME intrinsic uncertainty

The self consistency of the GOME observations is tested by looking at the root mean square value of the differences between the observations and the predicted model output (based on *previous* GOME observations, and the observed wind field) at the same time and location as the observation. This root mean square value would be equal to the random uncertainty in the GOME observations, in the ideal case of a perfect model and in the case

<sup>1</sup>Another possibility would be to start with a more realistic field, e.g., the assimilated TOVS data on 25 August. However, possible systematic differences might exist between TOVS and GOME, which are unknown yet. We prefer the *known* bias introduced by a constant start field.



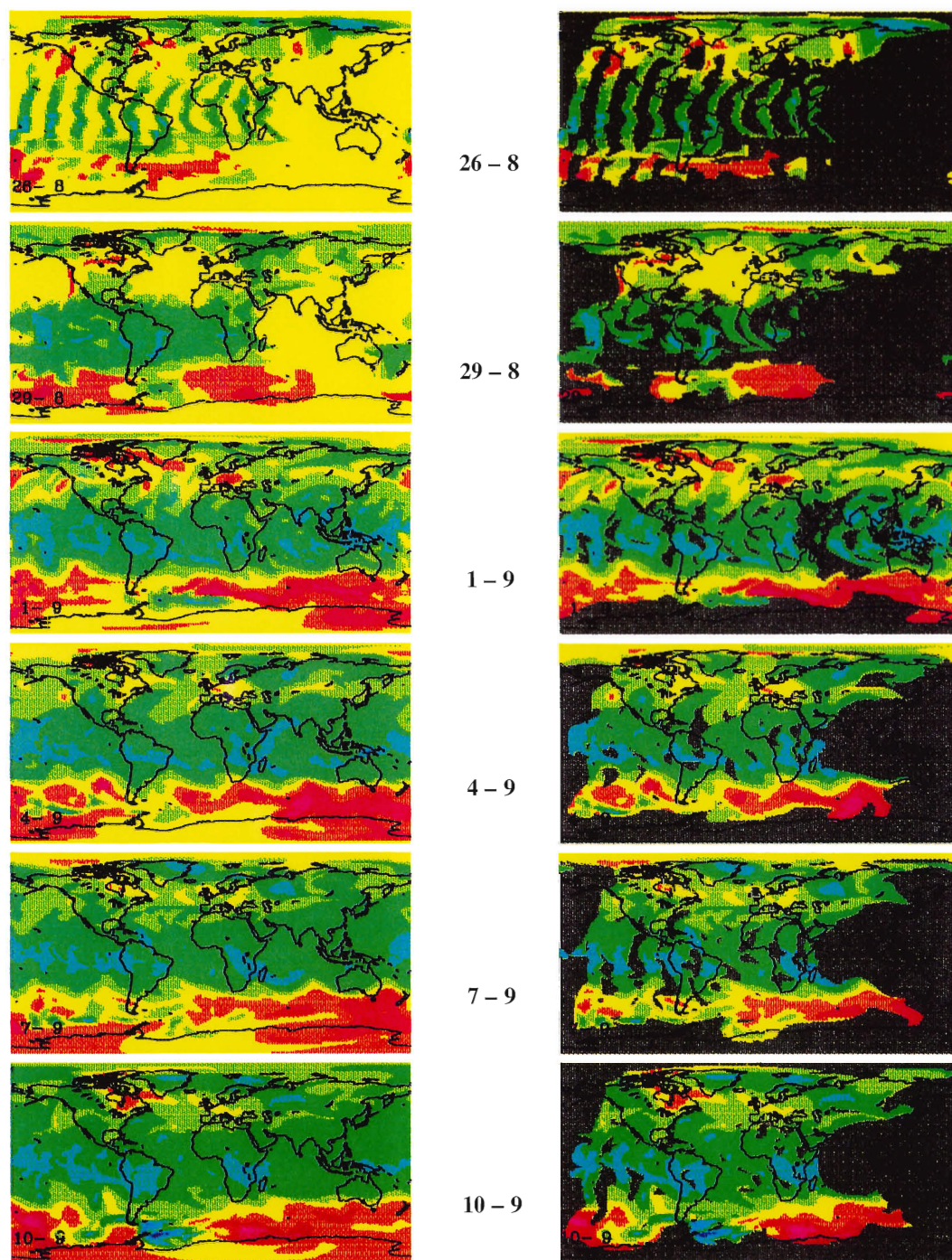


Figure 1: The global ozone fields resulting from the AMK run of 16 consecutive days in August and September (left hand panels). The right hand panels display the same results, but now the 'uncertain' ( $q < 0.5$ , see Section 4.1) regions of the model output are coloured brown. Different ozone values are indicated by different colours, red for high ozone values ( $\sim 350$  DU), light blue for low ozone values ( $\sim 200$  DU). Time goes from top to bottom, the 6 panels are from 26 and 29 August, 1, 4, 7, and 10 September, all at 0 UT, respectively. The stripe-like structures after the first day of the model run, at 26 August 0 UT (upper left panel), show the satellite orbits of 25 August, deformed by the wind field. Inbetween the orbits, no information exists on the ozone values, therefore the start field of 300 DU (yellow) is still visible here. The relatively large 'uncertain' (brown-coloured) regions in the right hand panels (Indian Ocean and Australia) result from the data gaps near the date line. The South Pole is not observed (hence ozone values there are indicated 'uncertain'), because the Sun is not illuminating this part of the Earth in the time period studied here.





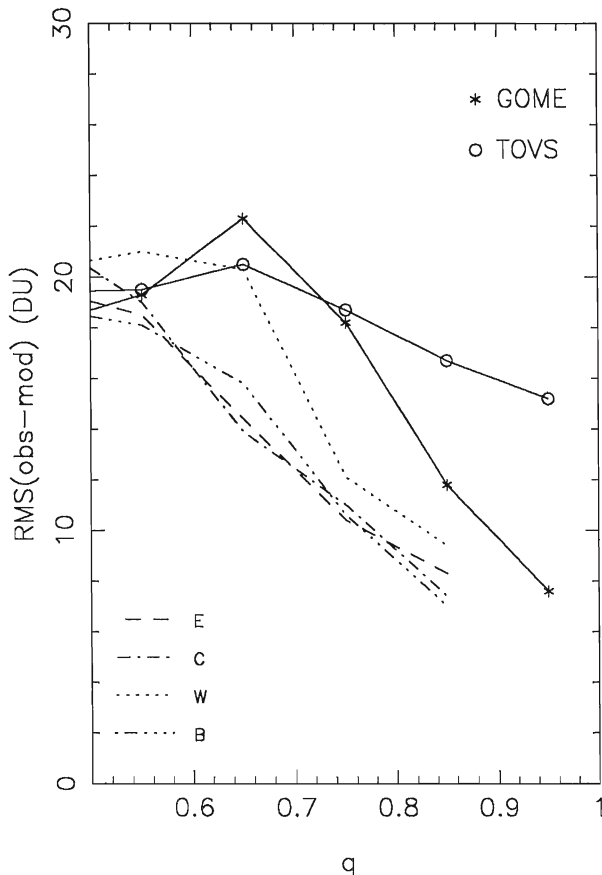


Figure 2: The root mean square of the difference between the observations and the model-output for the last three days of the AMK run, as a function of the reliability flag  $q$ . The data is binned in bins of  $\Delta q = 0.1$ . The stars indicate the results for the AMK run with GOME data, the circles indicate the results for the AMK run with TOVS data (see Section 4.2). The four dashed and dotted lines indicate the results for the AMK runs ‘East’, ‘Centre’, ‘West’ and ‘Backscan’ (see Section 4.3). The number of points contributing to the root mean square is more than 1600 per  $q$ -bin for the solid lines, and more than 160 per  $q$ -bin for the dashed and dotted lines.

that the GOME observations would have no systematic dependencies on for instance the solar zenith angle or the surface albedo or the viewing direction. In more realistic cases the root mean square value gives an *upper limit* to the intrinsic (random) uncertainty in the GOME ozone values. By plotting the root mean square value of the differences between observations and model output as a function of the reliability flag  $q$  (Figure 2, solid line with stars), the influence of model uncertainties (caused both by the relatively large periods without observations and by the simplifying assumptions underlying the model, see Section 2) can largely be ruled out. The model is perfect if  $q = 1$ , so the asymptotic value of the root mean square for  $q \rightarrow 1$ , gives the tightest constraint on the intrinsic uncertainty in the GOME total ozone value. From Figure 2 we conclude that this intrinsic uncertainty is less than 7 DU, which is very accurate ( $\sim 2\%$ ): the zenith sky observations of ground-based Brewer instrument, for instance, have a larger uncertainty (5%, see Piters et al., 1996).

For comparison a similar experiment is done with an AMK run using only TOVS total ozone data. We used 15

consecutive days in April 1992<sup>2</sup>, starting with the same start field as in the GOME experiment. The root mean square of the differences between the TOVS observations and the model output for the last three days of the run is plotted in Figure 2 (solid line with circles). The asymptotic value of the TOVS root mean square value for  $q \rightarrow 1$  is about 15 DU, corresponding to the intrinsic uncertainty usually attributed to the TOVS data (Planet et al., 1984).

Note that when the systematic dependencies of GOME total ozone value on for instance solar zenith angle (as observed by the GOME validation team, see other papers in this issue) will become less in future processing of the GOME data, the upper limit to the intrinsic uncertainty will become even smaller than 7 DU. In the next subsection we identify another systematic dependence of the GOME total ozone column, and find a tighter constraint on the intrinsic uncertainty.

### 4.3. Dependence on viewing direction

Here, we study the possible dependence of the GOME total ozone column on the viewing direction or line-of-sight zenith angle. In normal operational mode, the GOME scan mirror moves every 6 seconds in 4.5 seconds from left to right over approximately  $60^\circ$  and in 1.5 seconds back again. During the validation period the instrument integrated 0.375 seconds at the end of every 1.5 seconds, resulting in four ground pixels per scan, the so-called ‘East’, ‘Centre’, ‘West’, and ‘Backscan’ pixel. The scan mirror velocity together with the integration time determine the size of the ground pixels: the ‘East’, ‘Center’ and ‘West’ ground pixels are approximately  $80 \times 40 \text{ km}^2$ , the ‘Backscan’ pixel is approximately  $240 \times 40 \text{ km}^2$ . The corresponding average line-of-sight zenith angles for these ground pixels are  $-13^\circ$ ,  $+7^\circ$ ,  $+27^\circ$ , and  $-23^\circ$ .

The experiment described in Section 4.1 is repeated here four times, each time assimilating only the observations with the same viewing direction. The four different AMK runs are called ‘East’, ‘Center’, ‘West’, and ‘Backscan’, to their corresponding GOME ground pixel types. Figure 2 also shows the root mean square value of the differences between the observations and the model output for the four different AMK runs as a function of the reliability flag  $q$ . The root mean square value is in all these cases smaller than that for the AMK run using all observations as described in Section 4.2. This suggests that the intrinsic uncertainty in the GOME total ozone values is even smaller than 6 DU, and that there is a systematic error on the GOME total ozone value depending on viewing direction.

The magnitude of this systematic error is found by comparing the four different model outputs at the end of the AMK runs, on 10 September, 0 UT. If there would be no systematic errors with respect to the viewing direction, these four model outputs are expected to look the same, at least for the regions where the model uncertainties are small (i.e.,  $q$  large). We have calculated the difference between two model outputs for each grid cell, and averaged over the grid cells for which  $q > 0.6$  for both AMK runs. In Figure 3 these mean differences of each AMK run with AMK run ‘Centre’ are plotted. The error bars indicate the uncertainty in the mean. From this figure, it appears that significant systematic differences exist between ozone values corresponding to different pixel types.

<sup>2</sup>Note that the variability of the ozone field in April is larger than in September. This might influence the results presented here. However, the root mean square differences for the TOVS experiment are expected never to be smaller than the intrinsic TOVS uncertainty, i.e., approximately 15 DU.

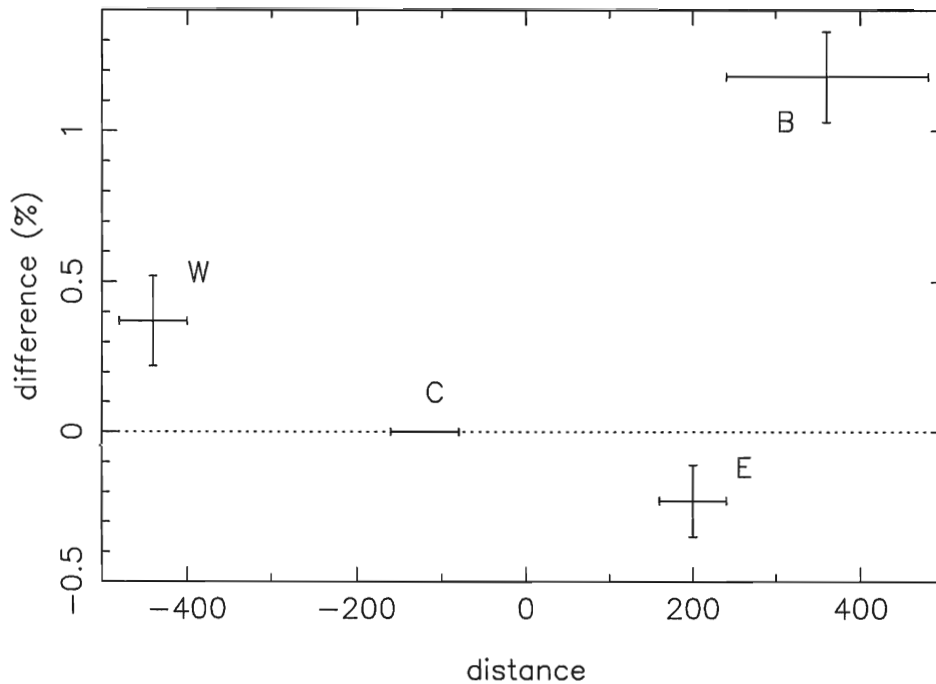


Figure 3: The average deviation of the model output of AMK runs ‘West’, ‘Center’, ‘East’ and ‘Backscan’ with respect to the output of AMK run ‘Center’ (see Section 4.3). The average has been taken over the set of grid cells with flag  $q > 0.6$ . The error bars denote the uncertainty in the mean. The horizontal axis indicates the position and extend of the different ground pixel types used in the different AMK runs, expressed in the distance (in km) from the projected nadir viewing direction. Negative distances refer to West.

The magnitude of the differences found here between the ozone values from the ‘West’, ‘Centre’ and ‘East’ pixels appears to be consistent with the dependence of the air mass factor on the differential azimuth angle<sup>3</sup>, which is *not* taken into account in the GOME retrieval algorithms (Thomas, 1996).

The large systematic offset of the ‘Backscan’-pixel values can not be explained by the air mass factor dependence on the azimuth angle (in this case, the offset would be expected to be somewhat lower than the ‘East’ pixel offset in Figure 3). The explanation might have something to do with the size of the ‘Backscan’ ground pixel. This pixel is three times as large as the other three ground pixels, due to the higher scanning velocity of the scan mirror while moving from right to left. The air mass factor, ozone vertical column, polarization and cloud cover can vary considerably along the pixel. Although in the present GDP software some first order corrections are made for (known) variations, there might still be some bias due to the inevitable averaging over the extended ‘Backscan’ pixel.

## 5. CONCLUSIONS

In the previous sections, the Assimilation Model KNMI proved to be of value in the validation of GOME total ozone values. Although the data set available for this study is very limited (15 consecutive days with large data gaps), we are able to derive the following conclusions.

For the period considered here (25 August – 9 September 1995) and for the GOME data processing software versions 1.20 and 1.21, the intrinsic (random) uncertainty

<sup>3</sup>Azimuth angles are defined in a plane parallel to the Earth’s surface at the point observed by the instrument. The differential azimuth angle is defined as the difference between the azimuth angles of the radiation reflected towards the instrument and the incident radiation.

of GOME total ozone columns is less than 6 DU, or approximately 2%, (Sections 4.2. and 4.3).

For this same period and software versions there appears to be a systematic error in the total ozone column depending on the viewing direction or pixel type (Section 4.3). The magnitude of this systematic error with respect to the ‘Centre’-pixel observations is  $0.37 \pm 0.15\%$  for the ‘West’-pixel observations,  $-0.23 \pm 0.12\%$  for the ‘East’-pixel observations, and  $1.18 \pm 0.17\%$  for the ‘Backscan’-pixel observations. The magnitude of the differences found here between the ozone values from the ‘West’, ‘Centre’ and ‘East’ pixels appears to be consistent with the expected difference due to the dependencies of the air mass factor on the differential azimuth angle. But the systematic difference between the ozone values from the ‘Backscan’ pixels and those from the other pixels is too large to be explained by these air mass factor dependencies.

## Acknowledgements

We gratefully acknowledge the members of the GOME Validation Group for fruitful discussions on the topics discussed in this paper. Especially, we would like to thank John Burrows (IUP, Bremen) and Piet Stammes (KNMI) for their helpful comments. We are grateful to Wolfgang Balzer and the data processing team at DLR for helping us to understand the GDP product. Ankie Piters is funded by SRON, The Netherlands, Pieter Levelt is funded by BCRS, The Netherlands.

## References

Daley R., Atmospheric Data Analysis, Cambridge University Press, Canada, 1991

Global Ozone Monitoring Experiment, Interim Science Report, European Space Agency (ESA), SP-1151, 1993

Levelt P.F., Allaart M.A.F., Kelder H.M., On the Assimilation of Total ozone satellite Data, *accepted for publication*, Annales Geophysicae, 1996

Piters A.J.M., Levelt P.F., Kuik F., Allaart M.A.F., Kelder H.M., Ground-based measurements at KNMI used for GOME validation, this issue, 1996 \*

Planet W.G., Crosby D.S., Lienisch J.H., Hill M.L., Determination of total ozone amount from TIROS Radiance Measurements, J. Clim. Appl. Meteorol. 23, 308, 1984

Proceedings of the GOME validation workshop, Frascati, 24–26 January, 1996 (this issue) \*

Riishojgaard L.P., Lary D.J., Short range simulations of extratropical total ozone with ASPERGE-/IFS, Proceedings of ECMWF Workshop on the stratosphere and numerical weather prediction, ECMWF, 1994

Thomas W., DLR, private communication, 1996

---

\* Proceedings of the GOME Geophysical Validation Campaign, ESA WPP-108, ESA/ESTEC, Noordwijk (1996)



## List of acronyms

ADEOS	Advanced Earth Observing Satellite (NASDA)
AMF	Air Mass Factor
AMK	Advection Model KNMI
DAK	Doubling-Adding KNMI
DOAS	Differential Optical Absorption Spectroscopy
DLR	Deutsche Forschungsanstalt für Luft- und Raumfahrt
ENVISAT	Environmental Satellite (ESA)
EUMETSAT	European Meteorological Satellite Agency
ERS	Satellite (ESA)
ESA	European Space Agency
GDP	GOME Data Processor
GOME	Global Ozone Monitoring Experiment
ICFA	Initial Cloud Fitting Algorithm
IMGA	Institute for Methodological Studies of Geophysics and Environment
IUP	Institute for Environmental Physics
KNMI	Royal Netherlands Meteorological Institute
METOP	Meteorological Operational Polar Satellite (EUMETSAT)
NASDA	National Space Development Agency of Japan
OMI	Ozone Monitoring Instrument
PI	Principal Investigator
PMD	Polarisation Measuring Device
RIVM	National Institute of Public Health and Environmental Protection (NL)
SCD	Slant Column Density
SCIAMACHY	Scanning Imaging Absorption Spectrometer for Atmospheric Cartography
SRON	Space Research Organisation of the Netherlands
TMK	Transport Model KNMI
TNO/TPD	TNO Institute of Applied Physics
TOMS	Total Ozone Mapping Spectrometer
VCD	Vertical Column Density



# KNMI-Publicaties, Technische & Wetenschappelijke Rapporten gepubliceerd sedert 1988

Een overzicht van alle publicaties van het Koninklijk Nederlands Meteorologisch Instituut die tussen 1849 en 1988 werden uitgegeven, wordt u op verzoek toegezonden door de Bibliotheek van het KNMI, postbus 201, 3730 AE De Bilt, tel. 030 - 2 206 855, fax. 030 - 2 210 407.

## KNMI-publicatie met nummer

150-27	Normalen en extreme waarden van 15 hoofdstations voor het tijdvak 1961-90 / samenst. H.J. Krijnen ...[et al.]	1992
165-5	Historische weerkundige waarnemingen: beschrijving antieke meetreeksen / H.A.M. Geurts en A.F.V. van Engelen	1992
172	Vliegen in weer en wind: geschiedenis van de luchtvaartmeteorologie / Tj. Langerveld	1988
173	Werkdocument verspreidingsmodellen / red. H. van Dop ; in samenwerking met het RIVM	1988
174	Ons klimaat, onze planeet / voorw. H. Tennekes ; inleiding C.J.E. Schuurmans ; met bijdr. van H. van Dop ...[et al.]	1989
175	Klimaat-onderzoek Westland ten behoeve van kustuitbreiding / W.H. Slob	1989
176	Stormenkalender: chronologisch overzicht van alle stormen langs de Nederlandse kust 1964-1990 / B. Augustijn, H. Daan ...[et al.]	1990
177	Description of the RIVM-KNMI PUFF dispersion model / G.H.L. Verver ...[et al.]	1990
178	Modules A & B / Bureau Vorming en Opleiding <b>[uitsluitend intern beschikbaar]</b>	1991-
179	Catalogus van aardbevingen in Nederland / G. Houtgast	1991
179a	Catalogus van aardbevingen in Nederland : 2e, gewijzigde druk / G. Houtgast	1992
180	List of acronyms in environmental sciences / [P. Geerders]	1991
180a	List of acronyms in environmental sciences : revised edition / [P. Geerders and M. Waterborg]	1995
181	Nationaal gebruik van de groepen 7wwW1W2 en 960ww voor landstations / [samenst. H. van Drongelen ea.]	1992
181a	FM12 Synop : internationale en nationale regelgeving voor het coderen van de groepen 7wwW1W2 en 960ww	1995
181b	FM12 Synop : internationale en nationale regelgeving voor het coderen van de groepen 7wwW1W2 en 960ww ; derde herziene versie	1996
182	Wijziging aeronautische codes : 1 juli 1993 / [P.Y. de Vries en A.A. Brouwer]	1993
183-1	Rainfall in New Guinea (Irian Jaya) / T.B. Ridder	1995
183-2	Vergelijking van zware regens te Hollandia (Nieuw-Guinea), thans Jayapura (Irian Jaya) met zware regens te De Bilt / T.B. Ridder	1995
183-3	Verdamping in Nieuw-Guinea, vergelijking van gemeten hoeveelheden met berekende hoeveelheden / T.B. Ridder	1995
183-4	Beschrijving van het klimaat te Merauke, Nieuw-Guinea (Irian Jaya) in verband met de eventuele vestiging van een zoutwinningsbedrijf aldaar / T.B. Ridder en H.W.H. Weeda	1995
183-5	Overzicht van klimatologische en geofysische publikaties betreffende Nieuw-Guinea / T.B. Ridder	1995
184	Inleiding tot de algemene meteorologie : studie-uitgave / B. Zwart, A. Steenhuisen, m.m.v. H.J. Krijnen	1994
184a	Inleiding tot de algemene meteorologie : studie uitgave ; 2e, geheel herziene druk / B. Zwart, A. Steenhuisen, m.m.v. H.J. Krijnen ea.	1995
185	Handleiding voor het gebruik van sectie 2 van de FM 13-X SHIP code door stations op zee / KNMI; Kon. Luchtmacht; Kon. Marine	1994
185a	Handleiding voor het gebruik van sectie 2 van de FM 13-X SHIP-code voor waarnemers op zee / KNMI; Kon.Luchtmacht, Kon.Marine	1995

## Overigen

Zonnestraling in Nederland / C.A. Velds (in samenwerking met uitgeverij Thieme in de serie "Het klimaat van Nederland"; 3) 1992

## Technisch rapport = technical report (TR) - ISSN 0169-1708

103a	Wind-chill [geheel herziene versie] / B. Zwart	1992
105	Description of the Cabauw turbulence dataset 1977-1979 / C. Hofman	1988
106	Automatische detectie van inversies met sodar / A.C.M. Beljaars en R. Agterberg	1988
107	Numerieke atmosfeermodellen / A.P.M. Baede	1988
108	Inpassing van Meteosat informatie in de meteorologische besluitvorming / J. Roodenburg	1988
109	Opmeting van het aardmagneetveld in Nederland, herleid naar 1985 / J.H. Rietman	1988
111	Van Penman naar Makkink: een nieuwe berekeningswijze voor de klimatologische verdampingsgetallen / red. J.C. Hooghart ...[et al.]	1988
112	Description of a software library for the calculation of surface fluxes / A.C.M. Beljaars ...[et al.]	1989
113	Menghoogteberekeningen voor het Europees continent: een vergelijkend onderzoek / M.P. Scheele en H. van Dop	1989
114	Operational WAMS statistics over the period December 1986 - March 1987 / R.A. van Moerkerken ...[et al.]	1989
115	Mesoscale terrain roughness mapping of the Netherlands / R. Agterberg and J. Wieringa	1989
116	Geschiedenis van de landbouwmeteorologie in Nederland tot 1972 / J.P.M. Woudenberg	1989
117	Instabiliteiten rond de straalstroom / R.P. Henzen	1989
118	Verificatie van de GONO golfverwachting over de periode oktober 1987 - april 1988 / R.A. van Moerkerken	1989
119	Spectra en gradienten van hoge windsnelheden te Cabauw tot 200 meter / R.W.M. Meijer	1989
120	About the possibilities of using an air transformation model in Tayun, Shanxi province, China / J. Reiff ...[et al.]	1989
121	The effect of wave data assimilation of the numerical simulation of wave energy advection / M. de las Heras ...[et al.]	1990
122	Objective analysis of precipitation observations during the Chernobyl episode / M.P. Scheele and G.H. Verver	1990
123	The use of satellite data in the ECMWF analysis system / K. Lablancz	1990
124	A primitive equation model for the Equatorial Pacific / M.A.F. Allart and A. Kattenberg	1990
125	Technical description of the high-resolution air mass transformation model at KNMI / E.I.F. de Bruin ...[et al.]	1990
126	Verificatie kwantitatieve neerslagverwachting korte termijn (proefperiode) voor 5 regio's / D. Messerschmidt	1990
127	Quantitative processing of Meteosat-data: implementation at KNMI: applications / S.H. Muller	1990
128	A primary experiment of statistical interpolation schemes used in sea wave data assimilation / Gao Quanduo	1990
129	Coordinate conversions for presenting and compositing weather radar data / H.R.A. Wessels	1990
130	Flux-profile relationships in the nocturnal boundary layer / P. Bouwman	1990
131	The implementation of the WAQUA/CSM-16 model for real time storm surge forecasting / J.W. de Vries	1991
132	De luchttemperatuur boven West-Ameland / F. Ynsen	1991
133	Seizoenverloop en trend in de chemische samenstelling van de neerslag te Lelystad / T.A. Buishand en J.H. Baard	1991
134	Technical description of LAM and OI: Limited Area Model and Optimum Interpolation analysis / W.C. de Rooy ...[et al.]	1991
134a	Technical description of LAM and OI: Limited Area Model and Optimum Interpolation analysis, 2nd edition / W.C. de Rooy ...[et al.]	1992
135	Relatieve trajectorijen in en rond een depressie / J.P.A.J. van Beeck	1991
136	Bepaling van een directe en diffuse straling en van zonneshijnduur uit 10-minuutwaarden van de globale straling / W.H. Slob ...[et al.]	1991



137	LAM en NEDWAM statistics over the period October 1990 - April 1991 / R.A. van Moerkerken	1991
138	Dagsom van de globale straling : een rekenmethode en verwachtingsverificatie / M.C. Nolet	1991
139	A real-time wave data quality control algorithm / Maria Paula Etala	1991
140	Syllabus Fysische Meteorologie I / H.R.A. Wessels	1991
141	Systeembeschrijving Mist Voorspel Systeem MIVOS / D. Blaauboer, H.R.A. Wessels en S. Kruizinga	1992
142	Het nachtelijk windmaximum : een interactieve verwachtingsmethode / N. Maat en H. Bakker	1992
143	Neerslagverificatie LAM / W.C. de Rooy en C. Engeldal	1992
144	Aanpassing vocht-bedeckingsgraadrelaties in het LAM / W.C. de Rooy	1992
145	Een verificatie van de Eurogids, de gidsverwachting voor vervoer en toerisme / H.G. Theihzen	1992
146	The earth radiation budget experiment : overview of data-processing and error sources / Arnout J. Feijt	1992
147	On the construction of a regional atmospheric climate model / Jens H. Christensen and Erik van Meijgaard	1992
148	Analyse van torenwindgegevens over het tijdvak 1977 tot en met 1991 / Gertie Geertsema	1992
149	The performance of drag relations in the WAQUA storm surge model / J.R.N. Onvlee	1993
150	Verifications of 3I retrievals vis-à-vis radiosonde observations / G.J. Prangma	1993
151	Het Synoptisch Symposium : een verslag / red. H.G. Theihzen	1993
152	The ACIFORN hydrological programme : the water cycle of a Douglas fir forest / F.C. Bosveld ...[et al.]	1993
153	Het APL+-programma / R.M. van Westrheden	1993
154	The effect of spatial averaging on threshold exceedances of daily precipitation amounts / T.A. Buishand,	1993
155	Neerslagvergelijking van Espelo ten opzichte van het omgevingsgemiddelde / J.P.M. van Dun en J. Verloof	1993
156	On the effects of limited spectral resolution in third-generation wave models / I.V. Lavrenov and J.R.A. Onvlee	1993
157	Meteorologische evaluatie van de zichtmetingen langs de A16 / H.R.A. Wessels	1993
158	Het programma voor berekening van zonnenschijnduur uit globale straling / U. Bergman	1993
159	Verificatie weersverwachtingen 1955 - 1993 / H. Daan	1993
160	Drie objectieve indices voor clear-air turbulence nader bekeken / H. Bakker	1993
161	The ASGASEX experiment / W.A. Oost	1994
162	TEBEX observations of clouds and radiation -potential and limitations / P. Stammes ...[et al.]	1994
163	Evaluatie kwaliteitsonderzoek mistdata "Mistprojekt A-16" Breda / M. van Berchum	1994
164	Standaard stralingsmetingen met een zonnevolger / A.C.A.P. van Lammeren en A. Hulshof	1994
165	Neurale netwerken versus lineaire regressie / R.M. Meuleman	1994
166	Seismische analyse van de aardbeving bij Alkmaar op 6 augustus 1994 / [SO]	1994
167	Seismische analyse van de aardbeving bij Alkmaar op 21 september 1994 / [SO]	1994
168	Analyse van het seismische risico in Noord-Nederland / Th. de Crook, B. Dost en H.W. Haak	1995
169	Evaluatie van neerslagprognoses van numerieke modellen voor de Belgische Ardennen in december 1993 / Erik van Meijgaard	1994
170	DARR-94 / C.P.G. Lomme	1994
171	EFEDA-91 : documentation of measurements obtained by KNMI / W.A.A. Monna ...[et al.]	1994
172	Cloud lidar research at the Royal Netherlands Meteorological Institute and KNMI2B2 version 2 cloud lidar analysis software documentation / Alexandre Y. Fong and André C.A.P. van Lammeren	1994
173	Measurements of the structure parameter of vertical wind-velocity in the atmospheric boundary layer / R. van der Ploeg	1995
174	Report of the ASGASEX'94 workshop / ed. by W.A. Oost	1995
175	Over slecht zicht, bewolking, windstoten en gladheid / J. Terpstra	1995
176	Verification of the WAQUA/CSM-16 model for the winters 1992-93 and 1993-94 / J.W. de Vries	1995
177	Nauwkeurig nettostraling meten / M.K. van der Molen en W. Kohsiek	1995
178	Neerslag in het stroomgebied van de Maas in januari 1995: waarnemingen en verificatie van modelprognoses / Rudmer Jilderda ...[et al.]	1995
179	First field experience with 600PA phased array sodar / Henk Klein Baltink	1995
180	Een Kalman-correctieschema voor de wegdektemperatuurverwachtingen van het VAISALA-model / A. Jacobs	1995
181	Calibration study of the K-Gill propeller vane / Marcel Bottema	1995
182	Ontwikkeling van een spectraal UV-meetinstrument / Frank Helderman	1995
183	Rainfall generator for the Rhine catchment : a feasibility study / T. Adri Buishand and Theo Brandsma	1996
184	Parametrisatie van mooi-weer cumulus / M.C. van Zanten	1995
185	Interim report on the KNMI contributions to the second phase of the AERO-project / Wiel Wauben, Paul Fortuin ...[et al.]	1995
186	Seismische analyse van de aardbevingen bij Middelstum (30 juli 1994) en Annen (16 augustus 1994 en 31 januari 1995) / [SO]	1995
187	Analyse wenselijkheid overname RIVM-windmeetlokaties door KNMI / H. Benschop	1996
188	Windsnelheidsmetingen op zeestations en kuststations: herleiding waarden windsnelheden naar 10-meter niveau / H. Benschop	1996
189	On the KNMI calibration of net radiometers / W. Kohsiek	1996
190	NEDWAM statistics over the period October 1994 - April 1995 / F.B. Koek	1996
191	Description and verification of the HIRLAM trajectory model / E.I.F. de Bruijn	1996
192	Tiltmeting : een alternatief voor waterpassing ? / H.W. Haak	1996
193	Error modelling of scatterometer, in-situ and ECMWF model winds; a calibration refinement / Ad Stoffelen	1996

### **Wetenschappelijk rapport = scientific report (WR) - ISSN 0169-1651**

88-01	Central Sudan surface wind data and climate characteristics / E.H. Abu Bakr	
88-02	Startocumulus modeling / P.G. Duynkerke	
88-03	Naar een niet-lineair wateropzetmodel : stand van zaken februari 1988 / C.J. Kok	
88-04	The boundary layer wind regime of a representative tropical African region, central Sudan / E.H. Abu Bakr	
88-05	Radiative cooling in the nocturnal boundary layer / S.A. Tjemkes	
88-06	Surface flux parameterization schemes : developments and experiences at KNMI / A.A.M. Holtslag and A.C.M. Beljaars	
89-01	Instability mechanisms in a barotropic atmosphere / R.J. Haarsma	
89-02	Climatological data for the North Sea based on observations by voluntary observing ships over the period 1961-1980 / C.G. Korevaar	
89-03	Verificatie van GONO golfverwachtingen en van Engelse fine-mesh winden over de periode oktober 1986 - april 1987 / R.A. van Moerkerken	
89-04	Diagnostics derivation of boundary layer parameters from the outputs of atmospheric models / A.A.M. Holtslag ...[et al.]	
89-05	Statistical forecasts of sunshine duration / Li Zhihong and S. Kruizinga	
90-01	The effect of a doubling atmospheric CO2 on the stormtracks in the climate of a GCM / P.C. Siegmund	
90-02	Analysis of regional differences of forecasts with the multi-layer AMT-model in the Netherlands / E.I.F. de Bruijn, Li Tao Guang ...[et al.]	
90-03	Description of the CRAU- data-set: Meteosat data, radiosonde data, sea surface temperatures : comparison of Meteosat and Heimann-data / S.H. Muller, H. The, W. Kohsiek and W.A.A. Monna	
90-04	A guide to the NEDWAM wave model / G. Burgers	
91-01	A parametrization of the convective atmospheric boundary layer and its application into a global climate model / A.A.M. Holtslag ...[et al.]	

91-02 Turbulent exchange coefficients over a Douglas fir forest / F.C. Bosveld  
92-01 Experimental evaluation of an arrival time difference lightning positioning system / H.R.A. Wessels  
92-02 GCM control run of UK Met.Office compared with the real climate in the Northwest European winter / J.J. Beersma  
92-03 The parameterization of vertical turbulent mixing processes in a General Circulation Model of the Tropical Pacific / G. Janssen  
92-04 A scintillation experiment over a forest / W. Kohsiek  
92-05 Grondtemperaturen / P.C.T. van der Hoeven en W.N. Lablans  
92-06 Automatic suppression of anomalous propagation clutter for noncoherent weather radars / H.R.A. Wessels ...[et al.]  
93-01 Searching for stationary stable solutions of Euler's equation / R. Salden  
93-02 Modelling daily precipitation as a function of temperature for climatic change impact studies / A.M.G. Klein Tank and T.A. Buishand  
93-03 An analytical conceptual model of extratropical cyclones / L.C. Heijboer  
93-04 A synoptic climatology of convective weather in the Netherlands / Dong Hongnian  
93-05 Conceptual models of severe convective weather in the Netherlands / Dong Hongnian  
94-01 Seismische analyse van aardbevingen in Noord-Nederland : bijdrage aan het multidisciplinaire onderzoek naar de relatie tussen gaswinning en aardbevingen / H.W. Haak en Th. de Crook  
94-02 Storm activity over the North Sea and the Netherlands in two climate models compared with observations / J.J. Beersma  
94-03 Atmospheric effects of high-flying subsonic aircraft / W. Fransen  
94-04 Cloud-radiation-hydrological interactions : measuring and modeling / A. Feijt ...[et al.]  
94-05 Spectral ultraviolet radiation measurements and correlation with atmospheric parameters / F. Kuik and H. Kelder  
95-01 Transformation of precipitation time series for climate change impact studies / A.M.G. Klein Tank and T.A. Buishand  
95-02 Internal variability of the ocean generated by a stochastic forcing / M.H.B. van Noordenburg  
95-03 Applicability of weakly nonlinear theory for the planetary-scale flow / E.A. Kartashova  
95-04 Changes in tropospheric NOx and O3 due to subsonic aircraft emissions / W.M.F. Wauben ...[et al.]  
95-05 Numerical studies on the Lorenz-84 atmosphere model / Leonardo Anastassiades  
95-06 Regionalisation of meteorological parameters / W.C. de Rooy  
95-07 Validation of the surface parametrization of HIRLAM using surface-based measurements and remote sensing data / A.F. Moene, H.A.R. de Bruin ...[et al.]  
95-08 Probabilities of climatic change : a pilot study / Wiegner Fransen (ed.) and Alice Reuvekamp  
96-01 A new algorithm for total ozone retrieval from direct sun measurements with a filter instrument / W.M.F. Wauben  
96-02 Chaos and coupling: a coupled atmosphere ocean-boxmodel for coupled behaviour studies / G. Zondervan  
96-03 An acoustical array for subsonic signals / H.W. Haak  
96-04 Transformation of wind in the coastal zone / V.N. Kudryavtsev and V.K. Makin  
96-05 Simulations of the response of the ocean waves in the North Atlantic and North Sea to CO2 doubling in the atmosphere / Kathy M. Rider ...[et al.]  
96-06 Microbarograph systems for the infrasonic detection of nuclear explosions / H.W. Haak and G.J. de Wilde  
96-07 An ozone climatology based on ozonesonde measurements / J.P.F. Fortuin





